Aus dem Institut
Leibniz-Forschungsinstitut für Molekulare Pharmakologie

DISSERTATION

Gating modules of the AMPA receptor pore domain revealed by unnatural amino acid mutagenesis

zur Erlangung des akademischen Grades
Doctor of Philosophy (PhD)

vorgelegt der Medizinischen Fakultät
Charité – Universitätsmedizin Berlin

von

Anahita Poshtiban, B.Sc., M.Sc.

aus Berlin, Deutschland

Datum der Promotion: 18.09.2020

Contents

List of Figures

List of Abbreviations

Å	Ångstrom
aaRS	aminoacyl-tRNA synthetase
AMPA	α-amino-3-hydroxy-5-methyl-4-isoxazole propionic acid
ATD	amino-terminal domain
AzF	p-azido-L-phenylalanine
BzF	p-benzoyl-L-phenylalanine
CTD	carboxy-terminal domain
CTZ	cyclothiazide
HEK	human embryonic kidney
iGluR	ionotropic glutamate receptor
LBD	ligand-binding domain
mRNA	messenger ribonucleic acid
NMDA	N-methyl-D-aspartate
PDB ID	protein data bank identifier
RNA	ribonucleic acid
TARP	transmembrane AMPA receptor regulatory proteins
TEV	tobacco etch virus
TMD	transmembrane domain
tRNA	transfer RNA
TyrRS	tyrosyl-tRNA synthetase
UAA	unnatural amino acid
UV	ultraviolet
WT	wild-type

I Abstract

Deutsch

Ionotrope Glutamatrezeptoren (iGluR) sind ligandengesteuerte Ionenkanäle, die eine wichtige Rolle für eine gesunde Hirnfunktion spielen. Dabei gehört der α-amino-3-hydroxyl-5-methyl-4-isoxazol-propionic acid (AMPA)-Subtyp der Glutamatrezeptoren zu den Hauptvermittlern der schnellen exzitatorischen synaptischen Transmission im Zentralnervensystem. Deren Funktionsstörung ist mit zahlreichen neurologischen Erkrankungen assoziiert. Folglich widmen sich viele Forscher der Untersuchung von Struktur und Funktion von iGluRs. Trotz des neuesten Fortschritts bei der Auflösung ihrer strukturellen Architektur und Dynamik, konnten bisher nur wenige Methoden die Dynamiken in der Membrandomäne aufklären.

Hier präsentiere ich ein optogenetisches Verfahren, welches die Aufklärung der Dynamiken der AMPA Rezeptor Transmembrandomäne (TMD) zum Ziel hat. Für diese Methode wurde der positions-spezifische Einbau von photo-aktiven unnatürlichen Aminosäuren (UAAs) eingesetzt. Auf diese Weise erzeugten wir photo-kontrollierbare AMPA Rezeptoren, die mit hoher räumlicher und zeitlicher Präzision gesteuert werden können, indem Licht als orthogonales Inputsignal genutzt wurde. Wir bauten die UAAs p-benzoyl-L-phenylalanine (BzF) and p-azido-L-phenylalanine (AzF) an 30 individuellen Positionen quer durch die TMD von der AMPA Rezeptoruntereinheit GluA2 ein.

Elektrophysiologische Messungen an *outside-out patches* von Säugetierzellen (HEK 293 Zellen) in Kombination mit synchronisiertem UV-Licht mittels Epi-Beleuchtung führte zu einer Reihe von optischen Effekten auf die Kanalaktivität.

Bei 11 verschiedenen Mutanten mit entweder eingebautem AzF oder BzF in die GluA2 TMD, identifizierten wir lichtinduzierte Veränderungen der Rezeptoraktivität, von einer schnellen Inhibition bis hin zu einer Aktivierung. Einer der eindrucksvollsten UV-Effekte kam bei der F579-Position mit eingebautem AzF inmitten der M2 Helix der TMD hervor, die komplexe Veränderungen in der Rezeptorkinetik zeigte nachdem AzF durch UV-Licht aktiviert wurde und sich vernetzte. Der Eintritt in die Desensibilisierung wurde verlangsamt, jedoch, einmal eingetreten, wurde der desensibilisierte Zustand auch stabiler und schien leitfähig zu sein. Die Ergebnisse deuten auf eine zentrale Rolle des M2-Segments beim *Gating* hin, die über seine gegenwärtig akzeptierte Funktion in der Ionenselektivität hinausgeht. Darüber hinaus lieferten unsere elektrophysiologischen Ergebnisse, ergänzt durch biochemische Experimente, Hinweise für eine Interaktion zwischen der Pre-M1 und M4 Helixe während der Desensibilisierung, die auf eine neuartige Rolle dieser Segmente hinweist.

Zusammenfassend lässt sich sagen, dass wir in der präsentierten Arbeit verschiedene bestehende Methoden verfeinerten und so zum ersten Mal systematisch Strukturänderungen innerhalb der Transmembrandomäne von AMPA Rezeptoren während des *Gatings* erforschen und diese mit den funktionellen Eigenschaften des Ionenkanals in Verbindung bringen konnten.

English

Ionotropic glutamate receptors (iGluRs) are ligand-gated ion channels that are fundamental for healthy brain function. For these, the α-amino-3-hydroxyl-5-methyl-4-isoxazol-propionic acid (AMPA)-subtype glutamate receptor is a key mediator of fast excitatory synaptic transmission in the central nervous system. Their dysfunction is implied in numerous neurological disorders. Consequently, considerable efforts have been dedicated to study the structure and function of iGluRs. However, despite recent progress in resolving their structural architecture and dynamics, to date, few methods could resolve dynamics in the membrane domain.

Here, I present an optogenetic approach with the goal of elucidating receptor dynamics of the AMPA receptor transmembrane domain (TMD). This method involved site-specific incorporation of unnatural amino acid (UAA) photocrosslinkers by unnatural mutagenesis. Thus, we created photo-controllable AMPA receptors that can be regulated with high spatiotemporal precision, using light as the orthogonal input signal. We introduced the UAAs p-benzoyl-L-phenylalanine (BzF) and p-azido-L-phenylalanine (AzF) at 30 individual sites throughout the TMD of the AMPA receptor subunit GluA2. Electrophysiological recordings of outside-out patches from mammalian cells (HEK 293 cells) in combination with synchronised exposure to UV light via epi-illumination led to a series of optical effects on channel activity.

For 11 different mutants with either AzF or BzF incorporated into the GluA2 TMD, we identified light-induced changes of receptor activity, ranging from fast inhibition to potentiation. One of the most striking UV effects arose from the F579 site harbouring AzF in the middle of the M2 re-entrant helix of the TMD, which showed complex changes in receptor kinetics after crosslinking AzF upon UV illumination. Entry to desensitzation was slowed, but once entered the desensitized state became more stable and seemed to be conductive. These results suggest a distinct role of the M2 segment in channel gating, beyond its canonical role in ion selectivity. Moreover, our electrophysiological results complemented with biochemical experiments provided evidence for an interaction between the pre-M1 and the M4 helices during desensitization, indicating a novel role of these helices.

To summarize, in the presented work, we refined several existing methods and, for the first time, could systemically explore structural rearrangements of the transmembrane domain of AMPA receptors during gating and relate them to functional properties of the channel.

II Manteltext

1 State of research

The first sections provide an overview of the state of research in the field of glutamate receptors. Their structure and function, particularly of the transmembrane domain (TMD), are in the focus, as well as the employed method of unnatural amino acid (UAA) mutagenesis for investigating the TMD. The literature in these sections was confined to previous findings by which the presented publication was motivated.

1.1 The synapse

The human brain is arguably one of the most complicated structures in the universe. It contains around 80 billion neurons (Herculano-Houzel 2012), each with the ability to influence downstream cells. Understanding the brain's ability to convert external stimuli into memory and signals into behavior is a fundamental subject in neuroscience. In order to understand the complex circuitries of the brain, one has to decipher the underlying mechanism of neuronal cell communication. Chemical synapses convert the electrical signal that travels along the cell membrane into a chemical signal by releasing substances into the synaptic cleft. These so-called neurotransmitters that can be of excitatory or inhibitory nature bind to receptors of the downstream neuron, which then converts the signal back into an electrical response. Through these processes, synapses constitute fundamental elements of neuronal networks that enable the processing, encoding, and retrieval of information in the brain.

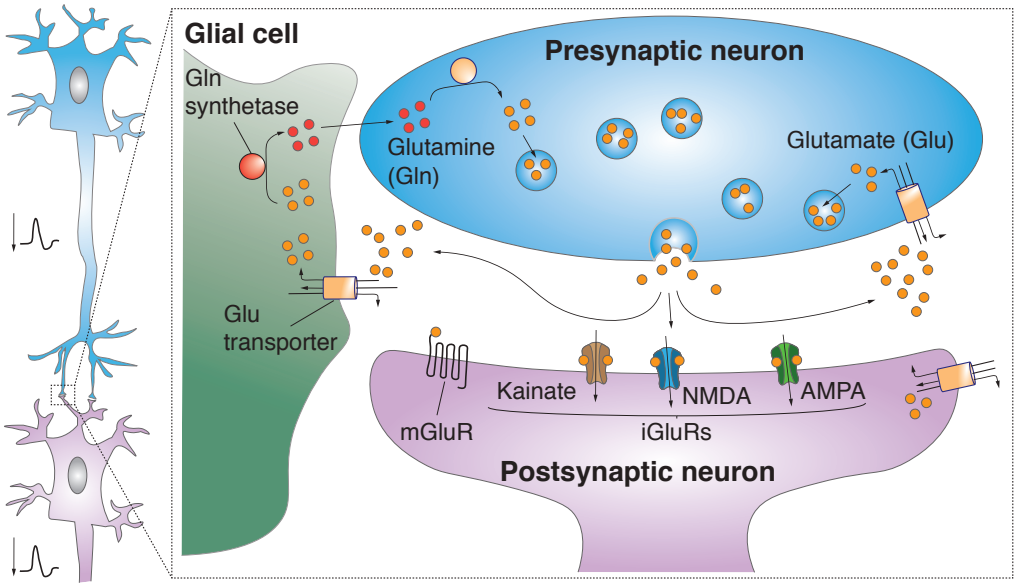

Figure 1: Glutamatergic synapse. Scheme of a simplified glutamatergic synapse. After release of glutamate (Glu) from the presynaptic neuron into the synaptic cleft, glutamte binds to glutamate receptors. At the postsynapse the chemical signal is translated via depolarisation of the postsynaptic membrane. Glia cells take glutamate up via specified glutamate transporters and convert them to glutamine (Gln). Glutamine in turn is taken up by the presynaptic neuron and converted back to glutamate. Glutamate molecules are stored in vesicles in the presynapse.

1.2 Ionotropic glutamate receptors

L-glutamate is the predominant excitatory neurotransmitter that mediates fast chemical signalling between nerve cells in the brain. At synapses, glutamate is released from presynaptic nerve terminals and binds to metabotropic or ionotropic glutamate receptors (iGluRs) embedded in the membrane of postsynaptic nerve terminals (Figure 1). Metabotropic glutamate receptors do not form ion channels and are instead coupled to other intracellular signalling systems or ion channels. The large iGluR family can be divided into three main subfamilies named according to their selective exogenous agonists; NMDA (N-methyl-D-aspartate), AMPA (α-amino-3-hydroxyl-5-methyl-4-isoxazol-propionic acid) and kainate receptors (reviewed in detail in Traynelis *et al.* 2010)

1.3 AMPA receptor subfamily

The AMPA receptor subfamily consists of a total of four subunits, GluA1 to GluA4 (formerly referred to as GluR1-GluR4), which combine as a dimer of dimers into homo- or heterotetrameric receptor complexes (Rosenmund *et al.* 1998; Mano and Teichberg 1998). The majority of the native AMPA receptors are GluA1/GluA2 or GluA2/GluA3 heterotetramers (Lu *et al.* 2009). However, subunit compositions of AMPA receptors varies during development and at different synapses (Tsuzuki *et al.* 2001; Schwenk *et al.* 2014). The various possible subunit combinations within each iGluR subfamily are further diversified by posttranscriptional and posttranslational modifications, which are common routes to modulate protein function. The posttranscriptional messenger ribonucleic acid (mRNA) editing of GluA2 occurs among other locations at the selectivity filter in the M2 loop and leads to the exchange of the neutral amino acid glutamine (Q) at position 607 (amino acid numbering refers to mature receptors that contain a 21 amino acid long signal peptide) with a positively charged arginine (R) (Sommer *et al.* 1990). As a consequence, AMPA receptors containing edited Q607R sites are impermeable to calcium and have reduced single-channel conductance level. Moreover, they have a linear current-voltage relationship, which is due to the absence of block by positively charged intracellular polyamines (reviewed in Traynelis *et al.* 2010). The GluA2 subunit is only expressed in the edited GluA2(R) form in native complexes and thus a critical determinant in AMPA receptor's contribution to synaptic responses (Lu *et al.* 2009). As a further mode to modulate their gating kinetics, AMPA receptors associate with auxiliary proteins, among which the most prominent are transmembrane AMPA receptor regulatory proteins (TARPs), the cornichon homologs and germ cell-specific gene 1-like protein (reviewed in Traynelis *et al.* 2010). Stargazin (also referred to as γ-2) is an extensively studied member of the TARP family and was shown to increase the steady-state current and decrease the deactivation and desensitization rate after associating with AMPA receptors (Jackson and Nicoll 2011). For the sake of simplicity not all regulation modes of AMPA receptor function will be discussed in detail.

Structure

Each of the four subunits (A, B, C and D, each 900 residues) has the same overall topology that consists of four discrete semiautonomous domains: 1) the large extracellular amino-terminal domain (ATD), 2) the extracellular ligand-binding domain (LBD) resembling a clamshell due to its two globular subdomains (D1 and D2), 3) the TMD comprised of four membrane segments (M1-M4), and 4) the intracellular carboxy-terminal domain (CTD). The conserved TMD is connected to the LBD through three short linkers (D1-M1, M3-D2 and D2-M4, Figure 2).
Structural information about iGluRs have emerged from sequence and structure comparisons, which established the unexpected kinship between the TMDs of iGluRs and K^+-selective channels (Galen Wo and Oswald 1995; Kuner *et al.* 2003). The missing link between the highly selective potassium channels and the relatively unselective cation channels of iGluRs, was clarified by the discovery of the prokaryotic glutamate-gated, K^+-selective receptor (GluR0), showing shared sequence and functional properties of the ion channel pore lining residues (Chen, Cui, *et al.* 1999). The topological structure has been confirmed by the first 3.6 Å resolution X-ray crystal structure of the full-length homotetrameric rat GluA2 receptor in the antagonist-bound, closed state (protein database identifier (PDB ID): 3kg2, Sobolevsky *et al.* 2009; note that the TMD is resolved at low resolution in this structure). This crystal structure provided for the first time the domain organisation of a membrane-spanning glutamate receptor. Thereby, both the ATD and LBD of the AMPA receptor extracellular domain possess a 2-fold rotational symmetry, while the TMD, which forms the ion channel, displays 4-fold symmetry. Furthermore, the subunits mismatch in their arrangement between the ATD and LBD so that subunits, which are proximal to each other in the ATD level (subunit pairs AB and CD), are distal at the LBD level, and vice versa.

Structure of the ion channel The three membrane-spanning α-helices (M1, M3 and M4) and the membrane-embedded re-entrant loop (M2) of each subunit assemble together to form the cation-selective ion pore of AMPA receptors (Sobolevsky *et al.* 2009). The linker region preceding the M1 makes a short helix (pre-M1) that is oriented at the exterior of the ion channel domain parallel to the lipid bilayer plane and forms a cuff around the ion channel pore. The M2 loops line the inner cavity of the pore and form the narrowest part, creating the selectivity filter controlling ion permeability. M3 helices line the outer cavity and shape a bundle crossing at the top of the TMD (Figure 2), which acts as a barrier to ion permeation (Sobolevsky *et al.* 2009). High structural homology with the gating domain of K^+ channels had already implied an important role for the M3 segment as an activation gate in NMDA receptors (Camino and Yellen 2001; Chang and Kuo 2008). Together with M1, M4 creates the peripheral part of the ion channel that faces the lipophilic membrane. Thereby, the M4 segment of one subunit primarily interacts with the membrane helices M1 and M3 of an adjacent subunit (Sobolevsky *et al.* 2009), indicating its crucial role in receptor assembly. The M4 segment has been shown to be required for tetramerization and surface expression of AMPA receptors (Salussolia, Corrales, *et al.* 2011; Salussolia, Gan, *et al.* 2013).

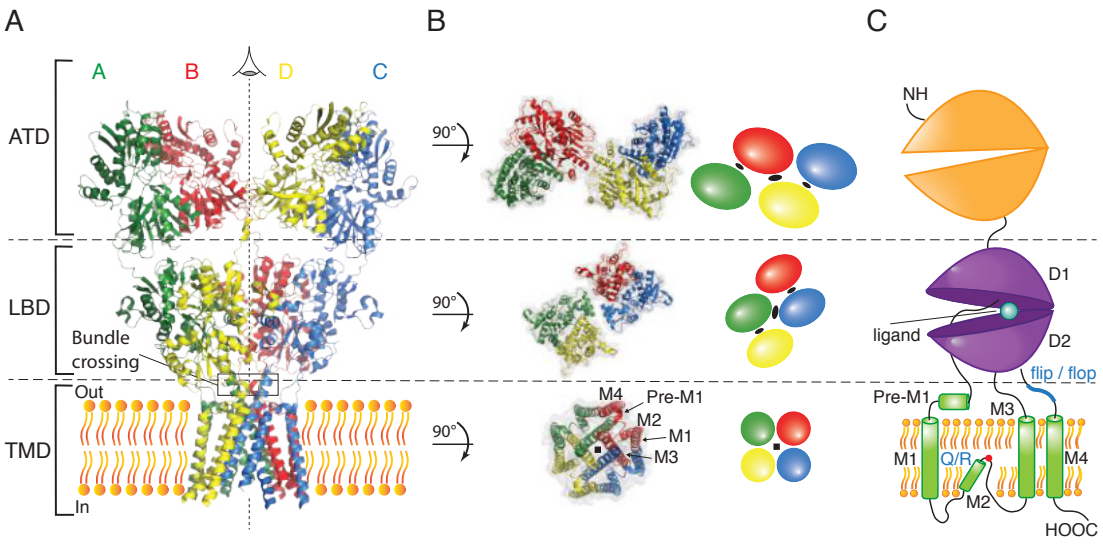

Figure 2: AMPA receptor structure and topology. **A)** Crystal structure of the tetrameric GluA2 receptor divided into three layers of ATD, LBD and CTD (PDB ID: 3kg2 drawn with PyMol, Sobolevsky *et al.* 2009). Individual subunits are coloured differently (A: green, B: red, C: blue and D: yellow). The lipid bilayer is indicated in orange. **B)** Subunits and individual domain layers are viewed from top down and colour-coded as in A). Black ovals and black square in the scheme illustrate the two-rotational symmetry of ATDs and LBDs (upper and center) and four-rotational symmetry of the TMD (lower), respectively. **C)** Schematic representation of one AMPA receptor subunit illustrating distinct elements of the receptor. The ATD in orange, LBD in purple being comprised of an upper lobe D1 and lower lobe D2, the TMD consisting of four transmembrane helices as green cylinders and a C-terminal tail.

Function

A hallmark of AMPA receptors is their ultra-fast activation in the sub-millisecond range through agonist application, like glutamate. Their following rapid and profound deactivation contribute to the rapid time course of synaptic currents (Figure 3A). The series of conformational changes in the AMPA receptor protein that comprise the opening and closing of the ion channel is referred to as gating.

Advances in structural biology have provided numerous snapshots of AMPA receptors in various closed-like conformations during gating, mainly displaying the extracellular domains with high resolution (reviewed in Pøhlsgaard *et al.* 2011; Mayer 2016). The caption of short-lived conformations during gating processes, involving rapid rearrangements within the ion permeation pathway upon agonist binding has been challenging. Recent work with cryo-electron microscopy, however, shed first light on conformational changes of the ion channel pore in a conducting state within the context of a full-length GluA2 receptor (Twomey *et al.* 2017). The gating process will be described in the following sections.

Activation Glutamate binding to the upper D1 lobe of the LBD results in a subsequent conformational change, the so-called clamshell closure in each of the four subunits (Zhang *et al.* 2008) (Figure 3B, middle dimer). Thereby, the D2 lobes move upward towards the D1 lobes and stabilizes the closed clamshell cleft conformation facilitated via interlobe hydrogen bonds (Armstrong and Gouaux 2000). Closure of the

ligand-binding domain drives a separation of the lower lobes of the LBD, resulting in a corkscrew-like rotation of the LBD assembly (Meyerson *et al.* 2014). Simultaneously, the upper lobes of the LBD pull down the ATD layer. The combination of agonist binding and clamshell closure exerts tension on the three linkers connecting the LBDs with the ion channel. The largest impact is seen on the M3-D2 linkers that pull M3 segments apart so that the ion pore opens, presumably resulting in an activated channel (Armstrong and Gouaux 2000; Twomey *et al.* 2017).

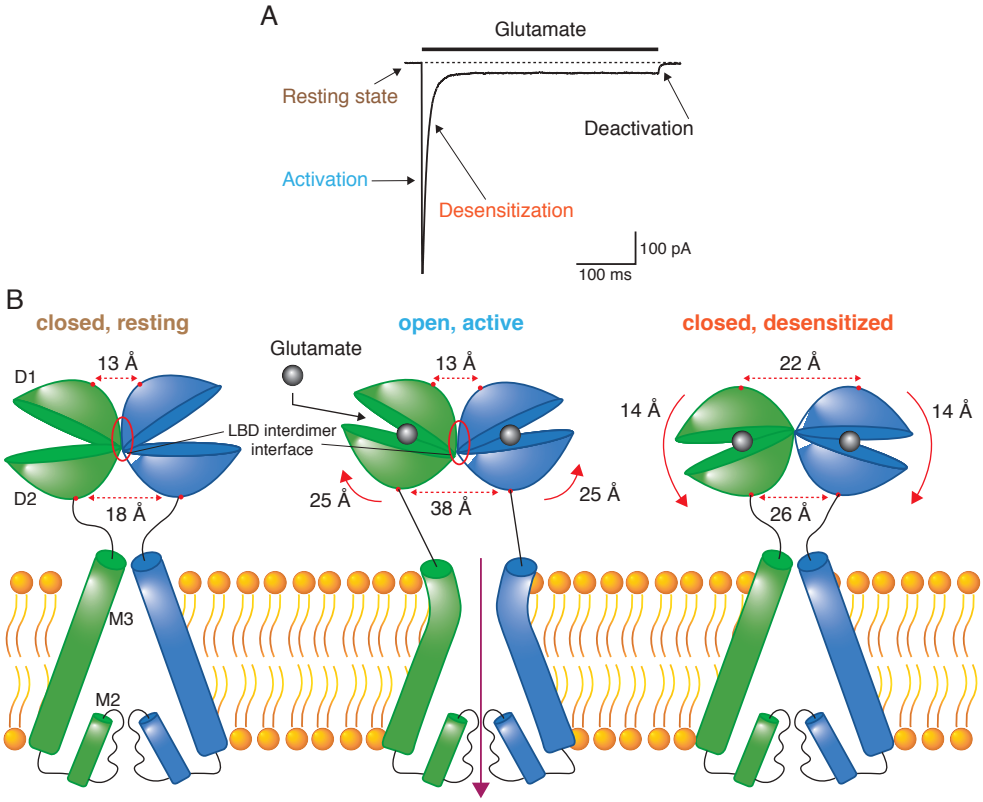

Figure 3: AMPA mobility during gating. **A)** Representative trace from outside-out patch recordings from human embryonic kidney (HEK) 293 cells that express rat GluA2, showing the gating steps in AMPA receptors after the 400 ms application of glutamate (black bar). **B)** Cartoon illustrating the mobility of AMPA receptor domains of LBD (D1 and D2) and TMD (M2 and M3) during the transition from the resting receptor (left) over the active state (middle) to the desensitized state (right). Red arrows and numbers (in Ångstrom) describe the involved conformational rearrangements during each transitional step. Distances between the linkers at D2 (P632) and between the tips of D1 (G739) at the top of the D1 lobes are taken from Sobolevsky (2015).

Deactivation and desensitization The energetically unfavourable strains exerted on the TMDs as well as on the LBD dimer interfaces during the open state are released by a conformational change through deactivation or desensitization. Whereas deactivation involves rapid reopening of the clamshell domains and subsequent unbinding of the agonist from the LBD, desensitization implies a D1-D1 interface rupture and rotation of individual LBDs, while maintaining their closed clamshell, agonist-bound state (Sun, Olson, *et al.* 2002; Horning and Mayer 2004; Twomey *et al.* 2017) (Figure 3B, right dimer). Both cases allow for the D2 domains and linkers to adopt a low-

energy non-conducting conformation, whereat desensitization occurs typically slower than deactivation. (Sun, Olson, *et al.* 2002; Armstrong, Jasti, *et al.* 2006). To return to the closed resting state, the receptor must undergo further conformational changes, a process referred to as recovery from desensitization. The crucial role of the D1 dimer interface is emphasized by actions of the positive allosteric modulator cyclothiazide (CTZ) as well as a lysine to tyrosine mutation in the LBD (in GluA2: L483Y) (Sun, Olson, *et al.* 2002). Both stabilize the D1-D1 interface between two LBDs, which blocks desensitization and traps the receptor in an active conformation.

Mobility of AMPA receptor domains during gating Mere structural results on extracellular (ATD and LBD) movements upon desensitization diverge substantially – ranging from a stable ATD dimer-dimer interface (Twomey *et al.* 2017) to ATDs displaying no dimer-dimer interactions (Meyerson *et al.* 2014). The large spectrum of ATD conformations captured in the desensitized state suggests a very dynamic ATD that is highly prone to interference. For instance, for common structural experiments, proteins were isolated from their native environment. This includes the membrane at which AMPA receptors sit and partner proteins with which they assemble, both of which likely account for protein integrity. Therefore, complementary results from biochemical and functional experiments as well as computational modelling probably serve as reliable evidences about receptor mobility during gating. For example, results from functional experiments using auxiliary proteins and crosslinkers as "molecular rulers" suggest a compact conformation of the extracellular domains (ATD and LBD) during gating, presumably held together by their associating auxiliary proteins (Baranovic and Plested 2018). In fact, more gating conformations, like numerous transient intermediate states of the LBD during activation (Baranovic, Chebli, *et al.* 2016; Lau *et al.* 2013) and surprisingly at rest (Plested and Mayer 2009), were resolved through functional crosslinking experiments. Hereby however, extracellular movements appear to be to a smaller extent than suggested by the available structural data.
Conclusions about the overall character of conformational changes of the ion channel during gating originated from comparison with open and closed K^+ channels (Galen Wo and Oswald 1995; Kuner *et al.* 2003). Furthermore, scanning mutagenesis in all TMD segments and the linkers that couple them to the LBD has shown specific elements important for gating (reviewed in Traynelis *et al.* 2010). A striking example presents the so-called Lurcher M3 mutation in a highly-conserved area of the M3 segment (the SYTANLAAF motif), which produced constitutively active channels (Yelshansky 2004; Sobolevsky *et al.* 2009). Recently, more detailed structural information was derived from a GluA2 homomer in complex with an auxiliary protein and bound to glutamate and CTZ (Twomey *et al.* 2017). Here, a kink at the bundle crossing in the SYTANLAAF motif (A618) was identified. This alanine in position 618 in M3 was found to make a turn upon glutamate binding, resulting in the side chain pointing away from the central pore axis (Twomey *et al.* 2017). Thus, the M3 segment is legitimately established as a key determinant for gating in glutamate receptors.
The M2 helices form numerous hydrophobic intra- and inter-subunit interactions with

M1 and M3 helices, presumably holding the ion channel core together. The narrowest part of the M2-loop extends their side chains towards the pore centre, which was recently suggested to create a second gate that needs to open up in order for the receptor to adapt a conductive state (Twomey *et al.* 2017).
In contrast, the contributions of pre-M1, M1 and M4 to gating remain vague. Notably, in the recent active structure of GluA2, the LBD-TMD linkers connecting to M1 (pre-M1) and M4 were observed to have altered distances of C_α-atoms of diagonal sites compared to closed structures, so that they presumalbly transmit the conformational changes of the LBD to open the ion channel pore (Twomey *et al.* 2017).
In any case, these structures represent snapshots and do not reveal the multiple structural factors that contribute to the energetics of conformational states and their transitions between them. Hence, the ambiguity in the dynamics of TMD segments still creates challenges to relate those to functional properties. In Poulsen *et al.* (2019), we aimed to illuminate dynamic changes within the TMD of AMPA receptors by incorporating light-sensitive UAAs into GluA2 subunits.

1.4 Introduction of UAAs into proteins

Conventional site-specific mutagenesis studies provide a practical approach to alter proteins and ultimately investigate the protein's structure-activity relationship. The expansion of the genetic code with UAAs bypasses the restriction of this technique to the 20 canonical amino acids. The use of UAAs with diverse chemical and biological reactivity provides an emerging tool to explore protein structure and dynamics or to control their activity in their native environment with high temporal and molecular precision. One possible way to perform site-specific mutagenesis with UAAs requires an evolved transfer RNA (tRNA) that uniquely recognizes the amber stop codon (UAG) and an orthogonal aminoacyl-tRNA synthetase (aaRS) that recognizes the UAA (see Method section 2.1).
In 1989, the first general method for UAA incorporation at an amber codon site was reported (Noren *et al.* 1989). Since then the method has been extensively extended and employed in proteins of bacteria, yeast, Xenopus laevis oocytes, mammalian cell lines, brain slices and whole organisms, including Drosophila and mice. Modified combinations of the evolved $tRNA^{Tyr}_{CUA}$/tyrosyl-tRNA synthetase (TyrRS) pair have been used to date in mammalian cells to sufficiently incorporate various UAAs with reactive side chains, including fluorescent, redox-active, photoactivatable or bioconjugative groups (reviewed in Chen, Lu, *et al.* 2017; Brown *et al.* 2018; Nödling *et al.* 2019). The $tRNA^{Tyr}_{CUA}$/TyrRS pair and the photoactive UAAs p-azido-L-phenylalanine (AzF) and p-benzoyl-L-phenylalanine (BzF) were utilized in the following work as previously probed in this laboratory (Klippenstein *et al.* 2014) and will be discussed hereafter.

1.5 Photocrosslinking mechanism of AzF and BzF

Both AzF and BzF are phenylalanine derivates and carry photoreactive groups, which can covalently crosslink after UV irradiation at 250-400nm and 350-365 nm, respectively

(Chin and Schultz 2002; Takimoto *et al.* 2009). The absorption wavelength of less energetic near-UV at around 350 nm induces comparatively the least damage to proteins or nucleic acids.

The sequence of the reaction pathway for AzF-based crosslinking is described as follows and illustrated in Figure 4. The excitation of the photoreactive azide functional group leads to a subsequent loss of dinitrogen (N_2) and generation of an excited state with free radicals (Schwyzer and Caviezel 1971). The generated nitrene can interact with various chemical groups: either it inserts into neighbouring active hydrogens of C-H or of N-H bonds or, in absence of a favourable interacting partner, it does not recombine, but expands its benzoyl ring. Ring expansion implies irreversible rearrangement into a ketenimine, which crosslinks less efficiently and is less specific regarding its crosslinking partners, such as water. Ketenimines can still react with polypeptides or proteins that contain amines (R-NH_2) or hydrogens (R-H). One of the major disadvantages of AzF is that it can react non-specifically even in the absence of UV illumination, probably due to the sensitivity of the azide group to daylight (Grunbeck *et al.* 2011).

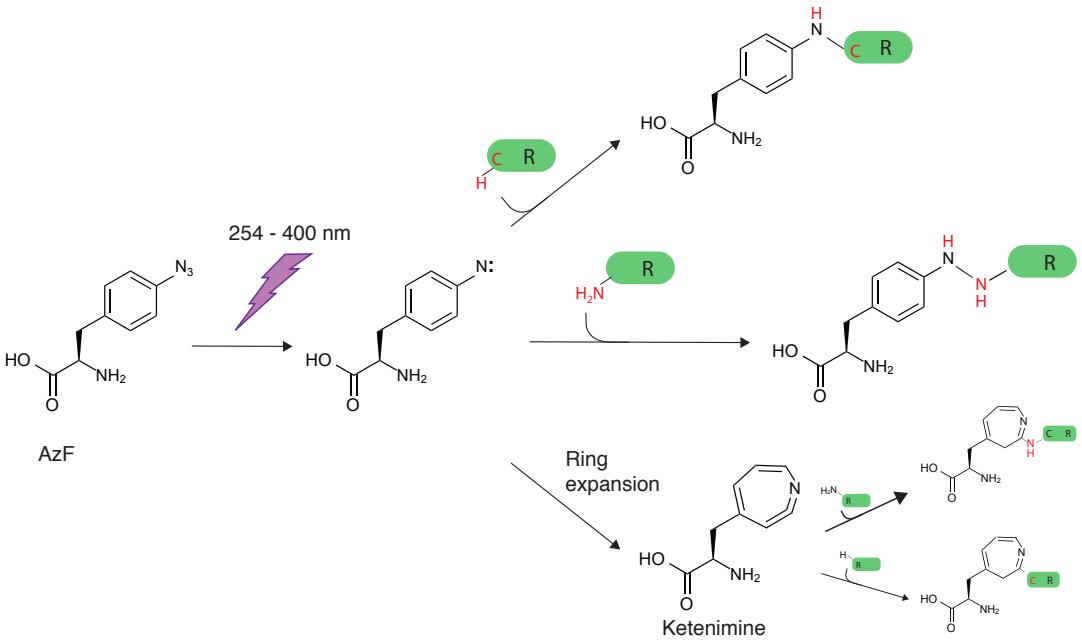

Figure 4: Crosslinking pathways of AzF. AzF is site-specifically introduced into a polypeptide chain. Illumination between 254 and 400 nm excites the photosensitive azide group of AzF, which forms into a short-lived reactive nitrene radical. If a favourable reaction partner is in close proximity, the nitrene can insert into hydrogens of a neighbouring molecule resulting in a covalent photocrosslink. If no suitable reaction partners is present, AzF expands its ring by incorporating the nitrene forming a ketenimine. Ketenimines can further react with polypeptides or proteins (R) that contain nucleophilic (R–NH_2) or active hydrogen (R–H) groups, whereby the first is the dominant pathway (indicated by a thicker arrow).

In contrast to AzF, BzF only has one photochemical reaction pathway (Ding and Horn 2001) (Figure 5): the absorption of a photon after irradation at 350 nm generates an excited state with a good quantum yield, followed by the abstraction of a hydrogen (H) from a carbohydrogen bond in close proximity, with a mild preference for α-carbon of a peptide backbone. This facilitates the covalent recombination of the resulting alkyl

and ketyl free radicals. Also, amino acid side chains or methyl groups of lipids can serve as H-donors. In the absence of a reactive partner, the crosslinking reaction fails, BzF returns to its basal state and can be excited again. While the advantages of BzF lie in its innoxious activation range and preference to crosslink to a series of carbohydrogen bonds, disadvantages are its bulkiness and hydrophobicity (Dorman and Prestwich 1994; Chin and Schultz 2002).

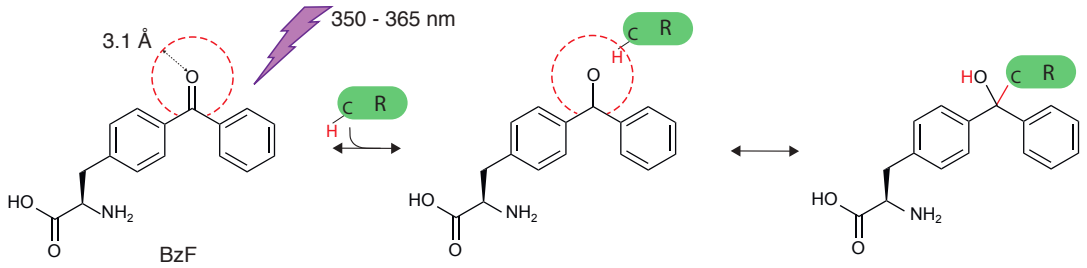

Figure 5: Crosslinking pathway of BzF. BzF is site-specifically introduced to a polypeptide chain. Illumination between 350 and 365 nm excites the photosensitive ketone group, which preferentially crosslinks to carbohydrogen (C-H) bonds within a 3.1 Å range (indicated in a red dotted circle). If a favourable reaction partner is in close proximity, BzF abstracts the hydrogen from the reaction partner. The resulting alkyl and ketyl free radicals facilitate the recombination into a covalent crosslink.

In Poulsen *et al.* (2019), we incorporated the photo-activatable UAAs, AzF and BzF, into the TMD of AMPA receptors, which are able to crosslink with nearby structures after UV activation. The cumulative illumination with UV allowed us to progressively perturb helical TMD structures and relate those sites to kinetic effects that we measured electrophysiologically.

2 Methodology

For our study in Poulsen *et al.* (2019), we used site-directed mutagenesis to site-specifically insert amber stop codons into the AMPA receptor subunit GluA2 with an unedited Q at 607. The introduction of orthogonal pairs of tRNA and either AzF-RS or BzF-RS into the heterologous expression system (HEK 293 cells) suppressed amber stop codons and incorporated AzF or BzF, respectively. Both are reactive after UV light irradiation and are able to form covalent bonds to nearby protein segments. By employing this method, we screened the TMD at 30 different sites. We characterized them functionally based on their light-induced modulations by means of fast-perfusion patch clamp electrophysiology coupled to a UV source. Thereby, the size of peak and steady-state currents, rate constants of desensitization, deactivation and recovery from desensitization as well as the modulation behaviour after UV crosslinking of the UAAs were particularly analyzed. Additionally, for most constructs, AMPA receptor expression was explored biochemically to verify the extent of amber stop codon rescue by the orthogonal tRNA/aaRS system. Simulated responses to glutamate for a kinetic model were generated to mimic the experimental effects and revealed a site close to the selectivity filter (F579), showing the likely complex modulations of channel kinetics after

UV irradiation. Upon these findings, further electrophysiological experiments with a focus on the temporal development of these modulations were pursued. Due to the resemblance in the UV-induced potentiation of currents from mutants in the pre-M1 and M4 helix, specifically-designed biochemical experiments were performed. Thereby, a cutting site for the tobacco-etch-virus (TEV) protease was inserted within the TMD in order to assess physical interactions based on crosslinking of the UAA between pre-M1 and M4 helices after UV exposure.
In the following, the theory of the two methodologies nonsense suppression mutagenesis and electrophysiology will be discussed in more detail. A detailed description of all methods applied for this study can be found in the supplement materials and methods section of Poulsen *et al.* (2019).

2.1 Molecular biology

Site-directed nonsense suppression mutagenesis

For protein biosynthesis, all organisms use the 64 nucleotide triplets (codons) each to encode for one of the 20 standard amino acids - including the three stop codons amber (UAG), opal (UGA) and ochre (UAA) that are defined by the universal genetic code. During translation, the aaRS recognizes its specific proteinogenic amino acid and catalyzes the aminoacylation to its corresponding tRNA. The loaded tRNA in turn possesses the correct anti-codon sequence according to the mRNA sequence and inserts the loaded amino acid at the right position (Watson 1964).
UAAs that usually carry synthetically modified, unique side chains can be added into any protein by introducing evolved pairs of bioorthogonal tRNA and aaRS into the host system - which is naturally not the organism from which neither the suppressor tRNA nor the aaRS was derived (illustrated in Figure 6) (Chen, Lu, *et al.* 2017; Brown *et al.* 2018). Those orthogonal tRNAs are no substrates to the host's native aaRSs, but function with the rest of its translational machinery, such as its ribosoms and translational factors. In the scope of conventional site-directed mutagenesis, one of the three stop codons is placed in the open reading frame into the gene of interest, which is later suppressed by the selected UAA via the orthogonal tRNA/aaRS pair. This method is also referred to as nonsense codon suppression mutagenesis because none of the introduced stop codons are suppressed by any of the 20 common amino acids. Traditionally, the amber stop codon is chosen, because in various eukaryotes it is natively the least frequently used among the three stop codons (Sun, Chen, *et al.* 2005). The UAA is supplied sufficiently to the cell via either supplementing the growth medium or directly injecting it into the cell. As a result, the modified protein contains the UAA at the genetically defined position. In absence of the UAA, or inefficient suppression, the amber codon will be read as a stop codon and translation will be terminated, resulting in a truncated, non-functional protein. An overview of this methodology is described in Figure 6. Strategies to maximize the efficiency of UAA incorporation includes the usage of tandemly repeated tRNA sequence on the expression vector and different promotors to enhance expression of the tRNA (Mukai *et al.* 2008). After years of adjustments to

overcome challenges in the evolution of efficient and genetically encoded nonsense codon suppression in mammalian cells, modified versions of a suppressor $tRNA^{Tyr}_{CUA}$ and its cognate TyrRS was employed first in 2002 (Sakamoto *et al.* 2002). This pair from Bacillus staerothermophilus and E.coli was particularly engineered directly in mammalian cells and was also used in Poulsen *et al.* (2019), enabled by kind gifts from Thomas Sakmar (Rockefeller University, New York). Although its development is technically demanding, nonsense suppression offers a versatile way to precisely manipulate protein function with new chemical groups at the molecular level. Obviously, the deployment of mammalian cells provide technical benefits, since most types of mammalian receptors can be efficiently expressed, but more importantly they allow for electrophysiological investigations of ion channels and receptors incorporated into the membrane.

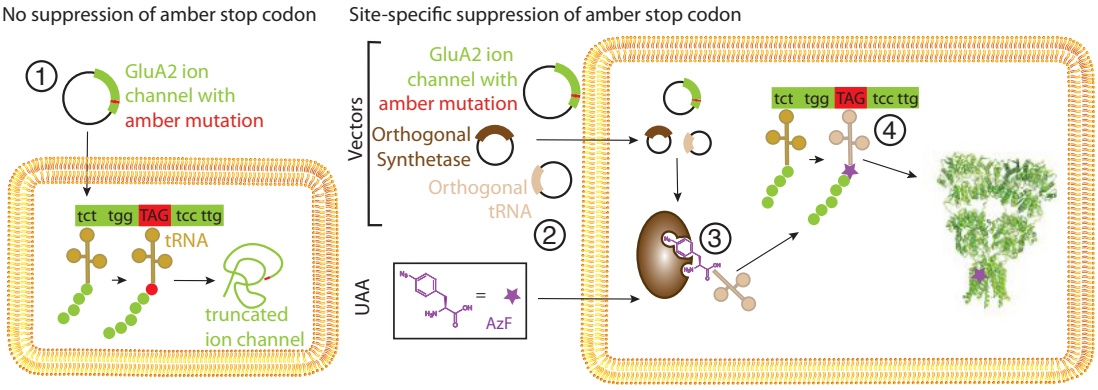

Figure 6: Genetically encoding photosensitive UAAs into ion channels. Schematic illustration of the key steps in nonsense suppression mutagenesis. Transfection of mammalian cells with only vectors carrying the genes for the protein of interest (green; AMPA receptor subunit GluA2) with introduced amber stop codons (TAGs, red) does not supress the TAG and leads to a truncated, non-functional protein ①. The TAG replaces a native codon at a permissive site within the GluA2 sequence. For site-specific suppression of the TAG, cells are co-transfected with vectors encoding for an orthogonal suppressor tRNA (beige)/aaRS (brown) and the photosensitive UAA (violet asteriks) are added to the cellular growth medium ②. Within the cell, the introduced synthetase specifically aminoacylates the supressor tRNA with the UAA ③. The UAA-carrying tRNA translates the TAG codon on the GluA2 nucleotide sequence by incorporating the UAA into the polypeptid chain ④. The full-length GluA2 homomeric AMPA receptor (PDB ID: 3kg2, Sobolevsky *et al.* 2009) folds into a functioning protein and carries the UAA site-specifically.

2.2 Electrophysiology

Electrophysiological questions deal with the bioelectric activity in living systems (e.g. neurons, cardiomyocytes and muscle fibers) in order to understand their physiological processes. In particular, the flow of ions and the mechanisms of action of various types of stimuli (electrical, chemical or mechanical) in neurons are of special interest. Since ions are not able to efficiently penetrate the lipid bilayer of cells by themselves, they are reliant on membrane-spanning proteins with water-filled channels or transporters. These proteins make use of the physiological electrochemical gradient of inorganic ions across the membrane. In order to measure ionic membrane currents mediated by ion channels while holding the membrane voltage at a set level, voltage clamp electro-

physiology can be employed. More precisely, in a basic voltage clamp, an intracellular recording electrode iteratively measures the membrane potential and, in case of changes due to current flow across the membrane, a second electrode adds the necessary current to achieve the command potential. The amount of the injected current allows for indirect measurements of currents of ions passing the ion channel under study. This technique is attributed to the work of Kenneth Cole and George Marmont (Marmont 1949) and paved the way for further experimental variations.

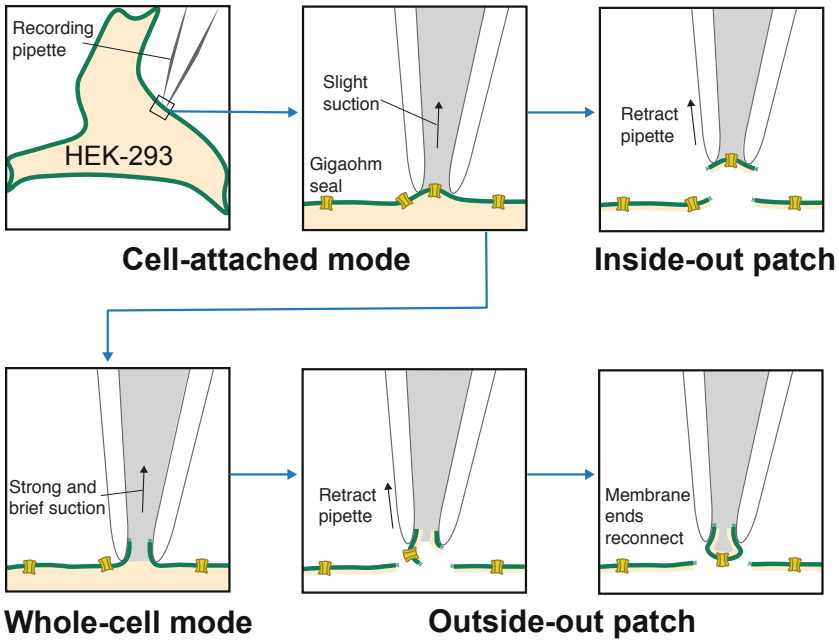

Figure 7: The four patch clamp configurations. Cell-attached: The pipette is pressed against the cell membrane and a mild suction is applied to gain a tight seal between the pipette and the membrane. Inside-out: Starting from the cell-attached mode, the pipette is gently retracted from cell and the patch is separated from the rest of the membrane. The cytoplasmic surface of the membrane is exposed to the bath solution. Whole-cell: Starting from the cell-attached mode, another brief but strong suction is applied in order to rupture the cell membrane and to gain access to the cytoplasm of the whole cell. Outside-out: Starting from the whole-cell mode, the pipette is gently retracted resulting in two small pieces of membrane that reconnect and form a small vesicle with the cytoplasmic surface facing the pipette solution.

Outside-out patch clamp electrophysiology

As a refined version of the voltage clamp, the patch clamp technique offers an extremely versatile application for studying electrophysiological properties of excitable membranes by using only one fine micropipette to form a high resistance seal on biological membranes. The use of only one pipette instead of two as in the votlage clamp setup is enabled through the use of non-polarizable, reversible silver/silver chloride microelectrodes that exchange electrons for chloride ions in solution. After its development by Erwin Neher and Bert Sakmann in the late 1970s (Neher *et al.* 1978), tight-seal recordings have been customized in various ways depending on the investigational approach and can be applied to virtually all biological preparations. The patch clamp technique enables high-resolution recordings in the millisecond and picoampere range not only of

whole cells, but also of micrometer sized cellular patches. It therefore allows to study the fast gating kinetics of ligand-gated ion channels from a set of or, most intriguingly, single ion channels.
In order to gain high-resistance seals in the gigaohm range, a thin glass pipette with a polished tip of 1 µm diameter is approached to the cell membrane and a slight suction is applied. A gigaohm seal prevents the leakage of ions between the pipette and membrane and results in electrical isolation of the membrane, which reduces the signal-to-noise ratio immensely and allows the recording of very small currents. Depending on the research interest, the experimenter can use different configurations during recordings (cell-attached, inside-out, whole-cell or outside-out patch mode), which are described in Figure 7. The pipette is filled with a salt solution, resembling that normally found in either the extracellular fluid (cell-attached or inside-out mode) or the intracellular fluid (whole-cell or outside-out mode). For this work, only the outside-patch mode was used, which facilitates the fast application of the agonist to the excised patches with glutamate-gated AMPA receptors using a sophisticated fast-perfusion system. Rapid perfusion electrophysiology involves a four-barrel glass-perfusion tool that allows the exchange of the bath and glutamate solutions within less than 1 ms. Thus, the fast kinetic properties of AMPA receptors can be addressed with needed quality and speed of the solution exchange.

3 Essential new results

For the first time, in Poulsen *et al.* (2019), we performed genetically encoded UAA mutagenesis in the membrane domain of AMPA receptors using specific orthogonal tRNA/AzF-RS or tRNA/BzF-RS pairs. Due to the high molecular and temporal precision of this approach, we were able to probe the TMD at 30 different sites, a region that is usually difficult to access and to track structurally. We used UV light to progressively perturb receptor structure at specific sites, incorporating photoreactive AzF or BzF, and concomitantly followed resulting changes in GluA2 receptor kinetics. Using this method, we were able to identify dynamic parts of the TMD that move during gating.
Three key discoveries were obtained. Firstly, we verified the applicability of this method in the AMPA receptor TMD. We could show that the incremental perturbations of the structure were site-specific. The magnitude of kinetic changes did not only depend on the membrane helix into which the UAA was inserted, but was also local to the specific amino acid site. This is also underlined by the fact that we found specific and comparable effects upon UV treatment at neighbouring amino acid substitutions (e.g. F515BzF and F518BzF in pre-M1; V539AzF, F541AzF and L542AzF in M1 or Y797AzF and I798AzF in M4; Figure 3 and Figure 5 in Poulsen *et al.* 2019). We were also able to control crosslinking by the photoactivation dose - the duration and intensity of applied UV light - so that less crosslinking occurred with smaller applied UV dose (SI Appendix, Figure S3 in Poulsen *et al.* 2019).
Secondly, the most striking new insight was that M2 likely acts as a second ion channel gate. Disruption of the M2 segment through UV activation of F579AzF critically

influenced channel gating in multiple ways. Our kinetic analysis showed that the selectivity filter is coupled to all aspects of receptor function – slowing rate constants for desensitization, deactivation, recovery from desensitization and decays after the steady-state current as well as increasing the steady-state current, more than almost any other residue in the protein. Interestingly, these UV-driven effects of F579AzF had different onsets and developed asynchronously with increasing UV exposures, underlining its complex role in multiple functional states. The wide-ranging role of the M2 helix in channel gating was additionally emphasized by kinetic models, in which both the open and the desensitized state had to be destabilized in order to mimick the observed kinetic changes.

Thirdly, we suggest a physical interaction between pre-M1 and M4 segments within a subunit. The interaction was found to control desensitization. This understanding originated from our results from biochemical experiments together with the coherence in the photoactivating effects during electrophysiology at selected pre-M1 and M4 sites (F515BzF and L518BzF, Y797AzF and I798AzF, respectively; Figure 3 and Figure 4 in Poulsen *et al.* 2019). The UV effect of these structurally close sites stood out from the rest of the investigated sites, because only at these sites UV crosslinking of the UAAs led to potentiating effects on channel function.

4 Further scientific questions

In the presented work, we employed genetically encoded UAAs, AzF or BzF, to map conformational changes during gating. The incorporation of photoreactive UAAs identified positions that, after UV-driven photocrosslinking, result in inactivation or potentiation of the receptor's response to glutamate. Overall, the findings support the idea of complex rearrangements during gating with each individual membrane helix moving upon glutamate binding to the AMPA receptor.

While previous studies, in which most experiments have been carried out in NMDA receptors, have suggested a role of all transmembrane helices in channel gating, only M2 and M3 helices of AMPA receptors have been assigned to defined roles (reviewed in Traynelis *et al.* 2010). Here, we suggest that also the transmembrane helices pre-M1 and M4 rearrange during desensitization. Furthermore, we propose that M2 functions as a second ion channel gate, which surpasses its commonly approved function as a pure ion selectivity filter. In particular, photoactivation of the M2-F579AzF mutant seems to make the desensitized receptor conductive, which is in line with the findings of a very recent, but not yet peer-reviewed work (Coombs *et al.* 2019). By means of fluctuation analysis, single-channel recording and kinetic modelling, they demonstrated that the steady-state current is mainly mediated by "conducting desensitized" receptors. These new findings might encourage more functional studies that aim to specifically pinpoint the involvement of the transmembrane segments, especially the M2 segment, in channel kinetics.

Experiments with heteromeric receptors carrying UAAs (e.g. wild-type GluA1(Q) and GluA2(R)$_{\mathrm{UAA}}$) might be reasonable anchor points to expand the study. How efficacious are the UV-induced kinetic effects conveyed in heteromeric receptors? Are these effects

comparable to effects that we see in homomeric GluA2 receptors? Or more specifically, how many UAA-carrying subunits are necessary to show the strong UV-induced kinetic effects? Identified inactivating sites, where UV application abolished more than 90% of current response in homomeric AMPA receptors (e.g. F608AzF, Y533AzF, F584AzF), might give more insight into the inactivation efficacy rendered by UAAs when assessed in heteromeric GluA1(Q):GluA2(R)$_{\mathrm{UAA}}$ receptors. For this, the UAAs can be incorporated only in the GluA2 subunit and glutamate-induced currents measured in the presence of the polyamine spermine in order to isolate heteromeric UAA-containing receptors at positive potentials. Straight IV-curves reflect little contamination with homomeric receptors.

As a further step, investigations of kinetic effects upon UV crosslinking on homomeric and heteromeric receptors in complex with auxiliary proteins (e.g. stargazing or other TARPs), which modulate channel gating, might contribute to the understanding of receptor function during the gating pathway. The lack of high-resolution structures of the TARP loops that are thought to interact with the receptor hampers the full understanding of how TARPs and AMPA receptors associate. Functional experiments using UAA crosslinking at presumable association sites might reveal molecular interaction loci.

To investigate the crosslinking event itself, single-channel recordings of UAA mutants can be conducted. What are the outcomes of crosslinking events at the single channel level regarding their kinetics or time-course? Are the crosslinking effects homogenous or heterogenous? Moreover, the assessment of UV-induced changes in the occupancy of different sub-conductance states via single-channel recordings of the M2-F579AzF mutant might give insight into how the M2 helix contribute to gating as a second gate. As we have already observed in outside-out patches of the M4-I798AzF mutant (Suppl. Figure 10, Poulsen *et al.* 2019), UV exposures increased the prevalence of long-lived bursts with high open-probability.

Investigations of receptor function in molecular terms aid to understand the gating of AMPA receptor complexes in detail as well the modes of regulation that fine-tune their function *in vivo*, which is a key in drug design. Despite rapid advances in methodological approaches though, these methods often fail to provide sufficient structural, spatial and temporal resolution in order to relate the receptor dynamics to their action under normal and diseased conditions. The findings of Poulsen *et al.* (2019) identified key moving parts of the ion channel and thus expanded the scope of putative pharmacological sites. Relating those functionally important sites of the receptor to how these sites can be altered by drugs or in disease conditions provides the foundation for future translational studies.

Since this study was conducted in the heterologous expression system of HEK 293 cells, the implementation of this method in neurons, where AMPA receptors are expressed naturally, is obvious. Co-cultures of primary neurons and astrocytes or brain slices are one step closer to the *in vivo* world, yet their genetic manipulation also already more challenging. However, the successful *in vivo* expression of light-activatable potassium channels using UAAs have already been demonstrated in mouse neocortex (Kang

et al. 2013), raising promising prospects of its feasibility. Since AMPA receptors are well-known to play a pivotal role in forming the cellular basis for cognition, perception, learning and memory (Malenka and Bear 2004), an interesting approach might be memory formation studies *in vivo*, in which a set of AMPA receptors are silenced by light at a defined timepoint. More particularly, for example the mutant F608AzF that showed the most pronounced and fastest inactivation can be used to completely ablate AMPA receptor currents in those studies. Once implemented in neurons, using the key advantage of this approach to tightly control the receptor's action temporally and molecularly, is likely to provide more insight into the physiological role of AMPA receptors in the brain.

5 References

Armstrong, N. and E. Gouaux (2000). "Mechanisms for Activation and Antagonism of an AMPA-Sensitive Glutamate Receptor". *Neuron* 28.1, pp. 165–181. DOI: 10.1016/S0896-6273(00)00094-5.

Armstrong, N., J. Jasti, M. Beich-Frandsen, and E. Gouaux (2006). "Measurement of conformational changes accompanying desensitization in an ionotropic glutamate receptor." *Cell* 127.1, pp. 85–97. DOI: 10.1016/j.cell.2006.08.037.

Baranovic, J., M. Chebli, H. Salazar, A. L. Carbone, K. Faelber, A. Y. Lau, O. Daumke, and A. J. R. Plested (2016). "Dynamics of the Ligand Binding Domain Layer during AMPA Receptor Activation". *Biophysical Journal* 110.4, pp. 896–911. DOI: 10.1016/j.bpj.2015.12.033.

Baranovic, J. and A. J. Plested (2018). "Auxiliary subunits keep AMPA receptors compact during activation and desensitization". *eLIFE* 91, pp. 399–404.

Brown, W., J. Liu, and A. Deiters (2018). "Genetic Code Expansion in Animals". *ACS Chemical Biology* 13.9, pp. 2375–2386. DOI: 10.1021/acschembio.8b00520.

Camino, D. del and G. Yellen (2001). "Tight Steric Closure at the Intracellular Activation Gate of a Voltage-Gated K+ Channel". *Neuron* 32.4, pp. 649–656. DOI: 10.1016/S0896-6273(01)00487-1.

Chang, H.-R. and C.-C. Kuo (2008). "The Activation Gate and Gating Mechanism of the NMDA Receptor". *Journal of Neuroscience* 28.7, pp. 1546–1556. DOI: 10.1523/jneurosci.3485-07.2008.

Chen, G.-Q., C. Cui, M. L. Mayer, and E. Gouaux (1999). "Functional characterization of a potassium-selective prokaryotic glutamate receptor". 402.December.

Chen, Y., L. Lu, and S. Ye (2017). "Genetic Code Expansion and Optoproteomics." *The Yale journal of biology and medicine* 90.4, pp. 599–610.

Chin, J. W. and P. G. Schultz (2002). "In Vivo Photocrosslinking with Unnatural Amino Acid Mutagenesis - Schultz_chembiochem02.pdf". 11, pp. 1135–1137.

Coombs, I. D., D. Soto, T. P. McGee, M. G. Gold, M. Farrant, and S. G. Cull-Candy (2019). "Homomeric Q/R edited AMPA receptors conduct when desensitized". *bioRxiv*. DOI: 10.1101/595009.

Ding, S. and R. Horn (2001). "Slow Photo-Cross-Linking Kinetics of Benzophenone-Labeled Voltage Sensors of Ion Channels†". DOI: 10.1021/BI010709Y.

Dorman, G. and G. D. Prestwich (1994). "Benzophenone photophores in biochemistry". *Biochemistry* 33.19, pp. 5661–5673.

Galen Wo, Z. and R. E. Oswald (1995). "Unraveling the modular design of glutamate-gated ion channels". *Trends in Neurosciences* 18.4, pp. 161–168. DOI: 10.1016/0166-2236(95)93895-5.

Grunbeck, A., T. Huber, P. Sachdev, and T. P. Sakmar (2011). "Mapping the Ligand-binding Site on a GPCR Using Genetically-encoded Photocrosslinkers NIH Public Access". *Biochemistry* 50.17, pp. 3411–3413. DOI: 10.1021/bi200214r.

Herculano-Houzel, S. (2012). "The remarkable, yet not extraordinary, human brain as a scaled-up primate brain and its associated cost". *Proceedings of the National Academy of Sciences* 109.Supplement_1, pp. 10661–10668. DOI: 10.1073/pnas.1201895109.

Horning, M. S. and M. L. Mayer (2004). "Regulation of AMPA Receptor Gating by Ligand Binding Core Dimers". *Neuron* 41.3, pp. 379–388. DOI: 10.1016/S0896-6273(04)00018-2.

Jackson, A. C. and R. A. Nicoll (2011). "The Expanding Social Network of Ionotropic Glutamate Receptors: TARPs and Other Transmembrane Auxiliary Subunits". *Neuron* 70.2, pp. 178–199. DOI: 10.1016/j.neuron.2011.04.007.

Kang, J.-Y., D. Kawaguchi, I. Coin, Z. Xiang, D. D. O'Leary, P. A. Slesinger, and L. Wang (2013). "In Vivo Expression of a Light-Activatable Potassium Channel Using Unnatural Amino Acids". *Neuron* 80.2, pp. 358–370. DOI: 10.1016/j.neuron.2013.08.016.

Klippenstein, V., V. Ghisi, M. Wietstruk, and A. J. R. Plested (2014). "Photoinactivation of Glutamate Receptors by Genetically Encoded Unnatural Amino Acids". *The Journal of Neuroscience* 34.3, pp. 980–991. DOI: 10.1523/JNEUROSCI.3725-13.2014.

Kuner, T., P. H. Seeburg, and H. Robert Guy (2003). "A common architecture for K+ channels and ionotropic glutamate receptors?": *Trends in Neurosciences* 26.1, pp. 27–32. DOI: 10.1016/S0166-2236(02)00010-3.

Lau, A. Y., H. Salazar, L. Blachowicz, V. Ghisi, A. J. R. Plested, and B. Roux (2013). "A Conformational intermediate in glutamate receptor activation". *Neuron* 79.3, pp. 792–503. DOI: 10.1016/j.neuron.2013.06.003.

Lu, W., Y. Shi, A. C. Jackson, K. Bjorgan, M. J. During, R. Sprengel, P. H. Seeburg, and R. A. Nicoll (2009). "Subunit composition of synaptic AMPA receptors revealed by a single-cell genetic approach." *Neuron* 62.2, pp. 254–68. DOI: 10.1016/j.neuron.2009.02.027.

Malenka, R. C. and M. F. Bear (2004). "LTP and LTD: an embarrassment of riches." *Neuron* 44.1, pp. 5–21. DOI: 10.1016/j.neuron.2004.09.012.

Mano, I. and V. I. Teichberg (1998). "A tetrameric subunit stoichiometry for a glutamate receptor-channel complex." *Neuroreport* 9.2, pp. 327–31.

Marmont, G. (1949). "Studies on the axon membrane. I. A new method". *Journal of cellular and comparative physiology* 34.3, pp. 351–382.

Mayer, M. L. (2016). "Structural biology of glutamate receptor ion channel complexes". *Current Opinion in Structural Biology* 41.Figure 1, pp. 119–127. DOI: 10.1016/j.sbi.2016.07.002.

Meyerson, J. R., J. Kumar, S. Chittori, P. Rao, J. Pierson, A. Bartesaghi, M. L. Mayer, and S. Subramaniam (2014). "Structural mechanism of glutamate receptor activation and desensitization". *Nature* advance on.7522. DOI: 10.1038/nature13603.

Mukai, T., T. Kobayashi, N. Hino, T. Yanagisawa, K. Sakamoto, and S. Yokoyama (2008). "Adding l-lysine derivatives to the genetic code of mammalian cells with engineered pyrrolysyl-tRNA synthetases". *Biochemical and biophysical research communications* 371.4, pp. 818–822.

Neher, E., B. Sakmann, and J. H. Steinbach (1978). "The extracellular patch clamp: A method for resolving currents through individual open channels in biological membranes". *Pflügers Archiv* 375.2, pp. 219–228. DOI: 10.1007/BF00584247.

Nödling, A. R., L. A. Spear, T. L. Williams, L. Y. Luk, and Y.-H. Tsai (2019). "Using genetically incorporated unnatural amino acids to control protein functions in mammalian cells". *Essays In Biochemistry* 0.March, EBC20180042. DOI: 10.1042/EBC20180042.

Noren, C. J., S. J. Anthony-Cahill, M. C. Griffith, and P. G. Schultz (1989). "A general method for site-specific incorporation of unnatural amino acids into proteins." *Science (New York, N.Y.)* 244.4901, pp. 182–8. DOI: 10.1126/SCIENCE.2649980.

Plested, A. J. R. and M. L. Mayer (2009). "AMPA receptor ligand binding domain mobility revealed by functional cross linking." *The Journal of neuroscience : the official journal of the Society for Neuroscience* 29.38, pp. 11912–23. DOI: 10.1523/JNEUROSCI.2971-09.2009.

Pøhlsgaard, J., K. Frydenvang, U. Madsen, and J. S. Kastrup (2011). "Lessons from more than 80 structures of the GluA2 ligand-binding domain in complex with agonists, antagonists and allosteric modulators". *Neuropharmacology* 60.1. High Resolution, pp. 135–150. DOI: https://doi.org/10.1016/j.neuropharm.2010.08.004.

Poulsen, M. H., A. Poshtiban, V. Klippenstein, V. Ghisi, and P. Andrew (2019). "Gating modules of the AMPA receptor pore domain revealed by unnatural amino acid mutagenesis". *Proceedings of the National Academy of Sciences*, p. 449181. DOI: 10.1101/449181.

Rosenmund, C., Y. Stern-Bach, and C. F. Stevens (1998). "The tetrameric structure of a glutamate receptor channel." *Science (New York, N.Y.)* 280.5369, pp. 1596–9.

Sakamoto, K., A. Hayashi, A. Sakamoto, D. Kiga, H. Nakayama, A. Soma, T. Kobayashi, M. Kitabatake, K. Takio, K. Saito, M. Shirouzu, I. Hirao, and S. Yokoyama (2002). "Site-specific incorporation of unnatural amino acids into proteins in mammalian cells". *Nuc* 794.21, pp. 215–228. DOI: 10.1007/978-1-61779-331-8_13.

Salussolia, C. L., A. Corrales, I. Talukder, R. Kazi, G. Akgul, M. Bowen, and L. P. Wollmuth (2011). "Interaction of the M4 segment with other transmembrane segments is required for surface expression of mammalian α-amino-3-hydroxy-5-methyl-4-isoxazolepropionic acid (AMPA) receptors." *The Journal of biological chemistry* 286.46, pp. 40205–18. DOI: 10.1074/jbc.M111.268839.

Salussolia, C. L., Q. Gan, R. Kazi, P. Singh, J. Allopenna, H. Furukawa, and L. P. Wollmuth (2013). "A eukaryotic specific transmembrane segment is required for tetramerization in AMPA receptors." *The Journal of neuroscience : the official journal of the Society for Neuroscience* 33.23, pp. 9840–5. DOI: 10.1523/JNEUROSCI.2626-12.2013.

Schwenk, J., D. Baehrens, A. Haupt, W. Bildl, S. Boudkkazi, J. Roeper, B. Fakler, and U. Schulte (2014). "Regional diversity and developmental dynamics of the AMPA-receptor proteome in the mammalian brain". *Neuron* 84.1, pp. 41–54. DOI: 10.1016/j.neuron.2014.08.044.

Schwyzer, R. and M. Caviezel (1971). "p-Azido-L-phenylalanine: a Photo-affinity ' Probe ' Related to Tyrosine". *Helvetica Chimica Acta* 54.143.

Sobolevsky, A. I. (2015). "Structure and gating of tetrameric glutamate receptors". *The Journal of Physiology* 593.1, pp. 29–38. DOI: 10.1113/jphysiol.2013.264911.

Sobolevsky, A. I., M. P. Rosconi, and E. Gouaux (2009). "X-ray structure, symmetry and mechanism of an AMPA-subtype glutamate receptor." *Nature* 462.7274, pp. 745–56. DOI: 10.1038/nature08624.

Sommer, B., K. Keinänen, T. A. Verdoorn, W. Wisden, N. Burnashev, A. Herb, M. Köhler, T. Takagi, B. Sakmann, and P. H. Seeburg (1990). "Flip and flop: a cell-specific functional switch in glutamate-operated channels of the CNS." *Science (New York, N.Y.)* 249.4976, pp. 1580–5.

Sun, J., M. Chen, J. Xu, and J. Luo (2005). "Relationships among stop codon usage bias, its context, isochores, and gene expression level in various eukaryotes". *Journal of Molecular Evolution* 61.4, pp. 437–444. DOI: 10.1007/s00239-004-0277-3.

Sun, Y., R. Olson, M. Horning, N. Armstrong, M. Mayer, and E. Gouaux (2002). "Mechanism of glutamate receptor desensitization". *Nature* 417.6886, pp. 245–253. DOI: 10.1038/417245a.

Takimoto, J. K., K. L. Adams, Z. Xiang, and L. Wang (2009). "Improving orthogonal tRNA-synthetase recognition for efficient unnatural amino acid incorporation and application in mammalian cells". *Molecular BioSystems* 5.9, pp. 931–934. DOI: 10.1039/b904228h.

Traynelis, S. F., L. P. Wollmuth, C. J. McBain, F. S. Menniti, K. M. Vance, K. K. Ogden, K. B. Hansen, H. Yuan, S. J. Myers, and R. Dingledine (2010). "Glutamate receptor ion channels: structure, regulation, and function." *Pharmacological reviews* 62.3, pp. 405–96. DOI: 10.1124/pr.109.002451.

Tsuzuki, K., B. Lambolez, J. Rossier, and S. Ozawa (2001). "Absolute quantification of AMPA receptor subunit mRNAs in single hippocampal neurons." *Journal of neurochemistry* 77.6, pp. 1650–9.

Twomey, E. C., M. V. Yelshanskaya, R. A. Grassucci, J. Frank, and A. I. Sobolevsky (2017). "Channel opening and gating mechanism in AMPA-subtype glutamate receptors". DOI: 10.1038/nature23479.

Watson, J. (1964). "The synthesis of proteins upon ribosomes." *Bulletin de la société de chimie biologique* 46, pp. 1399–1425.

Yelshansky, M. V. (2004). "Block of AMPA Receptor Desensitization by a Point Mutation outside the Ligand-Binding Domain". *Journal of Neuroscience* 24.20, pp. 4728–4736. DOI: 10.1523/jneurosci.0757-04.2004.

Zhang, W., Y. Cho, E. Lolis, and J. R. Howe (2008). "Structural and Single-Channel Results Indicate That the Rates of Ligand Binding Domain Closing and Opening Directly Impact AMPA Receptor Gating". *Journal of Neuroscience* 28.4, pp. 932–943. DOI: 10.1523/jneurosci.3309-07.2008.

III Affidavit

„Ich, Anahita Poshtiban, versichere an Eides statt durch meine eigenhändige Unterschrift, dass ich die vorgelegte Dissertation mit dem Thema: „Gating modules of the AMPA receptor pore domain revealed by unnatural amino acid mutagenesis“ als geteilter Erstautor und ohne nicht offengelegte Hilfe Dritter verfasst und keine anderen als die angegebenen Quellen und Hilfsmittel genutzt habe. Alle Stellen, die wörtlich oder dem Sinne nach auf Publikationen oder Vorträgen anderer Autoren beruhen, sind als solche in korrekter Zitierung kenntlich gemacht. Die Abschnitte zu Methodik (insbesondere praktische Arbeiten, Laborbestimmungen, statistische Aufarbeitung) und Resultaten (insbesondere Abbildungen, Graphiken und Tabellen) werden von mir verantwortet.
Meine Anteile an etwaigen Publikationen zu dieser Dissertation entsprechen denen, die in der untenstehenden gemeinsamen Erklärung mit dem/der Betreuer/in, angegeben sind. Für sämtliche im Rahmen der Dissertation entstandenen Publikationen wurden die Richtlinien des ICMJE (International Committee of Medical Journal Editors; www.icmje.og) zur Autorenschaft eingehalten. Ich erkläre ferner, dass mir die Satzung der Charité – Universitätsmedizin Berlin zur Sicherung Guter Wissenschaftlicher Praxis bekannt ist und ich mich zur Einhaltung dieser Satzung verpflichte.
Die Bedeutung dieser eidesstattlichen Versicherung und die strafrechtlichen Folgen einer unwahren eidesstattlichen Versicherung (§§156, 161 des Strafgesetzbuches) sind mir bekannt und bewusst.“

Berlin, den 31. Juli 2019 Unterschrift

.....

IV Author Contribution

Autoren: Mette H. Poulsen *, Anahita Poshtiban *, Viktoria Klippenstein, Valentina Ghisi, Andrew J.R. Plested (* geteilte Erstautorenschaft)
Titel: Gating modules of the AMPA receptor pore domain revealed by unnatural amino acid mutagenesis
Fachzeitschrift: Proceedings of the National Academy of Sciences of the United States of America (PNAS)
Erscheinungsdatum: 18. Juni 2019
Detaillierter Beitrag im Einzelnen:

Ich, Anahita Poshtiban, habe das hier zugrunde liegende Forschungsergebnis der Beschreibung von Gatingmodulen in der Transmembrandomäne (TMD) von AMPA-Rezeptoren des Subtyps GluA2 mit Hilfe von UV-sensitiven unnatürlicher Aminosäure-Mutagenese im Zuge meiner Promotion wie folgt aufgezeigt (**Gating modules of the AMPA receptor pore domain revealed by unnatural amino acid mutagenesis**):

1) Für die biochemischen Experimente haben Dr. Mette Poulsen und ich die Transfektionen der HEK293T Zellen mit den jeweiligen Mutanten und teilweise deren UV-Behandlung durchgeführt (siehe Supplementary Materials and methods - Biochemistry).

2) Elektrophysiologie - nähere Erläuterung zur experimentellen Herangehensweise: Für das große Screening der TMD von GluA2-Rezeptoren wurden insgesamt 30 verschiedene ortsspezifische Mutationen innerhalb der TMD elektrophysiologisch getestet und auf UV-Effekte überprüft (UV-Effekt = Änderungen in den kinetischen Gatingeigenschaften des Rezeptors nach UV-Aktivierung der eingebauten unnatürlichen Aminosäure). Die Mutationen wurde unter folgenden verschiedenen Bedingungen gemessen (nicht alle Mutanten wurden unter allen Bedingungen untersucht): mit den eingebauten unnatürlichen Aminosäuren i) AzF oder ii)BzF, im Hintergrund der LY-Mutation mit iii) AzF oder iv) BzF, oder als negative Kontrollexperimente ohne eine unnatürliche Aminosäure, aber im Hintergrund der v) AzF-Synthetase oder vi) BzF-Synthetase im Transfektionsmedium. Daraus ergaben sich insgesamt 84 verschiedene Bedingungen, die elektrophysiologisch untersucht wurden. Aus den getesteten 30 Mutanten waren 11 Mutanten (AzF und/oder BzF) sensitiv auf UV-Beleuchtung, d.h. sie veränderten ihre kinetischen Eigenschaften nach UV-Applikation (siehe *Fig. 1C*). Diese 11 Mutanten, der GluA2-Wildtyp, sowie 3 Null-Mutanten (Null-Mutante = Mutante mit einer eingebauten unnatürlichen Aminosäure, die ihre kinetischen Eigenschaften nach UV-Applikation nicht veränderte) wurden genauer elektrophysiologisch untersucht und analysiert. Insgesamt ergab dies 56 verschiedene Bedingungen.
Aus der Reihe dieser 11 Mutanten mit UV-Effekten und der 4 Kontrollen war ich verantwortlich für die eigenständige Planung und Durchführung elektrophysiologischer Messungen von insgesamt 42 verschiedenen Bedingungen (aus 56 Bedingungen) und für die Analyse von insgesamt 231 Messungen/Patches (aus 460 Messungen). Pro Bedin-

gung wurden etwa 3-25 Messungen/Patches aufgenommen. Folgende Mutanten bzw. Bedingungen wurden von mir untersucht:

AzF: WT, WT-LY, F515, L518, F531, F531-LY, Y533-LY, F574, L577, L577-LY, F579, F579-LY, F584-LY, W605, F608, F796, F796-LY, Y797, Y797-LY, I798, I798-LY.
BzF: WT, WT-LY, F515, L518, F574, F584, L577, Y797, Y797-LY.
Negative Kontrolle (AzF): F515, L518, F531, Y533, F541, L577, F579, F584, Y797, I798.
Negative Kontrolle (BzF): L577, Y797.

Für die elektrophysiologischen Experimente habe ich HEK293 Zellen mit den jeweiligen Mutanten transfiziert und die unnatürliche Aminosäure (AzF oder BzF oder keines der beiden zur Kontrolle) dem Medium hinzugefügt (siehe *Supplementary Materials and methods - Cell culture and transfection*). Daraufhin habe ich die Mutante/Bedingung alleinverantwortlich funktionell mittels der Outside-Out Patch-Clamping-Methode untersucht. Hierbei habe ich ihre kinetischen Gatingeigenschaften wie die Desensitisierung-, Deaktivierungs- und Erholungsrate von der Desensitisierung jeweils vor und nach der Applikation von UV-Licht gemessen (siehe *Supplementary Materials and methods - Electrophysiology*).
Aus diesen 42 Bedingungen übernahm ich für folgende 17 Bedingungen alle in die Publikation einbezogenen Messungen komplett alleinverantwortlich:

AzF: WT-LY, L518, L577, Y797-LY, I798, I798-LY.
BzF: WT-LY, L577, Y797-LY.
Negative Kontrolle (AzF): F515, L518, F531, F541, F579, I798.
Negative Kontrolle (BzF): L577, Y797.

Dr. Mette Poulsen war komplett alleinverantwortlich für 14 Bedingungen. Die elektrophysiologischen Messungen für die restlichen 25 Bedingungen wurden zwischen mir und Dr. Mette Poulsen zu etwa gleichen Anteilen zum Vergleich der UV-induzierten Ergebnisse geteilt. Alle ersten funktionellen Ergebnisse des Screenings der GluA2-TMD stellten wir in den Abbildungen 1, 2 und 3, in den Zusatzabbildungen S2, S3 und S5 und den Tabellen S2, S3, S4 und S5 dar.

Hinweis 1: Für die Publikation setzten wir uns einen hohen Qualitätsstandard bei den einbezogenen Messungen, z.B. zogen wir nur die Aufnahmen ein, die eine stabile Baseline über mehrere Aufnahmeminuten gewährleisteten. Daher liegt die Anzahl der tatsächlich aufgenommenen Patches sehr viel höher als die oben angegeben 460 Messungen. Besonders bei einigen der Mutanten mit UV-Effekten war die Aufrechterhaltung einer stabilen Baseline erschwert. Auch das in der Elektrophysiologie verbreitete „Rundown“ (d.h. Abnahme der Glutamat-induzierten Peak-Amplitude aus unbekanntem Grund) führte zum Ausschluss vieler Messungen.

Hinweis 2: Das Teilen von einigen Mutanten/Bedingungen zwischen mir und Dr. Mette Poulsen, besonders derer, die erschwert zu messen waren, diente zur gegenseitigen Qualitäts- und Reproduzierbarkeitskontrolle der UV-spezifischen Ergebnisse. Außerdem ist zu beachten, dass es sich um ein Screening mit einer großen Anzahl von Bedingungen handelt, welches wir mit der anspruchsvollen und zeitaufwendigen Outside-out Patch-Clamping Methode (eine Nicht-High-Throughput Methode) durchgeführt haben.

3) Ich war verantwortlich für die weiterführenden Folgeanalysen des Screenings zur Identifikation einer Beziehung zwischen den gemessenen funktionellen UV-Effekten und der Struktur der TMD:

- Ich führte strukturelle Distanzmessungen in der 3D-Grafiksoftware PyMol für Abbildung S7, S8A und S8D durch. Hierbei maß ich die Distanzen der Cα-Atompositionen der jeweiligen ortsspezifischen Mutante zwischen offener und geschlossener Ionenkanalstrukturen (siehe *Supplementary Materials and methods – Structural analysis*).

- Ich klassifizierte die Mutanten gemäß ihren spezifischen UV-Effekten in funktionelle Gruppen und übertrug diese auf die GluA2-Proteinstruktur in PyMol für Abbildung 5 B und Zusatzabbildung S8 A.

- Ich erstellte Plots aus den verschiedenen UV-induzierten Gatingeigenschaften der Mutanten für Abbildungen 5 A und 6 A und Zusatzabbildungen S6, S7, S8 D.

4) Die Analyse für Abbildung 6 A gab Hinweise auf eine Beziehung zwischen den identifizierten UV-Effekten der Mutanten und deren strukturellen Positionen in der TMD. Der Plot hob bestimmte TMD-Segmente als Gatingmodule hervor und deutete v.a. auf eine mögliche besondere und bisher nicht beschriebene Rolle des Selektivitätsfilters (Position M2-F579AzF). Daraufhin erfolgten folgende Untersuchungen:

- Prof. Andrew Plested war verantwortlich für den Vergleich dieser Zusammenhänge mit kinetischen Simulationen für Abbildung 6 B-E.

- Zur experimentellen Bestätigung der komplexen und neuen Rolle von M2-F579AzF war ich alleinverantwortlich für das Design der darauffolgenden elektrophysiologischen Experimente. Ich untersuchte die kinetischen Eigenschaften von F579AzF nicht nur vor und nach saturierter UV-Exposition wie im großen Screening, sondern auch dazwischen, also nach „subsaturierter“ UV-Exposition, um die zeitliche Entwicklung der Veränderung seiner kinetischen Eigenschaften genauer verfolgen zu können. Ich war auch alleinverantwortlich für die Durchführung und Analyse der Messungen an F579AzF und stellte meine Ergebnisse in den Abbildungen 7 und 8 A und in der Zusatzabbildung S9 dar.

Hinweis: Durch die oben beschriebenen ausgiebigen Folgeanalysen des Screenings und der daraus resultierenden Entdeckung und Belegung einer bisher nicht beschriebenen Rolle des Selektivitätsfilters (M2-F579) als Gatingmodul hat das Manuskript an Wichtigkeit in dem Forschungsgebiet von Glutamat-Rezeptoren gewonnen und wurde

wahrscheinlich auf Grund dessen einer Publikation in einem Top-Journal würdig.

5) Ich war verantwortlich für die Identifikation des Burst-Effekts von I798AzF aus den von mir durchgeführten elektrophysiologischen Experimenten für Zusatzabbildung S10.

6) Ich erstellte die Abbildungen 5, 6 A, 7 und 8 A, und die Zusatzabbildungen S6, S7, S8 A und D, S9 und S10.

7) Dr. Mette Poulsen, Prof. Andrew Plested und ich haben zu etwa gleichen Anteilen das Original-Manuskripts der Publikation entwickelt und geschrieben. Alle Autoren überprüften das Manuskript.

Journal Data Filtered By: **Selected JCR Year: 2017** Selected Editions: SCIE,SSCI Selected Categories: **"MULTIDISCIPLINARY SCIENCES"** Selected Category Scheme: WoS

Gesamtanzahl: 64 Journale

Rank	Full Journal Title	Total Cites	Journal Impact Factor	Eigenfactor Score
1	NATURE	710,766	41.577	1.355810
2	SCIENCE	645,132	41.058	1.127160
3	Nature Communications	178,348	12.353	0.926560
4	Science Advances	10,194	11.511	0.057080
5	PROCEEDINGS OF THE NATIONAL ACADEMY OF SCIENCES OF THE UNITED STATES OF AMERICA	637,268	9.504	1.108220
6	National Science Review	952	9.408	0.004340
7	GigaScience	1,694	7.267	0.011030
8	Scientific Data	1,567	5.305	0.008550
9	Journal of Advanced Research	1,843	4.327	0.003820
10	Annals of the New York Academy of Sciences	46,160	4.277	0.033270
11	Science Bulletin	1,952	4.136	0.005900
12	Scientific Reports	192,841	4.122	0.718960
13	Journal of the Royal Society Interface	11,357	3.355	0.030960
14	Research Synthesis Methods	1,374	3.218	0.006030
15	PLoS One	582,877	2.766	1.862350
16	PHILOSOPHICAL TRANSACTIONS OF THE ROYAL SOCIETY A-MATHEMATICAL PHYSICAL AND ENGINEERING SCIENCES	17,807	2.746	0.028220
17	Royal Society Open Science	2,145	2.504	0.009260
18	PROCEEDINGS OF THE ROYAL SOCIETY A-MATHEMATICAL PHYSICAL AND ENGINEERING SCIENCES	17,157	2.410	0.018270
19	PeerJ	7,377	2.118	0.031600
20	NPJ Microgravity	94	2.000	0.000350
21	SCIENCE AND ENGINEERING ETHICS	1,496	1.859	0.002520
22	COMPLEXITY	1,369	1.829	0.002380
23	Science of Nature	324	1.789	0.001260

Gating modules of the AMPA receptor pore domain revealed by unnatural amino acid mutagenesis

Mette H. Poulsen[a,b,1,2], Anahita Poshtiban[a,b,c,1], Viktoria Klippenstein[a,b], Valentina Ghisi[a,b], and Andrew J. R. Plested[a,b,c,3]

[a]Molecular Neuroscience and Biophysics, Leibniz Forschungsinstitut für Molekulare Pharmakologie, 13125 Berlin, Germany; [b]NeuroCure, Charité Universitätsmedizin, 10117 Berlin, Germany; and [c]Institute of Biology, Cellular Biophysics, Humboldt Universität zu Berlin, 10115 Berlin, Germany

Edited by Ehud Y. Isacoff, University of California, Berkeley, CA, and approved May 24, 2019 (received for review November 2, 2018)

Ionotropic glutamate receptors (iGluRs) are responsible for fast synaptic transmission throughout the vertebrate nervous system. Conformational changes of the transmembrane domain (TMD) underlying ion channel activation and desensitization remain poorly understood. Here, we explored the dynamics of the TMD of α-amino-3-hydroxy-5-methyl-4-isoxazolepropionic acid (AMPA)-type iGluRs using genetically encoded unnatural amino acid (UAA) photocross-linkers, p-benzoyl-L-phenylalanine (BzF) and p-azido-L-phenylalanine (AzF). We introduced these UAAs at sites throughout the TMD of the GluA2 receptor and characterized the mutants in patch-clamp recordings, exposing them to glutamate and ultraviolet (UV) light. This approach revealed a range of optical effects on the activity of mutant receptors. We found evidence for an interaction between the Pre-M1 and the M4 TMD helix during desensitization. Photoactivation at F579AzF, a residue behind the selectivity filter in the M2 segment, had extraordinarily broad effects on gating and desensitization. This observation suggests coupling to other parts of the receptor and like in other tetrameric ion channels, selectivity filter gating.

glutamate receptor | selectivity filter | membrane protein

The α-amino-3-hydroxy-5-methyl-4-isoxazolepropionic acid (AMPA)-type glutamate receptor (AMPAR), in common with other ionotropic glutamate receptors (iGluRs), includes glutamate binding domains that connect to a transmembrane ion channel pore. Glutamate binding activates the receptor and opens the channel. Despite the apparent simplicity of this activation principle, the geometries of the receptor involved in different activation states are unclear. Recently, two structures from cryoelectron microscopy of the active AMPAR in complex with the auxiliary subunit Stargazin were published (1, 2). However, it remains unclear whether these structures represent fully open channels or are, perhaps, conformations corresponding to subconductance openings. We currently lack an active-state structure for other subtypes of iGluR.

Numerous reports have investigated the structure and function of extracellular domains of AMPARs using pharmacological compounds and/or mutational studies (3, 4). These studies suggested that desensitization and gating of AMPARs are principally regulated by the conformation of the ligand binding domain (LBD) (5), with at most a limited role for amino terminal domains in controlling AMPAR function (6, 7). In contrast to the extracellular domains, comparatively few studies have examined the functional dynamics of the AMPAR pore domain. One reason for this deficit is the lack of approaches for capturing movements within the transmembrane domain (TMD). Nonetheless, mutagenesis on the ion channel extracellular collar (8), the linkers between the LBD and TMD (9), and the "Lurcher" mutation in the M3 segment (10) have all provided clues toward the necessary movements.

In tetrameric ion channels, two complementary mechanisms of channel gating have been described. The helical bundle crossing occludes the extracellular end of the AMPAR pore in closed channel structures solved to date (M3 in iGluRs, S6 in potassium channels), which is also tightly occluded in Shaker potassium channels (11) and sodium channels (12). However, other tetrameric channels, including CNG, BK, and MthK, exhibit either a partially or fully open bundle crossing, with the selectivity filter acting as a principal gate (13–16). Even in tetrameric ion channels with minimal architectures, such as KcsA, selectivity filter gating underlying C-type inactivation can be coupled to voltage and opening of the bundle crossing, including gating hysteresis (17–20). Cysteine accessibility experiments in AMPARs are consistent with a gate at the bundle crossing between resting and open states (21), but only two sites in the M3 helix of AMPARs could be studied with membrane impermeant reagents. In contrast, a similar approach in the *N*-methyl-D-aspartate (NMDA) receptor (NMDAR) is consistent with a lower gate (22). Moreover, coupling between the selectivity filter and bundle crossing has not been investigated and may occur in other functional states.

Real-time analysis of receptor activity coupled to chemical cross-linking has the potential to identify sites that have a state-dependent disruption of channel gating. Several techniques to produce cross-links between parts of the receptor have been used, including disulfide bonding and the introduction of artificial metal binding sites to bridge subunits (21, 23–26). However, these approaches require solvent access to the sites of interest,

Significance

Glutamate receptors are membrane proteins that incorporate an ion channel domain. Binding of the neurotransmitter glutamate opens the ion channel, a key event in neurotransmission, but also triggers other dynamic changes in protein structure. We have probed these changes in the membrane domain using light-sensitive unnatural amino acids at 30 sites. This approach allowed us to use ultraviolet light to progressively perturb receptor structure local to specified sites. We identify the collar domain and the selectivity filter, a structure that determines the permeant ion species, as exerting unexpectedly broad control over the gating and desensitization of the receptor. This work supports the idea of a dynamic selectivity filter, which in turn, may facilitate pharmacological intervention at this essential receptor.

Author contributions: M.H.P., A. Poshtiban, V.K., V.G., and A. J. R. Plested designed research; M.H.P., A. Poshtiban, V.K., V.G., and A. J. R. Plested performed research; A. J. R. Plested contributed new reagents/analytic tools; M.H.P., A. Poshtiban, V.K., V.G., and A. J. R. Plested analyzed data; and M.H.P., A. Poshtiban, and A. J. R. Plested wrote the paper.

The authors declare no conflict of interest.

This article is a PNAS Direct Submission.

[1]M.H.P. and A. Poshtiban contributed equally to this work.

[2]Present address: Department of Drug Design and Pharmacology, University of Copenhagen, 2100 Copenhagen, Denmark.

[3]To whom correspondence may be addressed. Email: plested@fmp-berlin.de.

This article contains supporting information online at www.pnas.org/lookup/suppl/doi:10.1073/pnas.1818845116/-/DCSupplemental.

which is not feasible for many sites within the membrane-embedded channel domain.

To study the TMD at arbitrary sites with the aim of mapping the channel gating pathway in an unbiased way, we exploited unnatural amino acids (UAAs). We chose UAAs that are reactive after irradiation with ultraviolet (UV) light and that consequently form covalent bonds to nearby protein segments. We used a well-characterized genetic encoding method that has been shown to be highly selective and potent in experiments on 7-TM metabotropic receptors and rhodopsin (27–30), potassium channels (31, 32), and NMDA and AMPA subtypes of iGluRs (33–35). We inserted individual TAG (amber) stop codons throughout the TMD of the AMPAR subtype GluA2, rescued these introduced stop codons with p-benzoyl-L-phenylalanine (BzF) or p-azido-L-phenylalanine (AzF), and measured the effects of UV exposures on currents induced by glutamate. We also assessed physical cross-linking with protein biochemistry. These experiments, in concert with analysis of kinetic mechanisms, revealed an unforeseen extent of control of gating and desensitization by both core and peripheral elements of the ion channel domain.

Results

We hypothesized that structural elements outside the bundle crossing are critically involved in the channel gating reaction. To investigate this hypothesis, we selected 30 sites in the TMD of GluA2 to insert either of the two photoactivatable UAAs, AzF or BzF (Fig. 1*A*). The size of AzF is comparable with that of tyrosine (Y) and tryptophan (W), whereas BzF is bulkier (Fig. 1*B*). Although we preferred to replace aromatic residues, we selected other amino acids at sites that allowed us to cover all four membrane segments, M1–M4. After I798 in M4, rescue became leakier, and we were concerned that receptors truncated at the TAG stop codon might form functional ion channels. The results for these mutants are listed in *SI Appendix*, Tables S6 and S7. In subsequent figures, we include only the results up to I798 in M4 (24 sites). In Fig. 1, we outline the basic results of the electrophysiological, optical activation, and biochemical experiments for 24 sites. This survey already permits some conclusions about the utility and chemistry of UAA cross-linking in the transmembrane segments.

We first found insertion sites in all helices at which we could rescue functional channels at the plasma membrane. At 19 of 24 sites listed in Fig. 1, typical fast glutamate-activated currents could be recorded from channels harboring AzF. At 11 of these sites, BzF also produced functional channels. There were no sites at which the bulkier BzF could preferentially rescue channel function. Viewed on the basis of crystal structures of GluA2, another aspect of functional rescue was apparent. Sites that readily accommodated both amino acids tended to be found at the circumference of the membrane domain, whereas sites that produced nonfunctional channels for both AzF and BzF tended to be centrally located around the channel pore. An intermediate layer of sites was permissive for AzF alone (Fig. 1*D*).

At 9 of 19 sites rescued by AzF, we could detect a robust alteration of channel gating on exposure to UV light. We explore in more detail the nature of these changes below. Strikingly, we could not determine a robust effect of BzF photoactivation on currents for any of the sites tested, except for the peripheral sites at F515 and L518 in the "Pre-M1" helix, which are likely to be outside the plasma membrane. We did detect a weak effect of UV exposure when BzF was incorporated in the M2 helix at position 577; however, the effect was hard to separate from current rundown. The absence of distinct UV-induced changes on receptor function for constructs containing BzF is surprising in light of experiments in which membrane domains in voltage-gated channels were cross-linked with Benzophenone (36). Most sites that we tried are likely shielded from the pore and water therein. However, BzF reacts poorly with water, and therefore, it seems unlikely that water is required for its reactivity with surrounding protein (37). The only water-accessible sites in the AMPAR pore domain are likely to be in the M3 helix (38–40), and BzF failed to produce functional channels at these sites.

A possible confounder of these results was that a lack of glutamate-activated current expression was because of a failure

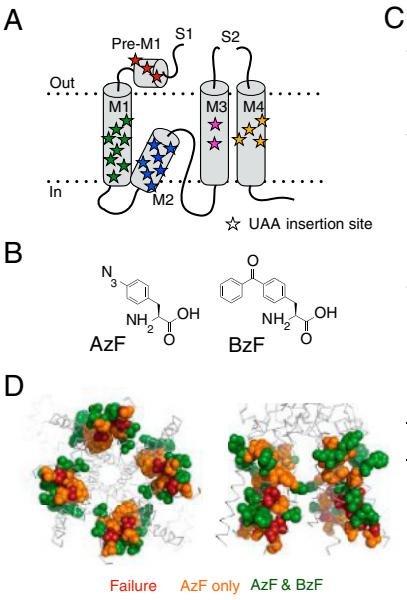

C

Site		Protein rescue		Current		UV effect	
		AzF	BzF	AzF	BzF	AzF	BzF
F515	Pre-M1	•	•	✔	✔	★	★
F517	Pre-M1	/	/	✔	✖	✱	/
L518	Pre-M1	/	/	✔	✔	✱	★
F531	M1	•	•	✔	✔	✱	✱
Y533	M1	•	•	✔	✖	★	/
S537	M1	•	•	✖	✖	/	/
V539	M1	•	•	✔	✔	✱	✱
L540	M1	•	•	✖	✖	/	/
F541	M1	•	•	✔	✔	✱	✱
L542	M1	•	•	✔	✔	✱	✱
S544	M1	/	/	✔	✖	/	/
F571	M2	/	/	✔	✖	/	/
G572	M2	/	/	✖	✖	/	/
F574	M2	/	/	✔	✔	?	✱
N575	M2	/	/	✖	✖	/	/
L577	M2	•	•	✔	✔	★	?
F579	M2	•	•	✔	✖	★	/
F584	M2	•	•	✔	✔	★	✱
W605	M3	•	•	✔	✖	?	/
F608	M3	•	•	✔	✖	★	/
V795	M4	/	/	✖	✖	/	/
F796	M4	•	•	✔	✖	★	/
Y797	M4	•	•	✔	✔	★	✱
I798	M4	•	/	✔	✔	★	/

✔ : Glu-induced currents
★ : UV-specific effect
? : Possible UV-specific effect
✖ : No currents
✱ : No effect after UV
/ : No test

Fig. 1. Site-specific incorporation of AzF and BzF. (*A*) Cartoon of the TMD of a glutamate receptor subunit. Stars indicate UAA insertion sites. (*B*) Chemical structures of AzF and BzF. (*C*) Summary of expression characteristics, electrophysiology, and UV effects. Color coding of sites is the same as in *A*. Western blot analysis indicated that "rescue" of translation was successful for all of the constructs tested, denoted by filled green circles. A backslash indicates no test. Under "Current," green ticks indicate constructs for which glutamate-induced currents could be detected, and red crosses indicate constructs where no currents could be recorded for AzF or BzF incorporation. Receptors were exposed to UV light in the resting and/or desensitized state during electrophysiological recordings. Green filled stars indicate a specific UV-triggered effect, and red asterisks indicate no apparent effect of UV light. Forward slashes indicate constructs [GluA2-F574AzF (M2), -W605AzF (M3), -L577BzF (M2), and -F584BzF (M2)] where large rundown in the current amplitude precluded quantitation of any possible slow concurrent UV effects. Recordings of the I798BzF (M4) mutant had rapid rundown and leak currents that were larger than usual. The currents for F571AzF and S544AzF mutants (both M2) were too small to permit analysis of UV-driven effects (indicated by a backslash). Incorporation of AzF in six additional sites in M4 was tested, but no UV effect was observed (*SI Appendix*, Tables S6 and S7) (*D*) Representation of insertion sites shown as color-coded spheres in a GluA2 crystal structure (PDB ID code 3kg2). Red spheres indicate failure of both AzF and BzF to rescue functional receptors (Current column in *C*), whereas orange spheres indicate successful insertion of only AzF, and green spheres indicate successful insertion of both AzF and BzF.

to translate the polypeptide chain. Therefore, we performed biochemical experiments to assess rescue of expression. These experiments confirmed that, for both AzF and BzF, inclusion of the UAAs and the requisite synthetase and exogenous transfer ribonucleic acid (tRNA) was sufficient to strongly enrich expression of the full-length subunits (Fig. 1*C* and *SI Appendix*, Fig. S1 and Table S1) (range of 5- to 3,500-fold increase in band intensity for 15 mutants). These ratios mean that, in the very worst case, 80% of subunits were UAA mutants. This fraction is likely an underestimate, because the synthetases that we used are more efficient at incorporating their cognate UAAs than endogenous amino acids, like Tyrosine (29). On average, wild-type receptors showed no change in expression level in the presence of the UAAs and the incorporation machinery. These experiments do not provide information about the maturity of the tetrameric form of the receptor or about surface expression but do indicate that deficits due to UAAs were either in assembly and/or gating, not in a gross absence of translation of the full-length polypeptide chain.

To assess whether functional receptors rescued by AzF and BzF were valid congeners of wild-type receptors, we assessed their desensitization, deactivation, and recovery from desensitization. Example traces are plotted in *SI Appendix*, Fig. S2, and analysis of the kinetics of 11 mutants is provided in *SI Appendix*, Table S2. Of all of the mutants tested, only insertion of AzF at position 798 had any appreciable effect on kinetics, slowing the rate of entry to desensitization to 50 ± 5 s^{-1} (n = 6 patches) (*SI Appendix*, Table S2) compared with 120 ± 10 s^{-1} for wild-type receptors (n = 36 patches, $P < 0.001$, t test). The deactivation rate was also slowed for this mutant (340 ± 50 s^{-1}, n = 2 patches, $P < 0.001$, t test against the wild type). For other mutants, the range of deactivation rates was from 1,200 to 2,200 s^{-1} compared with the average wild-type value of 1,600 ± 120 s^{-1} (n = 27), and the recovery from desensitization ranged from 45 to 70 s^{-1} compared with the average wild-type value of 55 ± 5 s^{-1} (n = 17) (*SI Appendix*, Fig. S2 and Table S2). Therefore, we assumed that these mutants (in their basal state; that is, before any UV exposure) have gating properties that are representative of GluA2 wild-type channels.

Patterns of UV-Induced Inhibition. Previously, we generated photoinactivatable AMPARs by inserting BzF in the extracellular domains of GluA2 (33). Due to their incorporation sites, these mutations were expected to trap an inactive state if they formed cross-links. Here, we chose sites on a pseudorandom basis without any particular expected photocross-linking effect. For five of the AzF mutants, the effect of UV illumination was a rapid, irreversible loss of the peak current response (Fig. 2 and *SI Appendix*, Table S3). Independent of the location (in any of the four membrane segments, M1–M4), we could inhibit the peak current by up to 95%. The fastest inhibitory action was observed for the F608AzF (M3) mutant, with a time constant of 1.5 s for cumulative exposures to UV (in intervals of 200 ms per episode) for reduction of the peak current to 4 ± 1% of its original value (barely distinguishable from background noise; n = 17) (Fig. 2*C* and *SI Appendix*, Table S3). We were able to control the speed of inactivation by changing the intensity of the UV light (50–100%) or the time interval of UV exposure per episode (50 and 200 ms) (*SI Appendix*, Fig. S3). We exposed receptors to UV light in resting and desensitized states by opening the shutter at the appropriate stages of each episode. To examine the active state, we initially blocked desensitization with cyclothiazide (CTZ) but found that CTZ itself could induce a UV-sensitive inhibition (*SI Appendix*, Fig. S4) that varied from batch to batch of CTZ. To avoid this problem, we instead performed experiments on the background of the L483Y mutation for all TAG mutants, with the exception of F608AzF-L483Y, which did not express. For this particular construct F608AzF, the UV-induced inhibition in the presence of CTZ was much faster than the CTZ-driven UV-dependent inhibition of GluA2 wild type (*SI Appendix*, Table S3). Surprisingly, the effects of UV exposure were independent of the functional state of the receptor. Values for all of the constructs tested that showed UV-dependent inhibition are listed in *SI Appendix*, Table S3. As previously reported (33), we controlled for nonspecific run-down of currents by pausing the UV exposures in the course of some experiments, observing that the peak current remained stable, and then, reverting to UV-driven inhibition.

Inhibition of responses might indicate nonspecific loss of channel function with UV exposure, but several observations

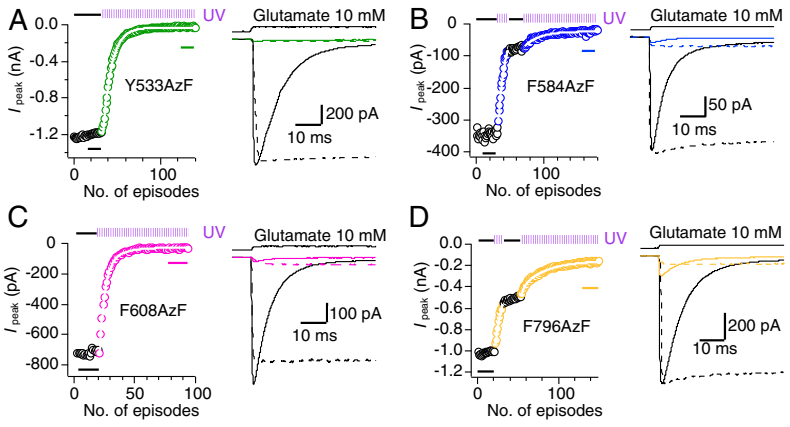

Fig. 2. UV-triggered inhibition of glutamate-induced currents. (*A*, *Left*, *B*, *Left*, *C*, *Left*, and *D*, *Left*) Examples of kymograms showing the time course of receptor inactivation for selected constructs. Each episode included a 400-ms application of 10 mM glutamate (each circle represents the peak current response). A 200-ms exposure of UV epiillumination was made in each episode (indicated in the kymogram by violet pulse trains and colored circles). The rate of peak current reduction was monoexponential (white outlined fits). (*A*, *Right*, *B*, *Right*, *C*, *Right*, and *D*, *Right*) Traces representing averages of 5–20 responses to glutamate before UV exposure (black trace) and after UV exposure (colors) in either the resting or desensitized state (solid lines; taken from points indicated by bars in kymograms) and fully active state (corresponding L483Y mutant; dotted line). We could not record currents from the GluA2-L483Y-F608AzF mutant (M3); therefore, CTZ was used to block desensitization for this construct. The dashed current traces were scaled to aid comparison (scale factor given in parentheses): Y533AzF-LY (0.8-fold), F584AzF-LY (0.9-fold), F608AzF + CTZ (5-fold), and F796AzF-LY (2.8-fold).

counter this proposition. As shown previously (33), GluA2 wild-type receptors were insensitive to UV light (*SI Appendix*, Fig. S5*A*) as were some mutants. For example, F531AzF (M1) was reliably rescued by AzF but showed no UV sensitivity at all (*SI Appendix*, Fig. S5*B*), speaking against nonspecific photodestructive effects based on AzF. Another control was provided by the F584TAG mutant in the absence of any UAA. All permissive AzF mutants had some degree of readthrough (that is, background rescue in the absence of UAA). The F584TAG mutation had the largest readthrough currents on average (*SI Appendix*, Table S4). However, unlike responses from receptors containing the AzF residue, the amplitude of responses obtained (in the absence of AzF) was entirely insensitive to UV illumination. We could not detect altered kinetic properties of receptors with TAG mutations expressed in the absence of UAA after UV exposure (*SI Appendix*, Table S5), but often, it was difficult to hold these patches long enough to obtain proper UV exposures, because they were unstable. The basal kinetic properties of TAG mutants were sometimes starkly different from those rescued with UAA [e.g., the F579TAG (M2) mutant has slow deactivation], further evidence that there is little readthrough in the presence of UAA. A typical recording from the F584TAG mutant from a cell cultured in the absence of AzF is shown in *SI Appendix*, Fig. S5*C*.

Although these controls gave us confidence that the inhibitory effects were site specific, the behavior of several other mutants provided more compelling evidence. For example, the F796AzF mutation in M4 was inhibited by UV, but inhibition was incomplete, reaching only about 85%. In addition, we found that incorporating AzF in M2 at position F579 also resulted in inhibition on UV illumination but only to 75% and with a concomitant increase in steady-state current (more details are given below and in *SI Appendix*, Table S3). This suggests that the effects of AzF activation within the TMD are site specific.

Photopotentiation. As would be expected from an unbiased screen of the gating region, in addition to inhibition, we also found four mutants that had a strong potentiating effect on function. For F515BzF, the peak current was on average increased 1.6-fold, with a larger 2.5-fold increase in the relative steady-state current compared with the peak current size (Fig. 3 and *SI Appendix*, Table S3). Peak current was also increased for the nondesensitizing LY mutant, indicating an effect on gating, not a simple block of desensitization (3). Glutamate-activated peak and steady-state currents were similarly increased for L518BzF by 1.3- and 7.8-fold, respectively (Fig. 3). As expected from a stabilization of the open state, paired measurements in the same patch (before and after UV exposure) showed that the rate of entry to desensitization was slowed (from 140 ± 10 to 90 ± 10 s^{-1}, $n = 19$ and from 130 ± 10 to 90 ± 10 s^{-1}, $n = 7$ for F515BzF and L518BzF, respectively). Analyses including both paired and nonpaired data are in *SI Appendix*, Table S2.

A similar effect on receptor activation behavior was seen for AzF introduced in M4 at position Y797, with an increase in the steady-state current (3.7-fold), presumably corresponding to the block of desensitization (from 120 ± 5 to 70 ± 5 s^{-1}, $n = 24$) (Fig. 3). Similarly, the relative steady-state current increased, albeit more variably, after UV exposure when AzF was incorporated into the neighboring M4 position at I798 (fold increase of 7 ± 3) (Fig. 3 and *SI Appendix*, Table S3). The extent of photopotentiation of the steady-state currents did not correlate with the initial size of the relative steady-state currents before the application of UV light (R^2 range from 0.06 to 0.2) (*SI Appendix*, Fig. S6). Notably, desensitization was slowed by incorporating AzF at position I798 and did not change with exposure to UV light (from 50 ± 5 to 45 ± 10 s^{-1}, $n = 6$) (Fig. 3). Since the I798AzF (M4) construct showed pronounced rundown, we were unable to determine deactivation rates and recovery rates from desensitization before and after applying UV light.

The Interaction between the Pre-M1 and M4 Helices. The confluence of the functional results in terms of potentiation of constructs with BzF in Pre-M1 (F515BzF, L518BzF) and AzF in M4 (Y797AzF, I798AzF), regions that are in close structural proximity, led us to ask what structural dynamics could produce these effects. Inserting the mutated residues into the closed-state structure of GluA2 provides a striking hypothesis: reciprocal cross-linking between these two sites is physically plausible (Fig. 4*A*). The BzF substitution at position 515 is located on the outer

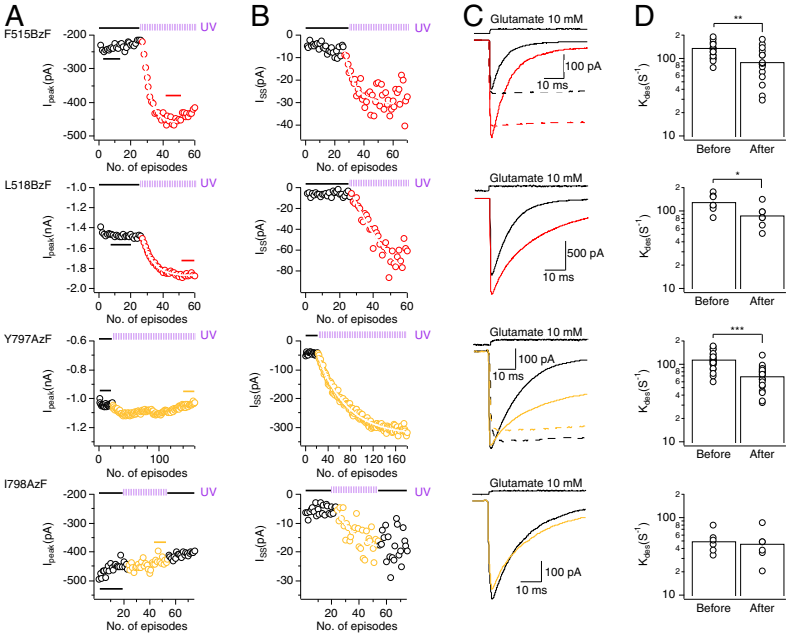

Fig. 3. UV-triggered potentiation of AMPAR responses. (*A* and *B*) Example kymograms illustrating the time course of the potentiation of peak (*A*) and steady-state (*B*) current for GluA2-F515BzF (Pre-M1; row 1), GluA2-L518BzF (Pre-M1; row 2), GluA2-Y797AzF (M4; row 3), and GluA2-I798AzF (M4; row 4). The rate of peak current potentiation was monoexponential (white outlined fits). (*C*) Example current traces representing averages of 5–20 responses to glutamate before UV exposure (black traces) and after UV exposure (colors) in either the resting or desensitized state (solid lines; taken from points indicated by bars in kymograms). Representative currents from the corresponding L483Y mutants (active-state UV exposure; dotted lines) are shown for F515BzF and Y797AzF (scaled, as in Fig. 2, by 0.35- and 3.5-fold, respectively). (*D*) Bar graphs summarize desensitization rates in 10 mM glutamate of GluA2-F515BzF, -L518BzF, -Y797AzF, and -I798AzF before and after UV exposures (*SI Appendix*, Table S2 has a summary of rates). *$P < 0.05$, **$P < 0.01$, and ***$P < 0.001$.

face of the Pre-M1 helix, but a rotation or outward bloom of this "collar" (1) could allow the photoactivated BzF radical to contact the M4 helix. Likewise, the AzF at 797 is likely buried within the membrane, but conformational change could allow it to reach multiple cross-linking partners. Rotations of M4 could permit cross-linking onto M3 or M1 of the neighboring subunit, but approach of the Pre-M1 helix from the same subunit, as envisaged above, could also bring this residue into potential contact.

Intersubunit cross-links, like those previously seen for the S729BzF mutant (33), were negligible for GluA2 wild-type receptors and all mutants that we tested (*SI Appendix*, Table S1). To test our hypothesis of reciprocal cross-linking between Pre-M1 and M4 within subunits, we used a principle based on a previously published study (41) as illustrated in Fig. 4*B*. Using antibodies to label both N and C termini, we used quantitative Western blotting to determine the protection against protease digestion afforded by cross-linking. We expected to detect intrasubunit cross-linking if the UV-activated UAA was able to physically connect fragments divided by an inline tobacco-etch virus (TEV) cleavage site. After brief UV exposures of 2 and 5 min, the F515BzF (Pre-M1) mutant harboring a TEV cleavage site showed a small but reproducible increase in the protected monomer fraction (Fig. 4 *C* and *D*). Based on the location of F515 in structures of GluA2 and our failure to detect any increase in dimers or higher-order oligomers, this result indicates cross-linking to M4 of the same subunit. The Y797AzF and I798AzF mutants did not show detectable monomer protection (Fig. 4 *C* and *D*), indicating that the effects in electrophysiological experiments likely arise either from a ring expansion of the phenyl ring or from cross-linking to lipid. Both interpretations require that M4 moves during gating and desensitization to feel the restraint or steric hindrance from the photoproduct (*Discussion*). These exposures to UV light were about 100-fold less intense than those experienced by receptors during patch-clamp experiments and epiillumination by UV (33). Therefore, the total exposure over a few minutes should be equivalent to those in electrophysiology experiments (seconds of exposure to epiillumination). However, we avoided longer exposures of, for example, 15–30 min in the UV oven, because these exceed the exposures needed for the relatively rapid changes in the gating properties that we detected in electrophysiological experiments. It seems likely that the low fraction of rescued monomer is due to heterogeneity of cross-linking to multiple targets. This raises the possibility that the substantial gating effect at the F515BzF site could derive from only one or two cross-linking events to M4 per receptor.

Structural Mapping of Photoactive Sites. The effects of UV exposure on the peak, relative, and absolute steady-state currents of rescued receptors are summarized as bar plots in Fig. 5. We mapped these effects onto a structure of the GluA2 TMD [Protein Data Bank (PDB) ID code 3KG2; ref. 42] (Fig. 5*B*). These plots suggested gradients in the peak and steady-state current effects, but any correlations are weak ($R^2 = 0.3$ for the fold change in peak current against radial distance) (*SI Appendix*, Fig. S7). The weakness of these relations is not surprising given that the chemistry of individual side-chain environments as well as local motions must influence the effect of a given residue on channel gating motions.

Structures of GluA2 in resting, active, and desensitized states are now available, and therefore, we next asked if the displacement of residues between structures could be related to the photoactivated effects on currents. We selected two nominally resting structures bound with antagonists (5L1B and 5VHZ), two active-state structures with open pores (5VOT and 5WEO), and two desensitized-state structures (5VOV and 5WEK). Measurements of distances between residues in different states produced a complex picture indicating considerable structural plasticity both within and between functional states (*SI Appendix*, Fig. S8). The two open-state structures are quite similar to each other and distinct from the closed-state

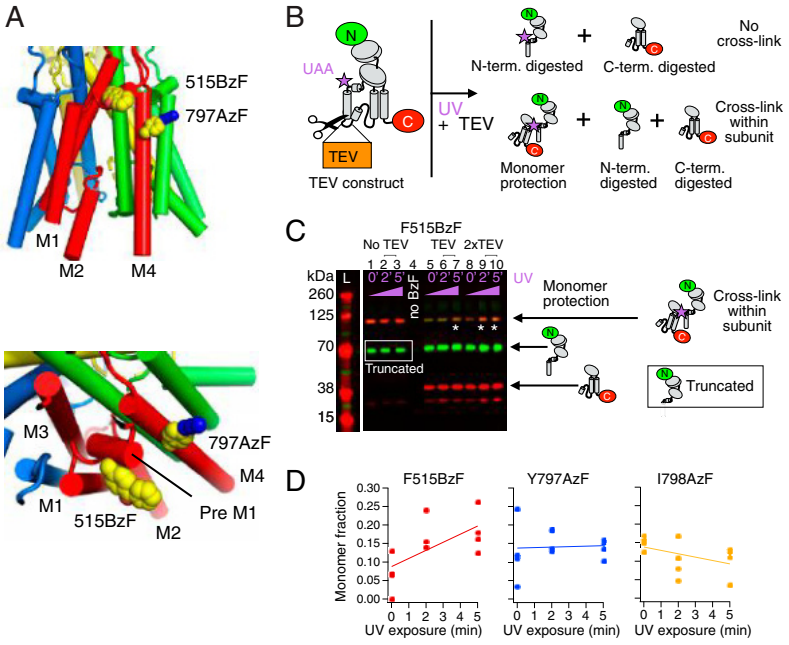

Fig. 4. Intrasubunit cross-linking by BzF. (*A*) Structure of the TMD (PDB ID code 3kg2) with AzF and BzF incorporated at sites 797 and 515, respectively, illustrating the close proximity of the two sites. (*B*) Cartoon of the TEV site construct and fragments generated by TEV protease treatment. A site for TEV protease recognition was introduced in the M1–M2 intracellular loop of the GluA2 subunit as well as a C-terminal FLAG-tag epitope and a TAG mutation for incorporation of UAA (violet star). Covalent bridging within a subunit of the two fragments arising from TEV protease treatment should "protect" a monomeric subunit band on Western blots. (*C*) Exemplary Western blot showing monomer protection of F515BzF (Pre-M1). For all conditions, the band at 63 kDa corresponds to GluA2 truncated at residue 515. The truncated band is undistinguishable from the digested N terminus when TEV protease is added (64 kDa). (Lanes 1–3) Quantitation of the rescue of F515TAG construct in cells by BzF showed a monomeric band at 100 kDa. A band from subunits truncated at the TAG site (63 kDa) is present, presumably pulled down in FLAG purification with full-length subunits. (Lane 4) The omission of only the UAA results in no rescue of monomeric band. A band corresponding to subunits truncated at the TAG site can be visualized on the blot; however, the band is very faint, presumably due to a lack of any FLAG epitope. (Lanes 5–7) Quantitation of F515BzF (Pre-M1) treated with TEV protease showed an increase of monomer fraction with longer exposure to UV. (Lanes 8–10) Exposing F515BzF to twice the amount of TEV protease (relative to lanes 5 and 6) led to an increase in protection of monomers, indicating more cross-linking events. (*D*) Summary of the monomeric fraction plotted against the UV exposure time. Only insertion of BzF in position 515 showed an increase in monomer protection over time.

structures, but the variability within the set of closed-state structures was high (*SI Appendix*, Fig. S8*C*). This structural variability accounts for almost all of the variability found in C-α positions between "closed" and "open." Notably, the most variable regions are the selectivity filter and the top of the M4 helix.

Finding no clear relation between geometry and the functional effect, we produced a two-dimensional plot of gating changes after UV exposure (Fig. 6*A*), plotting the peak current change against the relative steady-state current change. The plot delineates a cluster of null mutants, and two clear groups for which functional changes emerged, whereas the F579AzF (M2) mutant was a striking outlier. In the first of the two groups, peak current was inhibited, and the steady-state current concomitantly increased (Fig. 6*A*, purple circles). In the second group, a robust increase in steady-state current was accompanied with either increase or no change in the peak current (Fig. 6*A*, green circles). Notably, F579AzF could be described as an outlier in plots of peak current and steady-state current against geometry (*SI Appendix*, Fig. S7).

Simulations based on a simple single-binding site model of AMPARs (5, 43) can mimic the behavior of these two groups (Fig. 6 *B–D*). The behavior of the first group of mutants on the relation between the effects on peak and steady-state currents was reproduced by progressively reducing the lifetime of the desensitized-state AD2 or by allowing the desensitized state to become weakly conductive (Fig. 6 *B–D*). The kinetic behavior of the second group of mutants was reproduced by altering the channel-shutting rate α or the opening rate β (Fig. 6 *B–D*). The quantitative agreement between the 5-fold increase in the steady-state current accompanied by a 50-fold reduction in the peak current predicted by this model and the effects on actual mutants (e.g., 608AzF in M3) is notable. Rate constants for the model are the same as in our previous paper—no optimization was done (*Materials and Methods*). Most importantly, these simulations indicated that cross-linking at the F579 position is complex in nature and must involve multiple effects on kinetic model parameters, where both the lifetime of desensitization and channel-opening rate change (Fig. 6 *B–D* and *SI Appendix*, *Supplementary Materials and Methods*). Another manipulation allowing the desensitized state to become progressively weakly conductive gave the best description (Fig. 6 *B–D*).

Fig. 6*E* and Movie S1 illustrate four classes of residues that we could segregate by analogy to kinetic models of AMPAR activation. The residues form contiguous clusters in the TMD, suggesting that at least two of them correspond to functional modules that execute distinct gating functions—a bundle crossing gate and a desensitization module between helix M4 and the Pre-M1 collar. Another contiguous set of "null" mutants seems peripheral and at most, weakly involved in gating. Future work will address the extent to which these "modules" are independent or coupled within a common pathway. In the following section, we investigated the properties of the outlying F579 mutant.

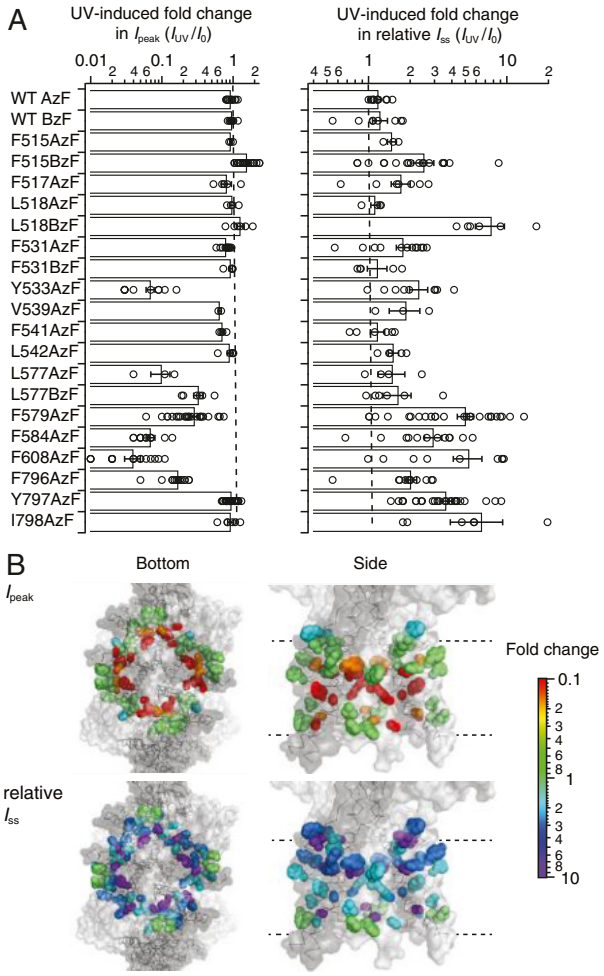

Fig. 5. Segregation of sites by UV effect. (*A*) Bar graph (*Left*) representing the summary of the change in peak current before (I_0) and after UV (I_{UV}) of selected GluA2 constructs with AzF or BzF incorporated in the TMD. Small reductions in peak current (like for F517AzF-preM1) are likely due to rundown and are not related to the application of UV. Bar graph (*Right*) summarizing the fold change in steady-state current relative to the peak current. (*B*) Bottom and side views of structures showing AzF and BzF insertion sites as spheres colored according to their UV-dependent changes in peak current amplitude (*Upper*) and relative steady-state current (*Lower*). Each site is highlighted in color in all four subunits. The color scale (*Left*) is representing the colors used to show the fold change measured for each construct. At sites where two residues were tested, we plotted the greater fold change.

A Complex Role in Receptor Kinetics for the F579 Site. A complicated kinetic model was needed to mimic the position of F579AzF (M2) in the plot of the relation between peak and steady-state currents (Fig. 6). Therefore, we reasoned that complex UV-driven changes in gating at this site might be detectable in patch-clamp recordings. To address this point, we pursued a more detailed investigation of kinetics, including recovery from desensitization, at both an intermediate time point in cumulative UV exposure (~2 s) and after saturating exposure (8 s).

Kymograms of the UV effect on peak current are shown in Fig. 7*A*. As in our initial analysis, peak current inhibition by UV was incomplete, reaching only about 75% (Fig. 7*A* and *SI Appendix*, Table S3). The steady-state current increased (*SI Appendix*, Fig. S9). This was also true for the nondesensitizing L483Y variant, indicating that hindrance of the channel-opening reaction rather than increased desensitization was responsible for this inhibition of the peak. In these experiments, the rate of entry to desensitization was reduced by almost one-third after saturating UV exposure time of 8 s (from $k_{des} = 130 \pm 15\ s^{-1}$ to $k_{des} = 45 \pm 10\ s^{-1}$, $n = 9$) (*SI Appendix*, Fig. S9), whereas intermediate cumulative exposure time of ~2 s showed desensitization rates similar to desensitization rate before UV application ($k_{des} = 110 \pm 10\ s^{-1}$). In contrast, steady-state currents activated by 10 mM glutamate increased to about 10% of the peak (*SI Appendix*, Fig. S9). Likewise, the deactivation rate after a 1-ms pulse of 10 mM glutamate was also substantially slowed [from 1,410 ± 140 to 700 ± 140 s^{-1} (2-s UV) and 500 ± 140 s^{-1} (8-s UV), $n = 9$] (*SI Appendix*,

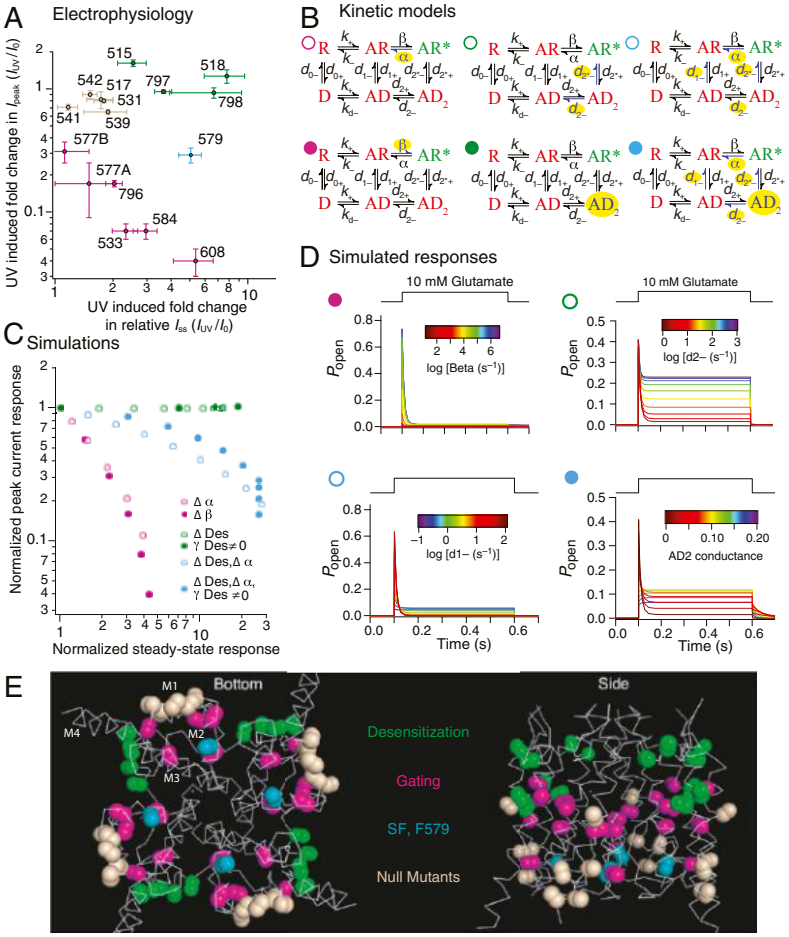

Fig. 6. Segregation based on gating properties. (*A*) Plot shows the relation between the mean UV-induced changes in peak and relative steady-state current before (I_0) and after UV (I_{UV}) at each site. Sites are color coded according to the effect: null in wheat, potentiation in green, inhibition in purple, and intermediate (579) in cyan. The same color code applies throughout the figure; 577A and 577B denote the insertions of AzF and BzF, respectively, at this particular site. (*B*) Simplified single-binding site models of AMPAR gating. Open state (AR*) is green, and shut states (including desensitized states D, AD, and AD_2) are red. Rates or states that were varied in each simulation are highlighted in yellow (*SI Appendix, Supplementary Materials and Methods* has details). (*C*) A two-dimensional plot resembling that in *A* but derived from simulations of the kinetic models described in *B*. Progressive alteration of the channel-shutting and -opening rates (α and β, respectively; purple circles), changes in desensitization rates (d2; open green circles), or AD2 becoming conductive (filled green circles). Changes to both gating and desensitization are needed to obtain the intermediate behavior (cyan circles). (*D*) Simulated responses from kinetic models (indicated with colored circles as in *B*) used to construct *C*, with traces colored according to the rate constant indicated. (*E*) Gating modules in the AMPAR pore (Movie S1). The major classes of mutants form contiguous modules: a desensitization module (green; collar), a gating module (magenta; bundle crossing gate), and peripheral mutations with no effect (null mutants; wheat). The selectivity filter mutant with complex behavior is F579AzF (cyan).

Fig. S9). Both of these effects on gating developed strongly at early stages of UV exposure (that is, after only 2 s).

We expected from our kinetic modeling that the stability of the desensitized state should be increased and possibly, that the desensitized state might become conductive. To this end, recovery from desensitization also was slowed [from k_{rec} = 40 ± 5 s^{-1} to k_{rec} = 20 ± 5 s^{-1} (2-s UV) and k_{rec} = 15 ± 5 s^{-1} (8-s UV), n = 9] (Fig. 7 *B* and *C*). One caveat for this measurement is that control measurements on the GluA2 wild-type receptor expressed on the background of AzF and its cognate synthetase showed a small slowing of recovery after UV exposure (from 55 ± 4 to 38 ± 2 s^{-1}, P = 0.008, paired t test, n = 9 patches) (*SI Appendix*, Table S2). The effect on F579AzF (M2) mutants was much more substantial and quite different to control measurements, with a "quiescent phase" where no effective response was detected for about 30 ms after the conditioning pulse (Fig. 7*B*). Measuring recovery was hampered by the peak current inhibition but also, by the development of an unusual long decay in the current after the desensitizing pulse. This "off relaxation" after desensitization was much slower after only a brief UV exposure [from k_{off} = 150 ± 60 s^{-1} to k_{off} = 30 ± 5 s^{-1} (2-s UV) and k_{off} = 35 ± 5 s^{-1} (8-s UV), n = 9] (Fig. 7*D*). These measurements also revealed that the steady-state current increased in absolute magnitude. There was no concomitant effect on the resting-state conductance—the patches did not become leaky. Overall, after photoactivation, the F579AzF mutant has anomalous desensitization behavior, with both slower recovery and more activity during recovery.

By comparing effects on kinetics at intermediate and saturating UV exposures, it was clear that the onset of UV-driven effects in F579AzF was not coherent. The slowing effect on the tail current (k_{off}) and deactivation as well as the slowing of recovery from desensitization were pronounced already at 2 s, whereas effects on the steady-state current and the rate of entry to desensitization developed later (Fig. 8*A*). These distinct time courses are further evidence that photoactivation of the F579AzF mutant has an unprecedent effect on multiple functional states of the AMPAR. This observation is consistent with a set of structurally distinct states at the selectivity filter region (at the cytoplasmic end of the channel) (Fig. 8 *B* and *C*), which are distinctly affected as the photoactivation dose increases on a per-subunit basis. Heterogeneous photoproducts generated by AzF may also have facilitated detection of these different effects.

Discussion

Despite the recent release of structures of activated GluA2 receptors (1, 2) to compare with cognate closed-state structures (42, 44, 45), the nature of conformational changes occurring at the level of the TMD of AMPARs during gating remains unclear. Previous work supports the idea that M3 lines the pore and an upper hydrophobic box (46, 47) and that M2 comprises the selectivity filter region (48). Conversely, the roles of the M1 and M4 helices are less well studied. In this work, site-specific incorporation of photoactivatable cross-linkers (33) enabled access to the entire TMD of homomeric GluA2 AMPARs. A key ad-

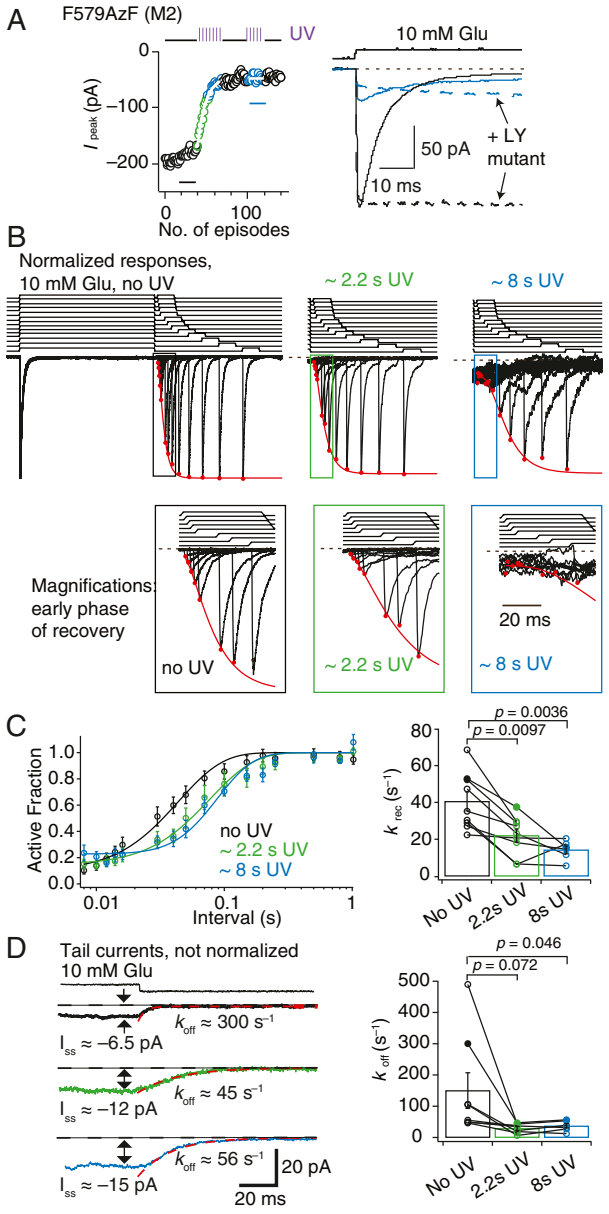

Fig. 7. Broad role of the M2 segment in activation and desensitization. (*A*) Kymograms illustrating the time course of incomplete inhibition for F579AzF (M2) peak current responses to 10 mM glutamate (*Left*). Example current traces (*Right*) representing averages of 10 responses to glutamate before UV exposure (black trace) and after UV exposure (cyan) in desensitized state (solid lines) and fully active state (corresponding L483Y mutant; dotted line; scaled 1.4-fold larger to aid comparison). (*B*) Exemplary normalized traces for recovery from desensitization before, during (2.2 s; green), and after (8 s; blue) UV exposure. Time courses of glutamate applications are shown above the traces. Red circles indicate the peak of the response fitted with a recovery function (red line). Apparent increase in noise after 8 s of UV exposure appears from performing a zoom on the trace to be able to find the remaining glutamate-induced current. (*C*) Recovery curves from pooled data are shifted to the right with cumulative UV exposure. Bar graph summarizing paired recovery from desensitization protocols before, during, and after 8 s of UV exposure. Solid symbols refer to the patch in *A*. Recovery rates ± SEM: k_{rec} = 40 ± 5 s^{-1} (n = 9), k_{rec} = 20 ± 3 s^{-1} (n = 9), and k_{rec} = 15 ± 2 s^{-1} (n = 6) before, during, and after UV, respectively. (*D*) Exemplary traces for tail currents after desensitization. Bar graph of decays after the steady-state current before, during, and after UV exposures, with solid symbols referring to the traces shown in *Left*. Deactivation rates ± SEM are k_{off} = 150 ± 60 s^{-1} (n = 9), k_{off} = 30 ± 5 s^{-1} (n = 9), and k_{off} = 35 ± 10 s^{-1} (n = 6) before, during, and after UV, respectively. Error bars represent SEM.

vantage of this method is that photoactivation is precisely controlled in time, allowing function to be assessed both after saturating exposures and during progressively increasing subsaturating exposures (as in Fig. 7). Critically, we expected that cross-linking potential would not require solvent exposure, allowing us to build a relatively unbiased map of functional elements in the TMD (possible sources of bias were discussed above). We could cover previously inaccessible sites and relate these elements to structural data. This factor was decisive in revealing relationships between the Pre-M1 and M4 helices and the selectivity filter region and channel activation and desensitization.

The incorporation of bulky AzF and BzF residues had at most minor effects on the kinetics of channel activation, gating, or desensitization of GluA2 before exposure to UV. The facility of these UAAs to be incorporated into the TMD depended on their environment and chemistry (Fig. 1). Unsurprisingly, sites proximal to the phospholipid membrane (at the TMD periphery) were more likely to provide enough space for the insertion of both AzF and BzF, whereas the ion channel core was less permissive. However, the periphery was not insensitive to insertion of AzF and BzF, and I798AzF in M4 had, in contrast to other sites, basal kinetics (that is, before UV exposure) that differed from GluA2 wild type. After UV exposure, long-lived (>25-ms) single-channel bursts could be observed for the I798AzF mutant (*SI Appendix*, Fig. S10). These findings augment previous studies showing that insertion of tryptophan in sites of the peripheral TMD can disrupt transmembrane interactions and receptor tetramerization (40, 49). At sites that were permissive, we found that ∼50% of the AMPARs rescued by incorporation of AzF showed a change in channel gating on UV exposure, while incorporation of BzF only showed an UV-induced effect in 3 cases of 11 (Fig. 1), 2 of which were at the membrane periphery. This superior capability of AzF in the TMD might be due to its greater mobility to rotate and cross-link to nearby carbohydrogen relative to BzF (35). Overall, UV-induced control of receptor activity was independent of the functional state and which membrane helix harbored the AzF residue. Surprisingly, segments lining the pore and peripheral elements (for example, M4) could alter gating and desensitization equally well. These observations suggest that gating is not a simple movement of the M3 segment to open the bundle crossing. Rather, it is plausible that most if not all of the membrane segments rearrange on receptor activation or to permit desensitization. Altered protein rigidity or friction might also explain the energetic changes. The wide range of potential interacting partners for AzF or BzF in each state of activation may have precluded state dependency. Heterogeneity of cross-linking targets is far from trivial to resolve. It is conceivable that UV illumination in different states results in cross-linking to various membrane segments or lipid parts of the bilayer to yield the same effects. Despite these reservations, we could identify clear site-specific actions of UAAs that extend our understanding of AMPAR activation and desensitization.

Previous work suggested that a disulfide bond between the Pre-M1 and M4 helices could inhibit channel opening (8). Four mutants clustered at the collar region (F515, L518, Y797, and I798) had similar UV-dependent effects, unique to this gating module (Figs. 6*E* and 8*D*). Our functional and biochemical data indicate that an adventitious cross-link or interactions between Pre-M1 and M4 can also have a potentiation effect and block desensitization (Fig. 3). When BzF was incorporated in the likely solvent-exposed sites in the Pre-M1 helix (F515BzF and L518BzF),

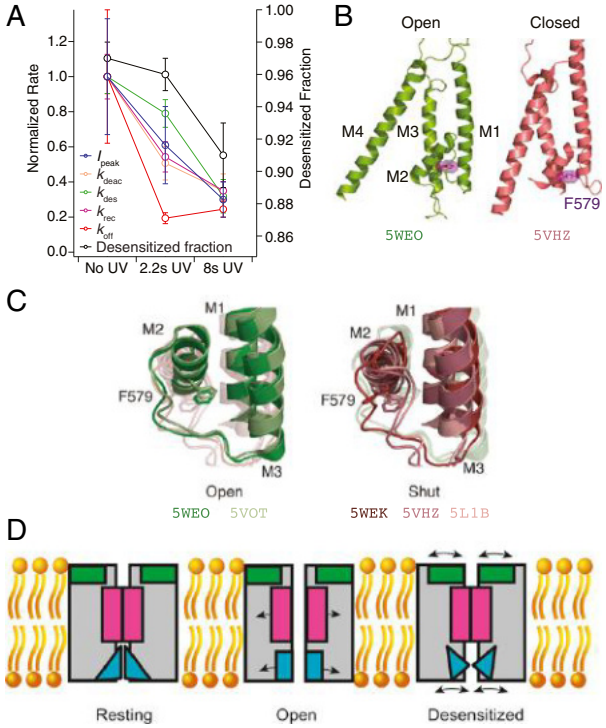

Fig. 8. Putative AMPAR gating modules. (*A*) The time courses of UV-dependent gating changes in the F579AzF (M2) mutant (details are in Fig. 7 and *SI Appendix*, Fig. S9). Desensitization changes (desensitized fraction and k_{des}) developed over longer cumulative exposures than deactivation (k_{deac}) or the long decay after a desensitized pulse (k_{off}). For the inhibition of the peak current (I_{peak}) before, during (2.2 s), and after (8 s) UV exposure: $P = 0.34$ (paired t test between no UV and 2.2-s UV) and $P = 0.0095$ (repeated measures ANOVA). (*B*) The F579 site is located immediately behind the selectivity filter. Overlay of the TMD of a single subunit from closed (red) and open (green) GluA2 channels with the four transmembrane helices (M1–M4) indicated. (*C*) Overlays of open and closed channel structures showing F579 in multiple conformations. The PDB ID codes are indicated in the corresponding colors. (*D*) Scheme of gating modules. Channel opening requires a "bloom" at the M3 segment (gating module; magenta) and a conductive selectivity filter (cyan). Desensitization is accompanied by movements of the desensitization module (green) and potentially by structural dynamics of the selectivity filter.

BzF cross-linking potentiated receptor currents (Fig. 3). Biochemical analysis showed no intersubunit cross-links, but we found a robust UV-induced increase in intrasubunit cross-linking by quantifying monomeric protection of GluA2-F515BzF subunits cleaved by TEV protease. This result indicates a rotation of the Pre-M1 segment toward M4 of the same subunit (Fig. 4*D*). This type of interaction has also been speculated for NMDARs (50, 51). Furthermore, while NMDAR M4 segments have subunit-specific effects on gating and permeation (52), it has been shown that the extreme intracellular end of AMPAR M4 segments only contributes weakly to desensitization (50). Desensitization after photoactivation of Y797AzF (M4) was strongly reduced. Comparing this with our recent Förster resonance energy transfer data suggesting that the M4 (as assayed from the C-terminal movement) is likely to move during gating, desensitization, and without pore opening (53), a wider role for peripheral interactions to modulate AMPAR function seems likely. We did not detect cross-linking either within or between subunits for Y797AzF. The effect in desensitization might thus be explained either by ring expansion of the AzF having a steric effect or by cross-linking to a lipid. We recently showed that interaction between the LBD-M4 linker and Stargazin is sufficient for modulation of GluA2 (54), thus raising the prospect that the perturbation at this site in M4 (Y797AzF), pointing away from the core of the channel, could be related to the changes in receptor function effected by auxiliary proteins, which in fact, interact with the M4 and M1 of the AMPAR (1, 55). Notably, in some patches, we could detect that, after photoactivation of AzF at position 798, glutamate could activate long bursts of channel openings with high open probability (*SI Appendix*, Fig. S10), much like the incorporation of Stargazin produces (56).

A distinct group of mutants flanking the bundle crossing (Figs. 6*E* and 8*D*) showed properties likely resulting from an inhibition of the channel-opening reaction either by slowing channel opening or by destabilization of the open state. F608 in the M3 helix showed the most potent inhibition. A kink at A618 allows the upper segment of M3 to move substantially on channel opening (1), but F608 seems to move much less (*SI Appendix*, Fig. S8). The fast rate of UV inhibition at this site might, therefore, simply reflect the necessity of M3 movement to open/close the channel.

Both the structural and functional analyses of cross-linking sites indicated that F579AzF (M2), located in close proximity to the selectivity filter at the base of the M2 helix, has a special role in gating of the receptor. In this context, the variation of the selectivity filter structure (and likewise, its disordered nature in some other structures), including between closed-state structures, and steric hindrance of the open channel selectivity filter structure by F579 are of interest (Fig. 8*C*). One caveat is the comparative lack of detail in this region for currently available structures; additional work will hopefully provide more information. Inhibition of the peak current was in the case of F579AzF accompanied by a large increase in the steady-state current. Mimicking these changes in a kinetic model required concurrent destabilization of both the open state and the desensitized state. The idea that desensitization can be affected by a residue deep in the channel in the M2 helix was confirmed by the slowing of recovery from desensitization measured after UV exposure of F579AzF (Fig. 7). Notably, recovery happens entirely while the channel is closed. Therefore, cross-linking at this site had a dual effect on desensitization, slowing both entry and recovery (2.9-fold each), as well as separately biasing the open–closed equilibrium (because the peak current was substantially inhibited). Finally, we note that comparing our results with structures directly was generally unproductive (*SI Appendix*, Fig. S8), whereas we readily discerned functional groups of residues by analyzing a two-dimensional plot of electrophysiological properties (Fig. 6). This relation between peak vs. steady-state responses presumably gives insight, because it compares the energies of modifying channel-opening transitions and modifying receptor desensitization.

Overall, the effects of the F579AzF mutation in M2 after UV exposure are complex, and the extent of changes to the current has distinct dependencies on UV exposure. Our results do not distinguish between subunit dosage effects that develop with a different dependence on the number of reacted subunits or trapping of distinct structural forms. More work will be needed to dissect how the different UV-dependent changes occur. The model that gave the best description of the F579AzF data included progressive shift of the desensitized state toward a small conductance. In practice, such a phenomenon (the development of a new conductive state with UV exposure) may not be related to desensitization, but the relaxation from the steady-state current (from the tail current kinetics) (Fig. 7*C*) matched that of recovery from desensitization. However, our observations strongly corroborate the idea that the selectivity filter of AMPARs is as dynamic a structure as it is in simple tetrameric channels, with distinct arrangements between states (1). This property might allow the selectivity filter region to function as a second ion gate,

closing and opening the pore between certain functional states as in other tetrameric channels. Additional work will be required to assess whether state-dependent ion transit through the selectivity filter is a feature of the AMPAR TMD.

Materials and Methods

The aminoacyl-tRNA-synthetase and tRNA constructs for human embryonic kidney cell expression (28, 29) were gifts from Thomas Sakmar, The Rockefeller University, New York, NY. Molecular biology, cell culture, and patch-clamp electrophysiology were done as described (33). Kinetic modeling was done with the Aligator scripts (https://www.github.com/aplested). For biochemical experiments, we used a construct with a TEV protease site between M1 and M2. Full methods and details of data analysis are in *SI Appendix, Supplementary Materials and Methods*.

ACKNOWLEDGMENTS. This work was funded by Deutsche Forschungsgemeinschaft Grants Cluster of Excellence "NeuroCure" (EXC-2049; to A. J. R. Plested), DFG PL619-2 (to A. J. R. Plested), and SFB/TRR 186 (to A. J. R. Plested). M.H.P. was the recipient of fellowships from the Carlsberg Foundation and the Danish Council for Independent Research. A. Poshtiban and V.K. both received stipends from NeuroCure.

1. E. C. Twomey, M. V. Yelshanskaya, R. A. Grassucci, J. Frank, A. I. Sobolevsky, Channel opening and gating mechanism in AMPA-subtype glutamate receptors. *Nature* **549**, 60–65 (2017).
2. S. Chen *et al*., Activation and desensitization mechanism of AMPA receptor-TARP complex by cryo-EM. *Cell* **170**, 1234–1246.e14 (2017).
3. Y. Sun *et al*., Mechanism of glutamate receptor desensitization. *Nature* **417**, 245–253 (2002).
4. M. S. Horning, M. L. Mayer, Regulation of AMPA receptor gating by ligand binding core dimers. *Neuron* **41**, 379–388 (2004).
5. A. L. Carbone, A. J. R. Plested, Coupled control of desensitization and gating by the ligand binding domain of glutamate receptors. *Neuron* **74**, 845–857 (2012).
6. M. V. Yelshanskaya, K. Saotome, A. K. Singh, A. I. Sobolevsky, Probing intersubunit interfaces in AMPA-subtype ionotropic glutamate receptors. *Sci. Rep.* **6**, 19082 (2016).
7. B. Herguedas *et al*., Structure and organization of heteromeric AMPA-type glutamate receptors. *Science* **352**, aad3873 (2016).
8. M. V. Yelshanskaya, S. Mesbahi-Vasey, M. G. Kurnikova, A. I. Sobolevsky, Role of the ion channel extracellular collar in AMPA receptor gating. *Sci. Rep.* **7**, 1050 (2017).
9. S. M. Schmid, C. Körber, S. Herrmann, M. Werner, M. Hollmann, A domain linking the AMPA receptor agonist binding site to the ion pore controls gating and causes lurcher properties when mutated. *J. Neurosci.* **27**, 12230–12241 (2007).
10. R. M. Klein, J. R. Howe, Effects of the lurcher mutation on GluR1 desensitization and activation kinetics. *J. Neurosci.* **24**, 4941–4951 (2004).
11. D. del Camino, G. Yellen, Tight steric closure at the intracellular activation gate of a voltage-gated K(+) channel. *Neuron* **32**, 649–656 (2001).
12. K. Oelstrom, M. P. Goldschen-Ohm, M. Holmgren, B. Chanda, Evolutionarily conserved intracellular gate of voltage-dependent sodium channels. *Nat. Commun.* **5**, 3420 (2014).
13. J. E. Contreras, D. Srikumar, M. Holmgren, Gating at the selectivity filter in cyclic nucleotide-gated channels. *Proc. Natl. Acad. Sci. U.S.A.* **105**, 3310–3314 (2008).
14. Y. Zhou, X. M. Xia, C. J. Lingle, Cysteine scanning and modification reveal major differences between BK channels and Kv channels in the inner pore region. *Proc. Natl. Acad. Sci. U.S.A.* **108**, 12161–12166 (2011).
15. D. J. Posson, J. G. McCoy, C. M. Nimigean, The voltage-dependent gate in MthK potassium channels is located at the selectivity filter. *Nat. Struct. Mol. Biol.* **20**, 159–166 (2013).
16. J. Thompson, T. Begenisich, Selectivity filter gating in large-conductance Ca(2+)-activated K+ channels. *J. Gen. Physiol.* **139**, 235–244 (2012).
17. R. Blunck, J. F. Cordero-Morales, L. G. Cuello, E. Perozo, F. Bezanilla, Detection of the opening of the bundle crossing in KcsA with fluorescence lifetime spectroscopy reveals the existence of two gates for ion conduction. *J. Gen. Physiol.* **128**, 569–581 (2006).
18. A. J. Labro, D. M. Cortes, C. Tilegenova, L. G. Cuello, Inverted allosteric coupling between activation and inactivation gates in K^+ channels. *Proc. Natl. Acad. Sci. U.S.A.* **115**, 5426–5431 (2018).
19. C. Tilegenova, D. M. Cortes, L. G. Cuello, Hysteresis of KcsA potassium channel's activation- deactivation gating is caused by structural changes at the channel's selectivity filter. *Proc. Natl. Acad. Sci. U.S.A.* **114**, 3234–3239 (2017).
20. P. K. Devaraneni *et al*., Semisynthetic K+ channels show that the constricted conformation of the selectivity filter is not the C-type inactivated state. *Proc. Natl. Acad. Sci. U.S.A.* **110**, 15698–15703 (2013).
21. A. I. Sobolevsky, M. V. Yelshansky, L. P. Wollmuth, The outer pore of the glutamate receptor channel has 2-fold rotational symmetry. *Neuron* **41**, 367–378 (2004).
22. A. I. Sobolevsky, C. Beck, L. P. Wollmuth, Molecular rearrangements of the extracellular vestibule in NMDAR channels during gating. *Neuron* **33**, 75–85 (2002).
23. A. H. Ahmed, S. Wang, H.-H. Chuang, R. E. Oswald, Mechanism of AMPA receptor activation by partial agonists: Disulfide trapping of closed lobe conformations. *J. Biol. Chem.* **286**, 35257–35266 (2011).
24. A. Y. Lau *et al*., A conformational intermediate in glutamate receptor activation. *Neuron* **79**, 492–503 (2013).
25. J. Baranovic *et al*., Dynamics of the ligand binding domain layer during AMPA receptor activation. *Biophys. J.* **110**, 896–911 (2016).
26. N. Armstrong, J. Jasti, M. Beich-Frandsen, E. Gouaux, Measurement of conformational changes accompanying desensitization in an ionotropic glutamate receptor. *Cell* **127**, 85–97 (2006).
27. S. Ye *et al*., Tracking G-protein-coupled receptor activation using genetically encoded infrared probes. *Nature* **464**, 1386–1389 (2010).
28. S. Ye, T. Huber, R. Vogel, T. P. Sakmar, FTIR analysis of GPCR activation using azido probes. *Nat. Chem. Biol.* **5**, 397–399 (2009).
29. S. Ye *et al*., Site-specific incorporation of keto amino acids into functional G protein-coupled receptors using unnatural amino acid mutagenesis. *J. Biol. Chem.* **283**, 1525–1533 (2008).
30. S. Naganathan, S. Ye, T. P. Sakmar, T. Huber, Site-specific epitope tagging of G protein-coupled receptors by bioorthogonal modification of a genetically encoded unnatural amino acid. *Biochemistry* **52**, 1028–1036 (2013).
31. G. M. Martin *et al*., Pharmacological correction of trafficking defects in ATP-sensitive potassium channels caused by sulfonylurea receptor 1 mutations. *J. Biol. Chem.* **291**, 21971–21983 (2016).
32. C. I. Murray *et al*., Unnatural amino acid photo-crosslinking of the IKs channel complex demonstrates a KCNE1:KCNQ1 stoichiometry of up to 4:4. *eLife* **5**, e11815 (2016).
33. V. Klippenstein, V. Ghisi, M. Wietstruk, A. J. R. Plested, Photoinactivation of glutamate receptors by genetically encoded unnatural amino acids. *J. Neurosci.* **34**, 980–991 (2014).
34. V. Klippenstein, C. Hoppmann, S. Ye, L. Wang, P. Paoletti, Optocontrol of glutamate receptor activity by single side-chain photoisomerization. *eLife* **6**, e25808 (2017).
35. M. Tian, S. Ye, Allosteric regulation in NMDA receptors revealed by the genetically encoded photo-cross-linkers. *Sci. Rep.* **6**, 34751 (2016).
36. S. Ding, R. Horn, Slow photo-cross-linking kinetics of benzophenone-labeled voltage sensors of ion channels. *Biochemistry* **40**, 10707–10716 (2001).
37. P. J. Weber, A. G. Beck-Sickinger, Comparison of the photochemical behavior of four different photoactivatable probes. *J. Pept. Res.* **49**, 375–383 (1997).
38. A. I. Sobolevsky, M. V. Yelshansky, L. P. Wollmuth, State-dependent changes in the electrostatic potential in the pore of a GluR channel. *Biophys. J.* **88**, 235–242 (2005).
39. A. I. Sobolevsky, M. V. Yelshansky, L. P. Wollmuth, Different gating mechanisms in glutamate receptor and K+ channels. *J. Neurosci.* **23**, 7559–7568 (2003).
40. C. L. Salussolia *et al*., Interaction of the M4 segment with other transmembrane segments is required for surface expression of mammalian α-amino-3-hydroxy-5-methyl-4-isoxazolepropionic acid (AMPA) receptors. *J. Biol. Chem.* **286**, 40205–40218 (2011).
41. Y. Xu, Y. Ramu, H.-G. Shin, J. Yamakaze, Z. Lu, Energetic role of the paddle motif in voltage gating of Shaker K(+) channels. *Nat. Struct. Mol. Biol.* **20**, 574–581 (2013).
42. A. I. Sobolevsky, M. P. Rosconi, E. Gouaux, X-ray structure, symmetry and mechanism of an AMPA-subtype glutamate receptor. *Nature* **462**, 745–756 (2009).
43. A. L. Carbone, A. J. R. Plested, Superactivation of AMPA receptors by auxiliary proteins. *Nat. Commun.* **7**, 10178 (2016).
44. L. Chen, K. L. Dürr, E. Gouaux, X-ray structures of AMPA receptor-cone snail toxin complexes illuminate activation mechanism. *Science* **345**, 1021–1026 (2014).
45. K. L. Dürr *et al*., Structure and dynamics of AMPA receptor GluA2 in resting, pre-open, and desensitized states. *Cell* **158**, 778–792 (2014).
46. T. Kuner, P. H. Seeburg, H. R. Guy, A common architecture for K+ channels and ionotropic glutamate receptors? *Trends Neurosci.* **26**, 27–32 (2003).
47. M. Alsaloum, R. Kazi, Q. Gan, J. Amin, L. P. Wollmuth, A molecular determinant of subtype-specific desensitization in ionotropic glutamate receptors. *J. Neurosci.* **36**, 2617–2622 (2016).
48. T. Kuner, C. Beck, B. Sakmann, P. H. Seeburg, Channel-lining residues of the AMPA receptor M2 segment: Structural environment of the Q/R site and identification of the selectivity filter. *J. Neurosci.* **21**, 4162–4172 (2001).
49. C. L. Salussolia *et al*., A eukaryotic specific transmembrane segment is required for tetramerization in AMPA receptors. *J. Neurosci.* **33**, 9840–9845 (2013).
50. J. B. Amin *et al*., Divergent roles of a peripheral transmembrane segment in AMPA and NMDA receptors. *J. Gen. Physiol.* **149**, 661–680 (2017).
51. K. K. Ogden *et al*., Molecular mechanism of disease-associated mutations in the pre-M1 helix of NMDA receptors and potential rescue pharmacology. *PLoS Genet.* **13**, e1006536 (2017).
52. J. B. Amin, X. Leng, A. Gochman, H.-X. Zhou, L. P. Wollmuth, A conserved glycine harboring disease-associated mutations permits NMDA receptor slow deactivation and high Ca^{2+} permeability. *Nat. Commun.* **9**, 3748 (2018).
53. L. G. Zachariassen *et al*., Structural rearrangement of the intracellular domains during AMPA receptor activation. *Proc. Natl. Acad. Sci. U.S.A.* **113**, E3950–E3959 (2016).
54. I. Riva, C. Eibl, R. Volkmer, A. L. Carbone, A. J. Plested, Control of AMPA receptor activity by the extracellular loops of auxiliary proteins. *eLife* **6**, e28680 (2017).
55. Y. Zhao, S. Chen, C. Yoshioka, I. Baconguis, E. Gouaux, Architecture of fully occupied GluA2 AMPA receptor-TARP complex elucidated by cryo-EM. *Nature* **536**, 108–111 (2016).
56. S. Tomita *et al*., Stargazin modulates AMPA receptor gating and trafficking by distinct domains. *Nature* **435**, 1052–1058 (2005).

Supplementary Information Appendix

Gating modules of the AMPA receptor pore domain revealed by unnatural amino acid mutagenesis
Poulsen *et al.*

Supplementary Movie 1: Gating modules
Residues corresponding to three spatially contiguous gating modules in the GluA2 pore domain are shown. The collar (green), the bundle crossing (magenta) and the selectivity filter (F579AzF, cyan) are flanked by the null mutants (wheat).

www.pnas.org/cgi/doi/10.1073/pnas.1818845116

Supplementary Materials and methods

Molecular Biology

The aminoacyl-tRNA-synthetase and tRNA constructs for Human embryonic kidney (HEK) cell expression (1, 2) were kind gifts from Thomas Sakmar (Rockefeller). For electrophysiological studies we used the pRK5 expression vector encoding the flip splice variant of the rat GluA2 subunit containing a Q at the Q/R-filter, followed by IRES and eGFP. The mutation Y40TAG was introduced into eGFP to act as a reporter of rescue (described in (3)). Amber stop codons were introduced by overlap PCR and confirmed by DNA sequencing. To study the active state of GluA2, a mutation (L483Y) was introduced that blocks receptor desensitization and stabilises an open state (4).

The pRK5 vector was also used for biochemical experiments, but for this purpose the GluA2 subunit carried a C-terminal FLAG-tag epitope (5) for purification and three cysteines deleted (C190A, C436S, C528S) to lower background subunit dimerization (3). The TEV protease recognition site 'ENLYFQGS' was inserted immediately before W572 in the M1-M2 intracellular loop with the native E571 being part of the TEV site (6).

Cell culture and transfection

HEK293T for biochemical experiments and HEK293 cells for electrophysiological experiments were maintained in Miminum Essential Medium (MEM, Sigma-Aldrich) supplemented with 10% serum and 5% penicillin/streptomycin and grown at 37°C with 5% CO_2. HEK293 and HEK293T cells were transiently transfected using polyethylenimine (PEI) in a 1:3 ratio (v/v; DNA/PEI) one day after cells were seeded. To suppress the amber stop codon, GluA2 mutants were co-expressed with vectors encoding mutated tRNA and synthetase for either AzF or BzF in the mass ratio 4:1:1. After six hours of incubation, the transfection medium was replaced by MEM supplemented with AzF (0.5 mM) or BzF (1 mM). We dissolved BzF (Bachem) in 1 M HCl and AzF (Chem-Impex International) in 1 M NaOH, which was immediately added to pre-warmed MEM containing 10% serum. Media supplemented with BzF or AzF were adjusted to pH 7.3 and filter-sterilized (0.22 μm PVDF filter) before use (1, 7). Control experiments on wild-type receptors were done on the background of the AzF or BzF synthetase and the UAA medium.

Electrophysiology

Patch clamp recordings of outside-out patches from HEK cells expressing mutant and wild-type glutamate receptors were performed 2-3 days after transfection. The external solution was composed as follows (mM): 150 NaCl, 0.1 $MgCl_2$, 0.1 $CaCl_2$, 5 HEPES. The pipette solution contained the following (mM): 115 NaCl, 0.5 $CaCl_2$, 1 $MgCl_2$, 10 Na_2ATP, 10 NaF, 5 Na_4BAPTA, 5 HEPES. Both solutions were titrated with NaOH to pH 7.3. Glutamate was diluted in the external solution and was applied to outside-out patches using a custom-made four-barrel glass perfusion tool (Vitrocom). For most experiments we used 10 mM glutamate to activate, but for some experiments, 1 mM glutamate was applied with no detectable differences in UV induced effects. The perfusion tool was mounted on a piezo-electric transducer (Physik Instrument), which was controlled via the digitizer interface (Instrutech ITC-18, HEKA Instrument). Borosilicate glass electrodes had resistance of 3-5 MΩ. Patches were clamped at -40 to -60 mV. Currents were filtered at 10 kHz and recorded at 40 kHz sampling rate using Axograph X (Axograph Scientific, Sydney, Australia). Macroscopic currents were elicited by applying the ligand for 400 ms. We exposed patches to UV light via epi-illumination from a Rapp UVICO source with a shutter under computer control. The UVICO system had a 120 W metal halide bulb with enhanced UV emission, which was passed through a 400 nm short-pass filter. Focussing this light through the Olympus LUCPFL 20x objective (transmission @ 365 nm > 80%) gave a pulse irradiance of ~30 kW/m^2 at the sample (30 mW at 365 nm, for the roughly 1 mm^2 field of view). For state-dependent receptor trapping, patches were exposed to UV light when the receptor was either in the resting (before glutamate application), desensitised

(during glutamate application) or in the active state (during glutamate application on L483Y-mutants) for 50 ms to 200 ms in each episode. It was not possible to record macroscopic currents from F608AzF (M3) harbouring the L483Y mutation, so in this case 100 μM cyclothiazide (Ascent Scientific) was applied to trap the receptor in an active state. All chemicals were purchased from Roth unless otherwise noted.

Kinetic Modelling
Simulated responses to glutamate for a set of kinetic models were generated using the Aligator scripts (https://www.github.com/aplested). The rate constants for the base model (before correction for microscopic reversibility on loops) were the same as those in our previous work, and provide a fair description of GluA2 kinetics (8). The rates constants were (per second): $\beta = 8{,}000$; $\alpha = 3{,}000$; $d_2{*}+ = 120$; $d_2{*}- = 2$; $d_2+ = 120$; $d_2- = 5$; $d_1+ = 300$; $d_1- = 25$; $d_0+ = 1$; $d_0- = 3$; $k+ = 5{,}000{,}000\ M^{-1}$; $k- = 40{,}000$; and $k_d- = 2{,}500$. Families of responses were generated by changing individual rate constants progressively, and correcting for microscopic reversibility (MR). These simulations extended previously used code to allow the conductance of states to change across a set of simulated currents, in order to mimic the desensitised state becoming conductive. We present 6 different simulations, as follows:

- Altering channel shutting rate ("$\Delta\alpha$" in figure 6C, rate d_{1-} was varied to ensure MR on the loop).

- Altering channel opening rate ("$\Delta\beta$", rate d_{1-} was varied to ensure MR on the loop).

- Reducing AD_2 lifetime ("ΔDes", rates d_{2-}, d_{2^*-} altered by a common factor, no MR compensation needed because rate alterations were symmetrical on the cycle).

- AD_2 becomes conducting ("γ Des $\neq 0$", no changes to rate constants)

- Rates d_{1-}, d_{2-}, d_{2^*-} and α all varied by common factor ("ΔDes, $\Delta\alpha$", no MR compensation needed because the rate alterations were symmetrical).

- Rates d_{1-}, d_{2-}, d_{2^*-} and α all varied by common factor and AD_2 becomes conducting ("ΔDes, $\Delta\alpha$, γ Des $\neq 0$", no MR compensation needed because the rate alterations were symmetrical)

Structural Analysis
We aligned the C-alpha atoms of residues 510-620 and 795-810 (membrane segments M1-3 and M4) from chains A & C of GluA2 from six CryoEM and crystal structures: 5VOT, 5WEO (open), 5WEK, 5L1B (resting), 5VHZ, 5V0V (desensitised) (9–12) using the PyMol command "Align". The selection of residues was interactively checked and chosen to give the most reliable alignment across all four subunits. We measured per-subunit distances between residues in different structures, and also took radial displacements by halving distances between diametrically-opposed subunits (e.g. between A and C, and B and D). Distances were taken between C-alpha atoms in the same chains for separate structures (for residue displacements), and between diametrically opposed chains in the same structures (for axial distances). These structures were obtained in both the presence and absence of different auxiliary proteins, which may contribute to variations between them. Scripting was done in the Anaconda distribution of Python supplied with PyMol 2.0 (Schrödinger).

Biochemistry

For biochemical experiments HEK293T cells were plated in dishes of 10 cm diameter and transfected as described above (cell culture and transfection). Three days after transfection the cells were exposed to UV light ($\sim$ 300 W/m^2) on ice in a ventilated chamber (Luzchem, LZC-1) for 2-15 minutes. We avoided longer exposures of, for example, 30 minutes in the UV oven, because these exceed the exposures needed for the relatively rapid changes in the gating properties that we detected in electrophysiological experiments. UV induced crosslinking was performed in the presence of 40 mM N-ethyl-maleimide (NEM, Thermo Fisher Scientific), to reduce spurious dimer formation from exposed free cysteines during solubilization and later denaturation. Cells were harvested immediately after UV exposure, lysed in buffer containing 1% dodecylmaltoside (Glycon Biochemicals) and 40 mM NEM. Lysates were incubated with ANTI-FLAG M2 Affinity Gel (Sigma-Aldrich) and column purified (illustra MicroSpin, GE Healthcare). NEM inhibits TEV protease, therefore it was necessary to wash the samples extensively during purification to remove NEM before adding TEV protease for overnight digestion (TEV Protease, Protean). The second elution round was loaded on 4-12% NuPAGE Novex gels (Invitrogen) and run in reducing conditions in presence of 500 mM 2-Mercaptoethanol (Sigma-Aldrich) at 200 mV for 2 h. Transfer of the proteins to PVDF membranes (Immobilon- FL Millipore) was done using XCell surelock mini-cell and XCell II Blot Module (Invitrogen) as described in the manufacturer's instructions. To enable quantitative detection of N- and C-terminal reactive bands in the same blot, membranes were incubated overnight at 4°C with polyclonal rabbit anti-GluR2/3 antibody (1:1000, Millipore) and monoclonal mouse anti-FLAG M2 antibody (1:1000, Sigma-Aldrich) respectively. The day after, infra-red dyes conjugated to secondary antibodies (IRDye 800CW Goat anti-mouse and IRDye 680RD Goat anti-Rabbit, Li-COR) were applied to the membranes for 1h at room temperature. The signal produced was detected on a LI-COR Odyssey Fc imager and quantified using ImageStudioLite2. Some experiments were done with semi-quantitative chemiluminescent detection, as described (3). As a control of readthrough the constructs containing an amber TAG stop codon at various positions in the GluA2 TMD were co-expressed with the tRNA and tRNA-synthetase in the absence of UAA, whereas WT controls were co-expressed with the tRNA and tRNA-synthetase in presence of UAA, to check for adventitious incorporation of UAA.

Electrophysiology data analysis

Rate constants for deactivation and desensitization were fit with double exponential functions, and from these we calculated a weighted rate constant. To measure recovery from desensitization, two pulses of glutamate were applied in one episode with varying interpulse intervals. Recovery data were fit with a Hodgkin-Huxley type function (13) with a slope of 2, except where noted. Kymograms of peak current reduction were fit with single exponential decay function. Statistical significance was assessed with Student's *t* test, using either pairwise comparisons for different values from a single patch recording or unpaired tests for comparisons between mutants or different conditions. For multiple comparisons of the measurements before, during and after UV exposure of the F579AzF mutant, we performed repeated measures ANOVA.

Supplementary References

1. Ye S, Huber T, Vogel R, Sakmar TP (2009) FTIR analysis of GPCR activation using azido probes. *Nat Chem Biol* 5(6):397–399.
2. Ye S *et al.* (2008) Site-specific incorporation of keto amino acids into functional G protein-coupled receptors using unnatural amino acid mutagenesis. *J Biol Chem* 283(3):1525–1533.
3. Klippenstein V, Ghisi V, Wietstruk M, Plested AJR (2014) Photoinactivation of glutamate receptors by genetically encoded unnatural amino acids. *J Neurosci* 34(3):980–991.
4. Sun Y *et al.* (2002) Mechanism of glutamate receptor desensitization. *Nature* 417(6886):245–253.
5. Lau AY *et al.* (2013) A conformational intermediate in glutamate receptor activation. *Neuron* 79(3):492–503.
6. Xu Y, Ramu Y, Shin H-G, Yamakaze J, Lu Z (2013) Energetic role of the paddle motif in voltage gating of Shaker K(+) channels. *Nat Struct Mol Biol* 20(5):574–581.
7. Hino N, Hayashi A, Sakamoto K, Yokoyama S (2006) Site-specific incorporation of non-natural amino acids into proteins in mammalian cells with an expanded genetic code. *Nat Protoc* 1(6):2957–2962.
8. Carbone AL, Plested AJR (2016) Superactivation of AMPA receptors by auxiliary proteins. *Nat Commun* 7:10178.
9. Yelshanskaya MV *et al.* (2016) Structural Bases of Noncompetitive Inhibition of AMPA-Subtype Ionotropic Glutamate Receptors by Antiepileptic Drugs. *Neuron* 91(6):1305–1315.
10. Twomey EC, Yelshanskaya MV, Grassucci RA, Frank J, Sobolevsky AI (2017) Channel opening and gating mechanism in AMPA-subtype glutamate receptors. *Nature*
11. Twomey EC, Yelshanskaya MV, Grassucci RA, Frank J, Sobolevsky AI (2017) Structural Bases of Desensitization in AMPA Receptor-Auxiliary Subunit Complexes. *Neuron* 94(3):569–580.e5.
12. Chen S *et al.* (2017) Activation and Desensitization Mechanism of AMPA Receptor-TARP Complex by Cryo-EM. *Cell* 170(6):1234–1246.e14.
13. Carbone AL, Plested AJR (2012) Coupled control of desensitization and gating by the ligand binding domain of glutamate receptors. *Neuron* 74(5):845–857.

Supplementary Tables

Table S1. Western blot analysis. Rescue of monomer expression by UAAs for ten TMD sites. Values represent fold increase in band intensity in presence of UAA relative to the absence of UAA (see methods and supplementary figure 1). The minimum and maximum values are the lower (including non-specific bands also seen in non-transfected cells) and upper (omitting non-specific bands) estimates of the increase in monomer band intensity, respectively. Dimer fraction denotes the intensity of the dimer band relative to the total (monomer plus dimer bands) before and after UV exposure. All data is shown as mean ± SEM with number of independent repetitions (blots) in brackets. Five further mutants listed in Figure 1C (V539, F541, L542, L577, W605) were tested in Western blot using chemiluminescent (*i.e.* semi-quantitative) detection, showing 20-300 fold increases in monomer band intensity (1 to 3 blots per mutant).

		Fold increase				Dimer fraction			
		AzF		BzF		AzF		BzF	
Site		Minimum	Maximum	Minimum	Maximum	Before UV	After UV	Before UV	After UV
WT	-	1 ± 0 (5)	1 ± 0 (5)	1 ± 0 (4)	1 ± 0 (4)	9 ± 1% (5)	9 ± 3% (5)	14 ± 5% (4)	15 ± 6% (4)
F515	Pre-M1	-	-	-	2000 ± 1000 (3)	-	-	22 ± 5% (3)	32 ± 10% (3)
F531	M1	15 ± 5 (4)	950 ± 890 (4)	20 ± 10 (3)	300 ± 200 (3)	8 ± 2% (4)	8 ± 2% (4)	5 ± 1% (3)	7 ± 3% (3)
Y533	M3	30 ± 30 (4)	2000 ± 2000 (4)	5 ± 1 (4)	3000 ± 2000 (4)	8 ± 1% (4)	15 ± 5% (4)	6 ± 1% (4)	8 ± 2% (4)
S537	M1	10 ± 5 (3)	80 ± 30 (3)	10 ± 5 (3)	200 ± 100 (3)	8 ± 1% (3)	8 ± 3% (3)	8 ± 1% (3)	9 ± 1% (3)
L540	M1	10 ± 5 (4)	100 ± 50 (4)	20 ± 10 (3)	180 ± 80 (3)	13 ± 1% (3)	16 ± 1% (3)	11 ± 3% (3)	13 ± 5% (3)
F579	M2	15 ± 10 (3)	270 ± 80 (3)	10 ± 5 (3)	40 ± 20 (3)	9 ± 3% (3)	14 ± 1% (3)	9 ± 2% (3)	10 ± 2% (3)
F584	M2	15 ± 5 (4)	45 ± 10 (4)	15 ± 5 (3)	70 ± 30 (3)	8 ± 2% (3)	12 ± 4% (3)	7 ± 4% (3)	12 ± 5% (3)
F608	M3	10 ± 5 (5)	50 ± 40 (5)	10 ± 5 (3)	3000 ± 3000 (3)	7 ± 2% (4)	8 ± 1% (4)	7 ± 2% (3)	7 ± 2% (3)
F796	M4	10 ± 5 (3)	40 ± 10 (3)	15 ± 5 (3)	130 ± 70 (3)	7 ± 1% (3)	15 ± 4% (3)	9 ± 4% (3)	9 ± 4% (3)
Y797	M4	30 ± 10 (4)	340 ± 130 (4)	15 ± 10 (3)	150 ± 20 (3)	8 ± 3% (3)	8 ± 3% (3)	5 ± 3% (3)	4 ± 1% (3)

Table S2. Kinetics of glutamate responses of selected constructs. Kinetic parameters are reported as mean ± SEM, with the number of patches in brackets. Patches with kinetics measured both before and after UV exposure were included in paired t-tests. * denotes $p < 0.05$, ** $p < 0.01$ and *** $p < 0.001$ vs. before UV

		Desensitization (k_{des}, s^{-1})				Deactivation (k_{deact}, s^{-1})				Recovery from desensitization (k_{rec}, s^{-1})			
		AzF		BzF		AzF		BzF		AzF		BzF	
Site		Before UV	After UV	Before UV	After UV	Before UV	After UV	Before UV	After UV	Before UV	After UV	Before UV	After UV
WT	-	120 ± 10 (21)	120 ± 10 (14)	120 ± 10 (15)	110 ± 10 (9)	1800 ± 150 (16)	2000 ± 200 (8)	1300 ± 200 (11)	1700 ± 400 (5)	55 ± 5 (11)	38 ± 2 (9) **	60 ± 5 (8)	50 ± 5 (4)
F515	Pre-M1	110 ± 10 (8)	90 ± 15 (6)	150 ± 10 (31)	90 ± 10 (19) **	1500 ± 400 (7)	-	1900 ± 300 (13)	2200 ± 200 (6) *	55 ± 10 (3)	-	55 ± 10 (4)	35 ± 5 (4) *
L518	Pre-M1	100 ± 20 (4)	100 ± 20 (4)	130 ± 10 (7)	90 ± 10 (7) *	1100 ± 400 (4)	1000 ± 250 (4)	1350 ± 70 (4)	-	35 ± 10 (2)	-	45 ± 15 (3)	-
F531	M1	160 ± 10 (13)	150 ± 10 (12)	160 ± 10 (16)	180 ± 10 (7)	1500 ± 200 (11)	1800 ± 400 (6)	1900 ± 200 (13)	1400 ± 300 (6) *	50 ± 5 (7)	50 ± 5 (4)	60 ± 10 (7)	40 ± 10 (4)
Y533	M1	130 ± 10 (9)	115 ± 10 (9)	-	-	2100 ± 150 (11)	-	-	-	60 ± 10 (8)	-	-	-
L577	M2	160 ± 10 (17)	95 ± 20 (4)	170± 10 (33)	170 ± 10 (8)	1600 ± 200 (14)	1400 ± 200 (3)	2100 ± 300 (16)	960 ± 150 (3)	40 ± 5 (8)	-	60 ± 10 (10)	55 ± 15 (3)
F579	M2	130 ± 10 (31)	80 ± 5 (25) ***	-	-	1300 ± 150 (16)	600 ± 150 (7)	-	-	40 ± 5 (18)	20 ± 5 (9)	-	-
F584	M2	140 ± 10 (25)	120 ± 10 (12) *	135 ± 5 (43)	150 ± 15 (4)	2000 ± 300 (10)	-	1200 ± 150 (14)	1200 ± 500 (3)	45 ± 5 (8)	-	70 ± 5 (5)	-
F608	M3	170 ± 10 (27)	170 ± 10 (18)	-	-	2200 ± 400 (10)	-	-	-	50 ± 10 (6)	-	-	-
F796	M4	110 ± 5 (25)	130 ± 10 (14)	-	-	1400 ± 100 (13)	-	-	-	55 ± 10 (5)	-	-	-
Y797	M4	120 ± 5 (35)	70 ± 5 (24) ***	125 ± 15 (14)	130 ± 10 (11)	1600 ± 150 (31)	1100 ± 100 (12)	1300 ± 200 (13)	1800 ± 400 (7)	50 ± 5 (22)	40 ± 5 (15)	60 ± 10 (15)	40 ± 10 (4)
I798	M4	50 ± 5 (6)	45 ± 10 (6)	-	-	340 ± 50 (2)	180 ± 5 (2)	-	-	20 (1)	20 (1)	-	-

Table S3. Summary of UV-induced changes in glutamate response. Peak current (I_{peak}) and relative steady-state current (I_{SS}) were assessed before (I_0) and after (I_{UV}) UV exposure during resting or desensitized states. UV effects were also tested in the active state ('LY'). The F608AzF-L483Y construct did not express; we used CTZ to block desensitization for this construct. Null hypothesis significance testing was against either WT or WT-LY (both AzF and BzF) patches, respectively. For null-hypothesis significance tests, * denotes $p < 0.05$, ** $p < 0.01$ and *** $p < 0.001$ against control, Student's *t*-test. We obtained time constants of peak current reduction (in number of 200 ms UV exposures, and in seconds of cumulative exposure) from mono-exponential fits to peak current kymograms. All values are mean ± SEM. The number of patches are in brackets.

Condition		I_{peak} (I_{UV}/I_0)	Relative I_{SS} (I_{UV}/I_0)	Tau (exposures)	Time constant (s)
WT + AzF		0.93 ± 0.04 (12)	1.18 ± 0.04 (12)	-	-
WT-LY + AzF		0.87 ± 0.01 (3)	-	-	-
WT + BzF		0.97 ± 0.04 (8)	1.2 ± 0.2 (8)	-	-
WT-LY + BzF		0.79 ± 0.16 (4)	-	-	-
WT + BzF + CTZ		0.11 ± 0.02 (8)***	-	41 ± 6 (8)	8 ± 1 (8)
F515BzF	Pre-M1	1.6 ± 0.1 (18)***	2.5 ± 0.4 (18)**	-	-
F515BzF-LY		1.2 ± 0.1 (6)**	-	-	-
L518BzF	Pre-M1	1.3 ± 0.2 (6)	8 ± 2 (6)*	-	-
Y533AzF	M1	0.07 ± 0.01 (10)***	2.3 ± 0.4 (9)*	20 ± 3 (10)	4 ± 0.6 (10)
Y533AzF-LY		0.07 ± 0.02 (8)***	-	21 ± 2 (7)	4.1 ± 0.4 (7)
F579AzF	M2	0.29 ± 0.04 (23)***	5 ± 0.7 (25)***	11 ± 1 (14)	2.2 ± 0.2 (14)
F579AzF-LY		0.25 ± 0.03 (11)	-	16 ± 2 (11)	3.2 ± 0.3 (11)
F584AzF	M2	0.07 ± 0.01 (12)***	3 ± 0.4 (12)**	12 ± 1 (12)	2.5 ± 0.2 (12)
F584AzF-LY		0.08 ± 0.02 (11)***	-	17 ± 2 (11)	3.4 ± 0.4 (11)
F608AzF	M3	0.04 ± 0.01 (17)***	5.4 ± 1.3 (9)*	7 ± 1 (16)	1.5 ± 0.2 (16)
F608AzF + CTZ		0.09 ± 0.02 (3)***	-	9 ± 2 (3)	1.7 ± 0.4 (3)
F796AzF	M4	0.17 ± 0.01 (13)***	2 ± 0.2 (11)**	15 ± 1 (12)	3 ± 0.3 (12)
F796AzF-LY		0.16 ± 0.06 (4)***	-	20 ± 4 (4)	4 ± 0.8 (4)
Y797AzF	M4	0.95 ± 0.03 (26)	3.7 ± 0.4 (27)***	-	-
Y797AzF-LY		0.91 ± 0.03 (5)	-	-	-
I798AzF	M4	0.9 ± 0.1 (6)	7 ± 3 (6)	-	-

Table S4. Amplitudes of control and "read-through" currents. Average peak amplitudes of glutamate-activated currents from GluA2-TAG constructs expressed in HEK cells and incubated in presence or absence of AzF or BzF. In both conditions, outside-out patches (clamped at –60 mV) were excised from green cells (reported by the co-expressed GFP-TAG, see Methods). Values are mean ± SEM with the number of repetitions in brackets.

		I_{peak} (pA)			I_{peak} (pA)		
Site		+AzF	–AzF	fold-increase (+/–AzF)	+BzF	–BzF	fold-increase (+/–BzF)
F515	Pre-M1	-800 ± 300 (10)	-2 ± 1 (3)	410	-370 ± 60 (33)	-40 ± 30 (3)	10
L518	Pre-M1	-	-		-380 ± 150 (8)	-30 ± 25 (3)	13
F531	M1	-400 ± 100 (13)	-60 ± 40 (5)	6	-270 ± 50 (8)	-4 ± 1 (5)	68
Y533	M1	-600 ± 100 (15)	-40 ± 10 (23)	15	-	-	
F541	M1	-630 ± 160 (8)	-180 ± 50 (9)	4	-	-	
L577	M2	-1410 ± 340 (4)	-370 ± 250 (4)	4	-600 ± 70 (39)	-15 ± 10 (8)	40
F579	M2	-600 ± 100 (22)	-160 ± 50 (13)	4	-	-	
F584	M2	-600 ± 10 (25)	-440 ± 170 (17)	1.3	-430 ± 50 (58)	-18 ± 9 (6)	24
F608	M3	-400 ± 70 (28)	-200 ± 100 (5)	2	-	-	
F796	M4	-560 ± 90 (25)	-100 ± 70 (13)	5	-	-	
Y797	M4	-450 ± 70 (40)	-30 ± 20 (12)	15	-300 ± 70 (14)	-2 ± 0.3 (6)	152
I798	M4	-450 ± 60 (6)	-60 ± 40 (12)	8	-	-	

Table S5. Kinetics of glutamate responses from "read-through" current. Kinetic parameters of glutamate-induced read-through currents from GluA2-TAG constructs expressed in HEK cells in absence of UAA (-AzF). Parameters are reported as mean ± SEM, with the number of patches in brackets. Only patches where kinetics were measured both before and after UV exposure were included in null hypothesis significance testing. For following mutants expressed in the background of the BzF-synthetase only desensitization rates before UV application could be measured due to small currents and unstable patches: k_{des} (L577) = 165 ± 60 (2), k_{des} (F584) = 120 ± 55 (3) and k_{des} (F515) = 125 (1). Null hypothesis significance testing gave no significant changes in the kinetic parameters.

		I_{peak} (I_{UV}/I_0)	Desensitization (k_{des}, s^{-1})		Deactivation (k_{deact}, s^{-1})		Recovery from desensitization (k_{rec}, s^{-1})	
			–AzF		–AzF		–AzF	
Site			Before UV	After UV	Before UV	After UV	Before UV	After UV
F531	M1		165 ± 5 (2)	-	-	-	-	-
Y533	M1	0.59 ± 0.08	130 ± 10 (10)	130 ± 10 (2)	1070 ± 270 (7)	-	-	-
F541	M1	0.90 ± 0.04	160 ± 15 (9)	165 ± 10 (7)	1360 ± 300 (8)	1300 ± 400 (5)	40 ± 5 (6)	30 ± 10 (6)
L577	M2		170 ± 20 (4)	-	1120 ± 400 (3)	-	-	-
F579	M2	0.76 ± 0.12	180 ± 25 (8)	170 ± 50 (5)	750 ± 90 (7)	640 ± 80 (5)	20 ± 10 (3)	10 ± 1 (2)
F584	M2	0.65 ± 0.16	150 ± 10 (13)	160 ± 15 (4)	1860 ± 250 (12)	1700 ± 130 (4)	35 ± 10 (7)	30 ± 20 (3)
F608	M3		130 ± 25 (5)	-	-	-	-	-
F796	M4		215 ± 30 (4)		1370 ± 330 (2)	-	-	-
Y797	M4	0.68	175 ± 20 (4)	170 (1)	1000 ± 270 (2)	-	-	-
I798	M4	0.90	85 ± 35 (5)	60 (1)	425 ± 190 (3)	525 (1)	-	-

Table S6. Amplitudes of additional M4 constructs harboring AzF. Average peak amplitudes of glutamate-activated currents from GluA2-TAG constructs expressed in HEK cells and incubated in presence or absence of AzF. Values are mean ± SEM with the number of repetitions in brackets.

		I_{peak} (pA)		fold-increase
Site		+AzF	–AzF	(+/–AzF)
F803	M4	0	-	-
G804	M4	-260 ± 70 (4)	-125 ± 70 (7)	2
L808	M4	-500 ± 180 (5)	-225 ± 190 (4)	2
V809	M4	-175 ± 25 (4)	-5 ± 5 (3)	35
A810	M4	-260 ± 100 (6)	-25 ± 10 (4)	10
F814	M4	-360 ± 130 (3)	-125 ± 60 (4)	3

Table S7. Kinetic parameters of additional M4 constructs. Kinetic parameters are reported as mean ± SEM, with the number of patches in brackets.

		Desensitization (k_{des}, s^{-1})		Deactivation (k_{deact}, s^{-1})		Recovery (k_{rec}, s^{-1})	
		+AzF		+AzF		+AzF	
Site		Before UV	After UV	Before UV	After UV	Before UV	After UV
F803	M4	-		-		-	
G804	M4	130 ± 10 (4)	120 ± 20 (3)	1295 ± 175 (4)	1090 ± 120 (2)	47 ± 10 (4)	45 ± 15 (2)
L808	M4	135 ± 5 (5)	115 ± 5 (3)	2105 ± 470 (4)	1580 ± 335 (3)	80 ± 5 (4)	60 ± 5 (2)
V809	M4	220 ± 50 (3)	-	1670 ± 145 (3)	-	65 (1)	-
A810	M4	120 ± 40 (5)	90 ± 1 (2)	1400 ± 410 (6)	770 ± 175 (2)	70 ± 10 (5)	50 ± 5 (2)
F814	M4	140 ± 20 (3)	150 ± 10 (2)	1530 ± 320 (3)	1180 ± 440 (2)	50 ± 10 (3)	50 ± 10 (2)

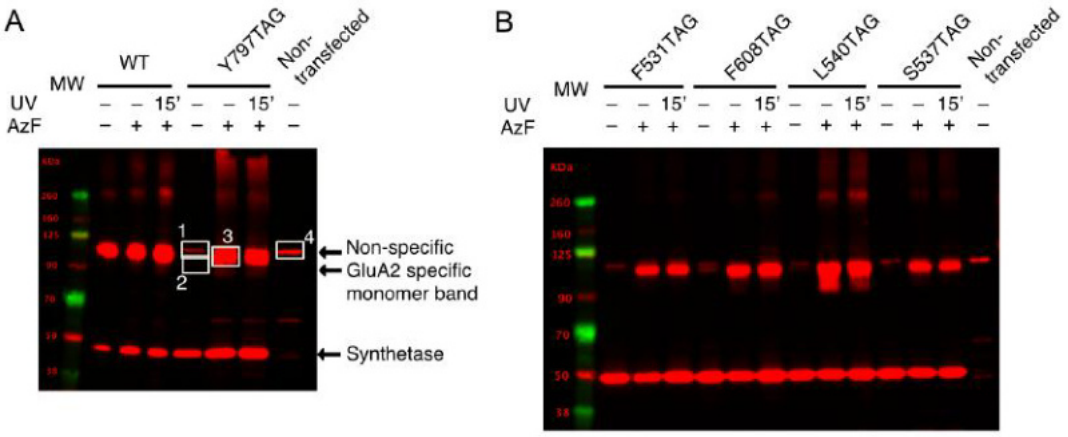

Supplementary Figure 1. Representative Western blots of GluA2 TAG mutants rescued by AzF incorporation.
A Estimation of the enrichment of expression by AzF for the Y797TAG mutant. Western blotting against the FLAG epitopes on GluA2 and the tRNA synthetase also reveals a non-specific band around 100 kDa, similar in size to monomeric GluA2 (indicated for non-transfected HEK 293-T cells with white box #4). Since we could not separate the non-specific band from actual rescue in presence of UAA, we calculated minimum enrichment following inclusion of AzF by taking the ratio of densitometric measurement including the non-specific band (Box #3 / [Box #1 + Box #2]) or the maximum enrichment by excluding the non-specific band (Box #3/ Box #2). **B** Typical Western blot for measurement of enrichment following AzF inclusion in culture media for four TAG mutants of GluA2. Dimeric fractions can be seen around 260 kDa for L540, but these were not enhanced by UV (15' exposure).

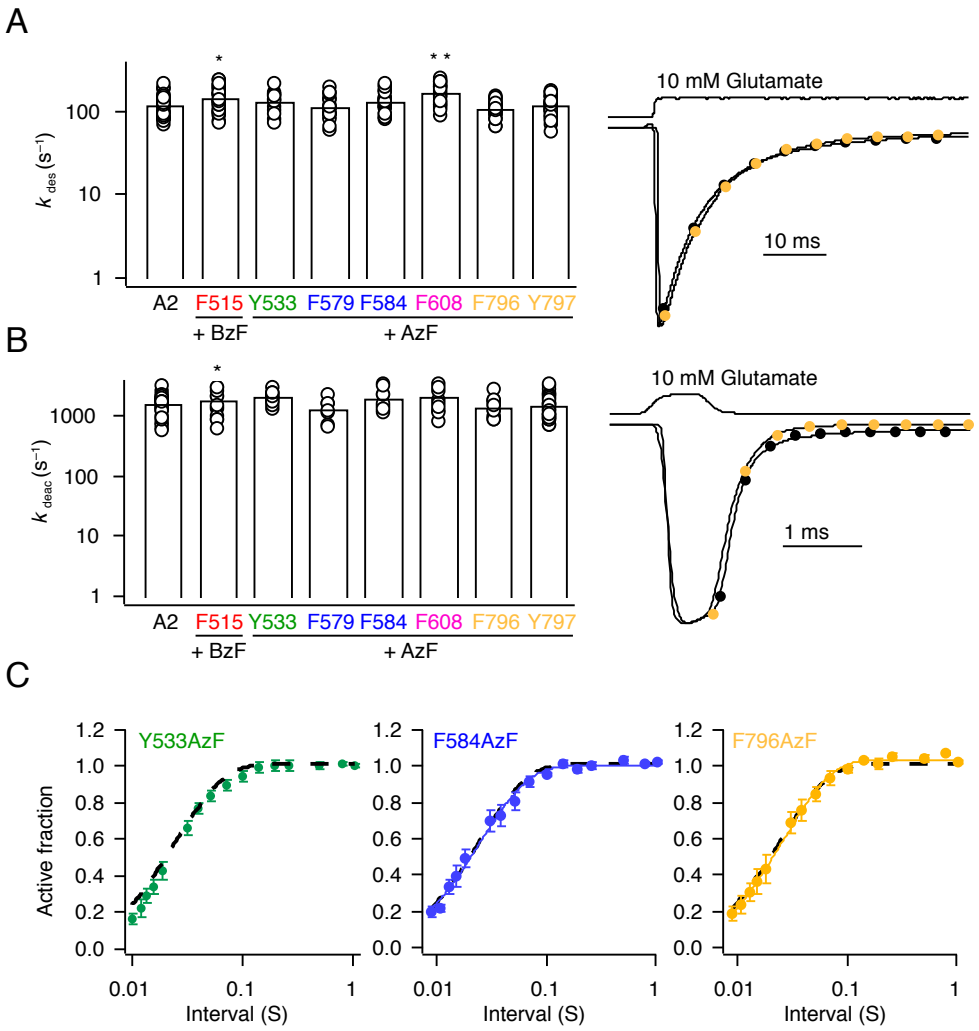

Supplementary Figure 1. Kinetics of GluA2 receptors harboring AzF or BzF in the transmembrane domain.
A Bar graph (*left*) summarizing desensitization rates of selected GluA2 constructs with AzF or BzF. **Significant difference GluA2 WT vs. mutant ($p < 0.001$, t-test), * Significant difference GluA2 WT vs. mutant ($p < 0.05$, t-test). Traces (*right*) illustrating the rate of desensitization of GluA2 WT (*black*) and F796AzF (*yellow*). **B** Bar graph (*left*) summarizing deactivation rates for selected constructs with AzF or BzF after a brief (1 ms) pulse of 10 mM glutamate. Traces (*right*) illustrate the rate of deactivation of GluA2 WT (*black*) and F796AzF (*yellow*). **C** Pooled data for recovery from desensitization of GluA2 WT (black dotted line), GluA2-Y533AzF (green), -F584AzF (blue) and -F796AzF (yellow). See Supplementary Table 2 for a summary of rates.

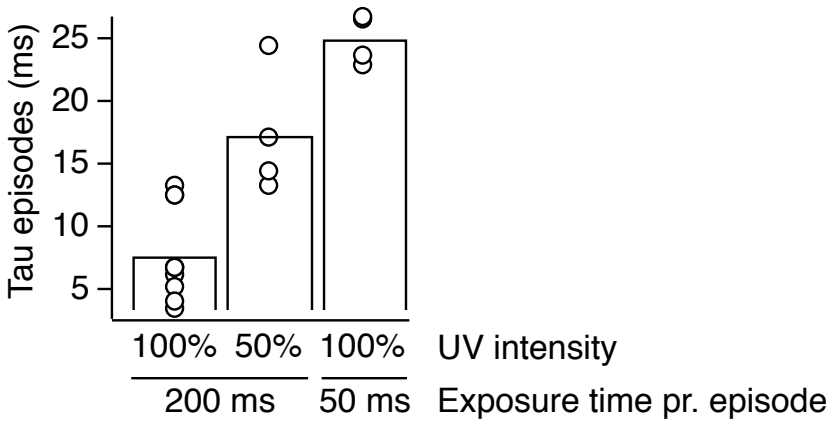

Supplementary Figure 3. Dependency on UV intensity and exposure time.
Summary of the exponential half-times of GluA2-F608AzF inactivation, plotted against the UV exposure periods per episode in milliseconds. The rate of peak current reduction could be manipulated by changing the intensity of the UV light from 100% (τ 200 ms,100% = 7 ms) to 50% (τ 200 ms,50% = 17 ms) or reducing the time interval of UV exposure to 50 ms (τ 50 ms,100% = 25 ms), verifying that the peak-current reduction is controlled by UV light.

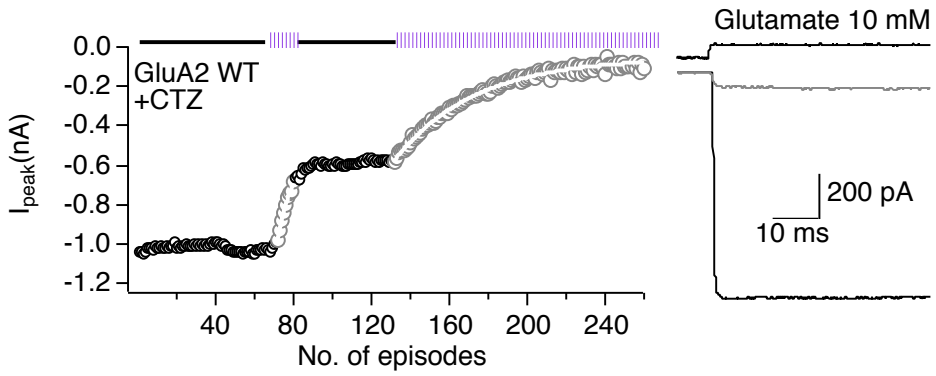

Supplementary Figure 4. UV-induced inhibition of GluA2 wild-type in the presence of CTZ.
UV exposures resulted in a decrease in the peak current after the application of glutamate and 100 μM CTZ. This effect was irregular and showed batch to batch variation (compare with Klippenstein et al. 2014). *Left*; Example kymogram illustrates the UV inactivation of GluA2 WT due to the presence of CTZ, plotted as described in the legend to Figure 2. *Right*; Example responses from the beginning (black) and end of the kymogram (grey).

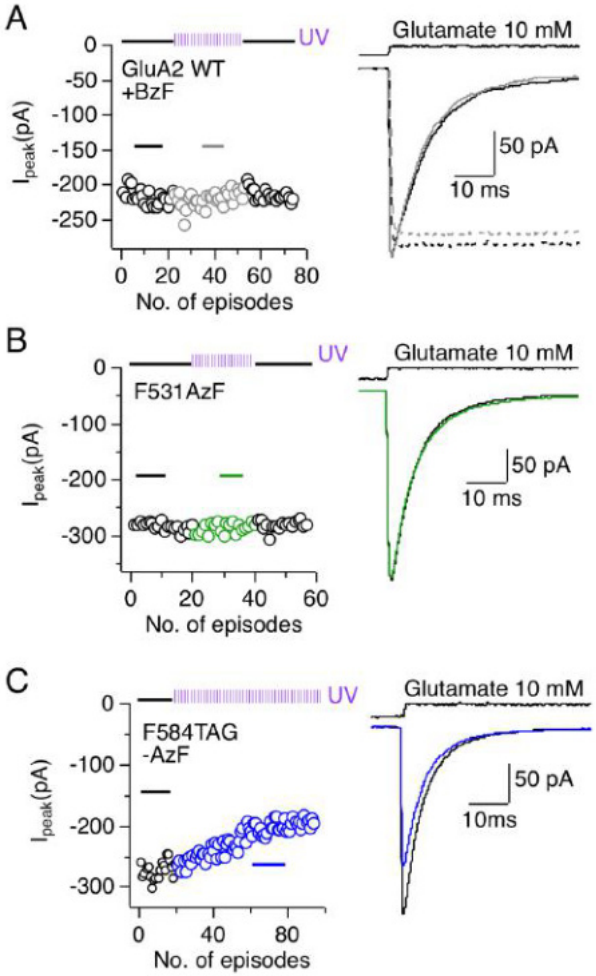

Supplementary Figure 5. Three null results of UV exposure.
A UV exposure did not change the glutamate response for the GluA2 WT cultured in the presence of BzF and the appropriate tRNA-synthetase pair. Kymogram (*left*) as described in Figure 2 illustrates the time course of UV exposure, and example currents (*right*) from sections of the histogram labeled with a solid line. The effect of UV exposure in the active state of the GluA2 WT was also tested by introducing the L483Y mutation to block desensitization (dotted lines). **B** GluA2-F531AzF was insensitive to UV. **C** All tested TAG mutants that were not rescued with an UAA, but that gave a current due to read through, were also insensitive to UV, as exemplified by F584TAG. This patch exhibited a constant mild rundown, independent of the UV exposure.

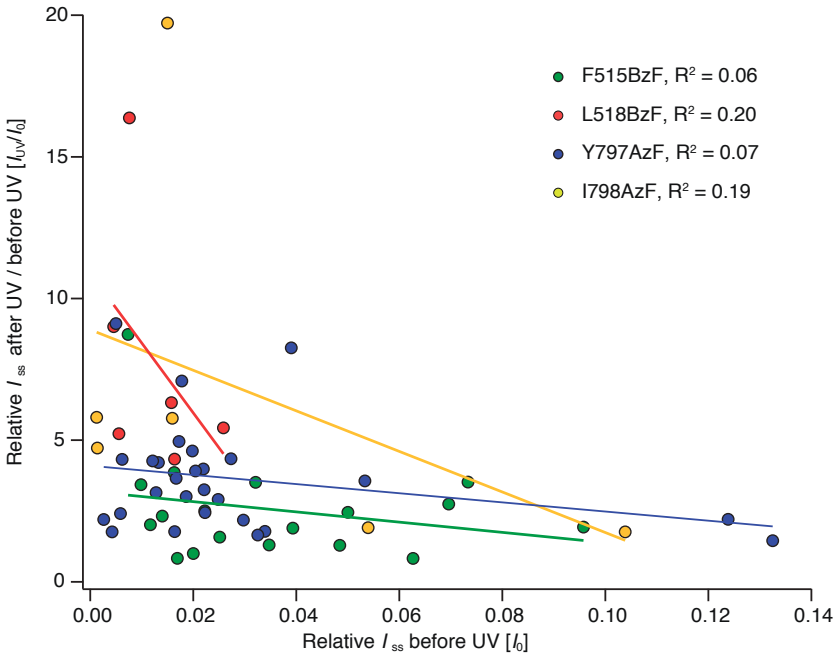

Supplementary Figure 6. Relation between the initial steady-state current and photopotentiation.
Graph showing the absence of correlation between relative steady-state currents (I_{ss}/I_{peak}) before UV application (I_0) and the fold change in relative steady-state current (I_{ss}/I_{peak}) before and after UV application (I_{UV}/I_0) for the GluA2-F515BzF, -L518BzF, -Y797AzF and -I798AzF mutants. Thus, UV induced photopotentiation of the relative steady-state current was independent of the amplitude of the initial relative steady-state current.

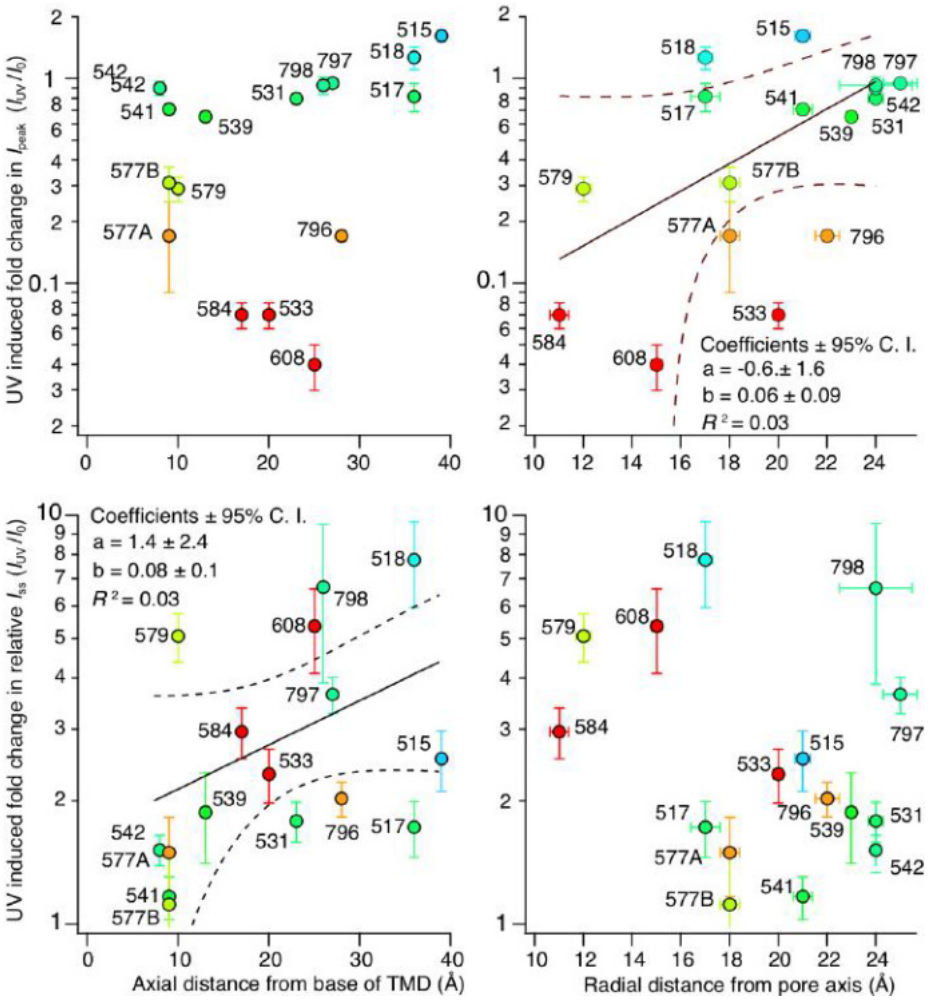

Supplementary Figure 7. Comparing distances at photoactive sites and UV induced effects.
The UV-induced fold changes of peak currents (*upper panels*) and relative steady-state currents (I_{ss}/I_{peak}) (*lower panels)*, of each mutant were plotted against the axial distance of UAA insertion site from the base of the TMD (*left panels*) or the radial distance from the pore axis (*right panels*) in Ångström. Distances were taken between the C_α atoms of the UAA insertion site and the base of the TMD (L817) or between C_α atoms of the UAA insertion site in diametrically opposed chains. The sites are color-coded according to their UV-induced fold change in peak current (as in Figure 5B). 577A and 577B denotes the insertion of AzF and BzF, respectively, at this particular site.

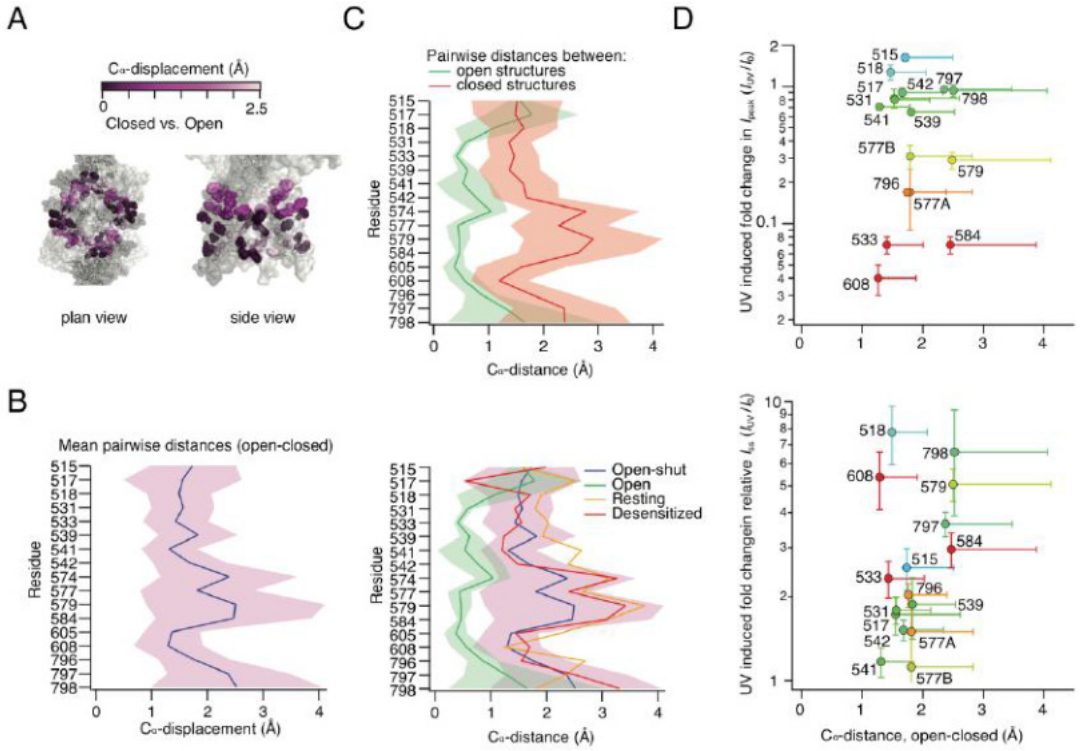

Supplementary Figure 8. Amino acid displacements in published structures.
A Colored bar (*upper*) shows the used color code for C_α-displacement in Ångström of the AzF/BzF insertion sites between resting (PDB ID: 3kg2) and active (PDB ID: 5weo) state. Dark magenta indicates no to very small movements, whereas light magenta indicates bigger movements. PYMOL figures (*bottom*) show selected insertion sites as spheres colored according to its UV C_α-displacement effect. **B** Relation between the C_α-distances at the UAA insertion sites in the open to closed state structures. **C** Structures were further divided into closed and open (*upper panel*) and open-shut, open, resting and desensitized state (*lower panel*). **D** Graph showing the C_α-distance between open and closed structures and the site-specific UV-induced effect on receptor peak current amplitude (*upper*) and relative steady-state current (*bottom*) for each site of the TMD, respectively. The individual sites are color-coded according to the specific UV-induced effects on peak current as in Supplementary Figure 7. Distances between C_α atoms in the same chains were measured between open and closed channel structures. Errors derive from variability in distances between different subunits and between different structures.

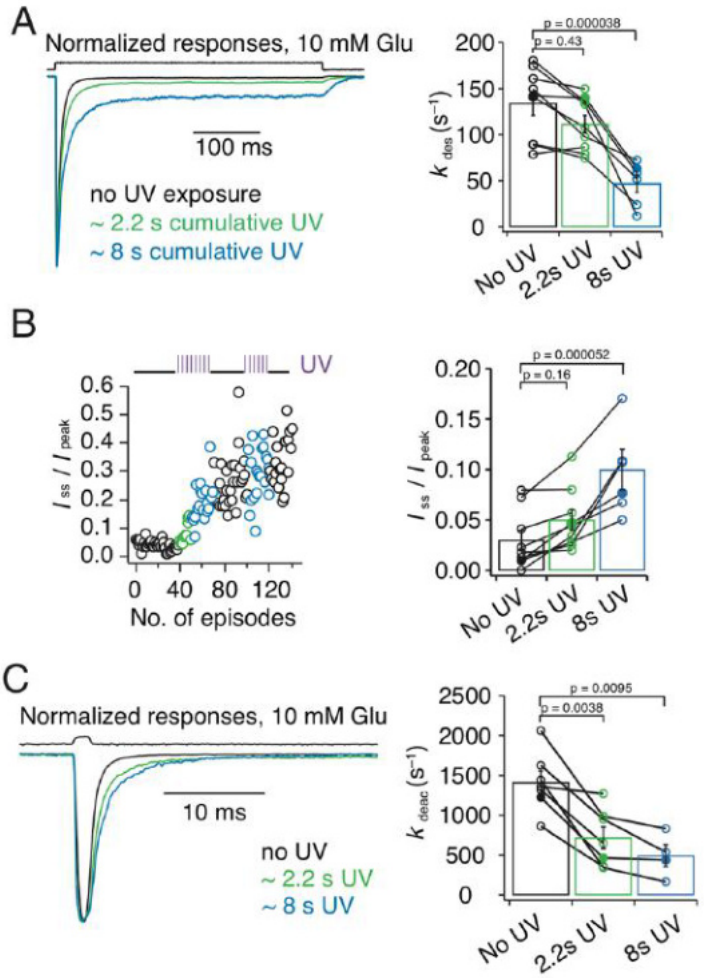

Supplementary Figure 9. Activation of F579AzF (M2) mutant with long and short pulses of glutamate.

A Exemplary normalized traces for desensitizing responses to a 400 ms glutamate pulse, before (black), during (2.2 s, green) and after (8 s, blue) UV exposure. Bar graph shows rates of desensitization ± SEM before, after 2.2 s and after 8 s of UV exposure from paired recordings: k_{des} = 130 ± 15 s^{-1} (n = 9), k_{des} = 110 ± 10 s^{-1} (n = 9) and k_{des} = 50 ± 10 s^{-1} (n = 6). **B** Increase in the relative steady-state current, relative to the peak. I_{ss}/I_{peak} = 0.03 ± 0.01 (n = 9), I_{ss}/I_{peak} = 0.05 ± 0.01 (n = 9) and I_{ss}/I_{peak} = 0.1 ± 0.02 (n = 6). **C** Exemplary normalized traces for responses to a 1 ms application of 10 mM glutamate, with the same color code as panel B. Bar graph shows rates of deactivation before, during and after UV, respectively: k_{deac} = 1400 ± 140 s^{-1} (n = 7), k_{deac} = 700 ± 140 s^{-1} (n = 7) and k_{deac} = 500 ± 140 s^{-1} (n = 4). Solid symbols indicate the rates for the responses shown in the left panels. Error bars represent SEM.

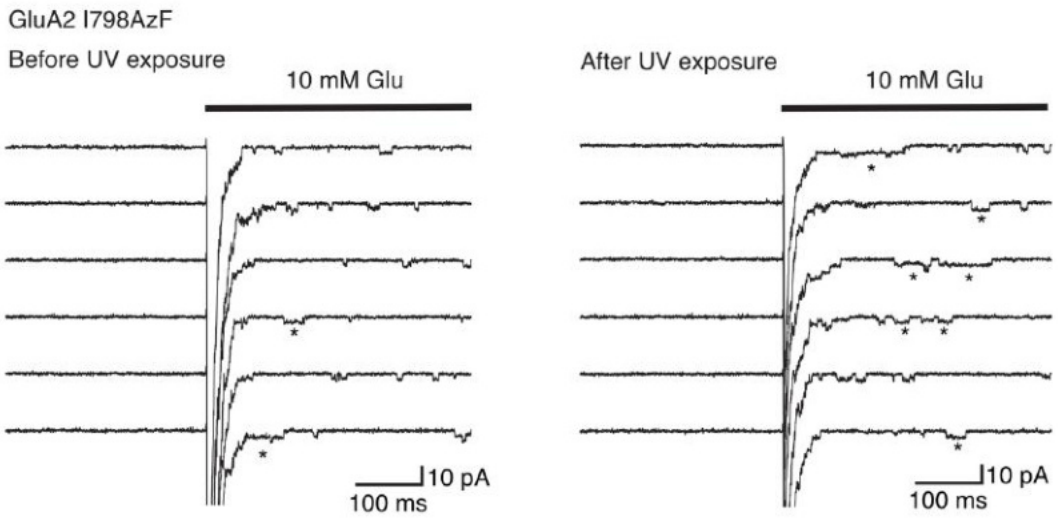

Supplementary Figure 10. Photoactivation at I798AzF lengthens the activations of individual receptors.
Representative desensitized traces from GluA2-I798AzF outside-out patches before (*left*) and after (*right*) UV exposure. After UV exposure, long bursts (>25 ms) with high open probability (*) became much more prevalent. The traces were filtered at 1 kHz. The holding voltage was –60 mV.

VII Curriculum Vitae

Mein Lebenslauf wird aus datenschutzrechtlichen Gründen in der elektronischen Version meiner Arbeit nicht veröffentlicht.

VIII Publication list

Poulsen M.*, **Poshtiban A.***, Klippenstein V., Ghisi V. and A.J.R. Plested (2019). "Gating modules of the AMPA receptor pore domain revealed by unnatural amino acid mutagenesis. *Proceedings of the National Academy of Sciences of the United States of America*. DOI: 10.1073/pnas.1818845116 (Shared first-authorship; Journal impact factor 2017: 9.504)

Huebl J., **Poshtiban A.**, Brücke C., Siegert S., Bock A., Koziara H., Kmiec T., Rola R., Mandat T. and A. Kühn (2019). "Subthalamic and pallidal oscillatory activity in patients with Neurodegeneration with Brain Iron Accumulation type I (NBIA-I). *Clinical Neurophysiology* 130.4:469-473. DOI: 10.1016/j.clinph.2018.12.012 (Co-authorship; Journal impact factor 2017: 3.614)

Klein C., Rasińska J., Empl L., Sparenberg M., **Poshtiban A**, Hain E.G., Iggena D., Rivalan M., Winter Y. and B. Steiner (2016). "Physical exercise counteracts MPTP-induced changes in neural precursor cell proliferation in the hippocampus and restores spatial learning but not memory performance in the water maze. *Behavioural Brain Research* 307: 227-38. DOI: 10.1016/j.bbr.2016.02.040 (Co-authorship; Journal impact factor 2016: 3.002)

IX Acknowledgements

Firstly, I would like to thank Andrew for giving me the great opportunity to pursue my PhD in the field of biophysics and molecular neurosciences. Your patient, encouraging and also challenging attitude helped me surpass myself professionally as well as personally. Big thanks to all my clever and supportive past and present fellow lab colleagues. I consider myself lucky to be part of the "Happy Plesteds". Your cheerful mood always created a desirable atmosphere in and outside the lab that I wish for my future working life. Special thanks to Mette, who supervised me with great scientific advices in my first PhD year. You were the best companion during our long-lived publication process. Thanks to the team of the NeuroCure PhD stipend funding body that supported my studies.

To life-long friendships with Vicky, Romina, Antonia, Alex and Toni with whom life is so much more beautiful. You supported, and above all inspired me, each in your own special way. To Victor, whose love and support is a strong pillar of my present and future life ahead. Your positive and active spirit always manages to free my mind. Thanks to all not specifically mentioned individuals that crossed my way at some point in my life and shaped my educational and personal path contributing to where I stand today. Last, but not least, I would like to express my warmest thanks to my family. To my brother Kian, who, with his coolness and laid-back way of looking at life, was the idol of my childhood. To my parents, who always faced me with unconditional love, support and belief in me and my path ahead. All the important things in life, I learned from you, which enabled me to overcome any challenges in life and reach the educational level that I was fortunate enough to obtain.